ICRP ref: 4834-8186-0460
5 July 2018

Annals of the ICRP

ICRP PUBLICATION 1XX

Dose Coefficients for External Exposures to Environmental Sources

Authors on behalf of ICRP
N. Petoussi-Henss, D. Satoh, A. Endo, K.F. Eckerman,
W.E. Bolch, J. Hunt, J.T.M. Jansen, C.H. Kim, C. Lee, K. Saito,
H. Schlattl, Y.S. Yeom, S.J. Yoo

PUBLISHED FOR
The International Commission on Radiological Protection
by

[SAGE logo]

Please cite this issue as 'ICRP, 20YY. Title of the annals. ICRP Publication XXX, Ann. ICRP 00 (0).'

CONTENTS

[GUEST] EDITORIAL

To be drafted

Dose Coefficients for External Exposures to Environmental Sources

ICRP Publication XXX

Approved by the Commission in xxx

Abstract- This publication presents radionuclide-specific organ and effective dose rate coefficients for members of the public resulting from environmental external exposures to radionuclide emissions of both photons and electrons, calculated using computational phantoms representing the ICRP reference newborn, 1-year-old, 5-year-old, 10-year-old, 15-year-old, and adult males and females. Environmental radiation fields of monoenergetic photon and electron sources were firstly computed using the Monte Carlo radiation transport code PHITS (Particle and Heavy Ion Transport code System) for source geometries representing environmental radionuclide exposures including planar sources on and within the ground at different depths (representing radionuclide ground contamination from fall-out or naturally occurring terrestrial sources), volumetric sources in air (representing a radioactive cloud), and uniformly distributed sources in simulated contaminated water. For the above geometries, the exposed reference individual is considered to be completely within the radiation field. Organ equivalent dose rate coefficients for monoenergetic photons and electrons were next computed employing the PHITS code thus simulating photon and electron interactions within the tissues and organs of the exposed reference individual. For quality assurance purposes, further cross-check calculations were performed using GEANT4, EGSnrc, MCNPX, MCNP6, and the Visible Monte Carlo radiation transport codes. From the monoenergetic values, nuclide-specific effective and organ equivalent dose rate coefficients for several radionuclides for the above environmental exposures were computed using the nuclear decay data from *Publication 107*. The coefficients are given as dose rates normalised to radionuclide concentrations in environmental media, such as radioactivity concentration, in units of nSv h^{-1} Bq^{-1} m^{-2} or nSv h^{-1} Bq^{-1} m^{-3} and can be re-normalised to ambient dose equivalent (Sv Sv^{-1}) or air kerma (Sv Gy^{-1}). The findings showed that, in general, the smaller the body mass of the phantom, the higher the organ and effective dose due to (1) closer proximity to the source (in the case of ground contamination) and (2) the smaller amount of body shielding of internal organs in the younger and smaller reference phantoms. The difference in effective dose between an adult and an infant is 60-140% at a photon energy of 50 keV, while it is less than 70% above a photon energy of 100 keV, where the smaller differences are observed for air submersion and the largest differences are observed for soil contamination on the surface of the ground. For realistic exposure situations of radionuclide environmental contamination, the difference was found to be more moderate. For example, for radioactive caesium (^{134}Cs, ^{136}Cs, ^{137}Cs/^{137m}Ba) deposited on and in the ground, the difference in effective dose between an adult and an infant was in the range of 20-60%, depending on the radioactivity deposition depth within the soil.

Keywords: External radiation; Environmental; Effective Dose; Organ equivalent dose; Dose coefficients; Ambient dose equivalent; Soil contamination; Air submersion; Water immersion.

AUTHORS ON BEHALF OF ICRP
N. Petoussi-Henss, D. Satoh, A. Endo, K.F. Eckerman,
W.E. Bolch, J. Hunt, J.T.M. Jansen, C.H. Kim, C. Lee,
K. Saito, H. Schlattl, Y.S. Yeom, S.J. Yoo

PREFACE

The membership of the Task Group 90 “Age Dependent Dose Coefficients for External Environmental Exposures” was as follows:

N. Petoussi-Henss (Chair)	K. Eckerman	H. Schlattl
W. Bolch	A. Endo	

Corresponding members were:

M. Bellamy	J.T.M. Jansen	D. Satoh
N. Hertel	C. Lee	Y. S. Yeom
J. Hunt	K. Saito	S. J. Yoo

Additional contributor to this publication was:

D. Santos

The membership of Committee 2 during the period of preparation of this report was:

(2009-2013)

H-G. Menzel (Chair)	R. Cox	R. Leggett
M.R. Bailey	G. Dietze	J.L. Lipsztein
M. Balonov	K.F. Eckerman	J. Ma
D. Bartlett	A. Endo	F. Paquet
V. Berkovski	J.D. Harrison	N. Petoussi-Henss
W.E. Bolch	N. Ishigure	A.S. Pradhan

(2013-2017)

J.D. Harrison (Chair)	M. Degteva	D. Noβke
M.R. Bailey	A. Endo	F. Paquet
V. Berkovski	J.G. Hunt	N. Petoussi-Henss
L. Bertelli	C. Hyeong Kim	F. Wissmann
W.E. Bolch	R. Leggett	
D. Chambers	J. Ma	

(2017-2020)

J.D. Harrison (Chair)	C. Hyeong Kim	T. Sato
V. Berkovski	R. Leggett	T. Smith
E. Blanchardon	J. Li	A. Ulanowski
W.E. Bolch	M.A. Lopez	F. Wissmann
A. Giussani	F. Paquet	
D. Jokisch	N. Petoussi-Henss	

MAIN POINTS

- **This publication presents radionuclide-specific reference organ and effective dose rate coefficients for the following types of environmental external exposures: soil contamination, air submersion, and water immersion.**
- **These coefficients are needed to evaluate effective dose and/or organ equivalent doses from activity concentrations in the environment, air kerma free in air, absorbed dose in air, or ambient dose equivalent.**
- **Calculation of the coefficients requires modelling of the environmental field including the exposure geometry, density and composition of both soil and air, and spatial distribution of the radionuclide contamination. The most probable exposure scenarios for both chronic/routine and accidental releases were identified and these respective environmental radiation fields were simulated with the Monte Carlo radiation transport code PHITS.**
- **The magnitude of organ equivalent doses from environmental radionuclide exposures depend on body size since, in external exposures, increasing amounts of overlying tissue enhance body shielding of internal organs. Accordingly, the full series of ICRP reference individuals – both male and female – were considered in this report, including computational phantoms of the newborn, 1-year-old, 5-year-old, 10-year-old, 15-year-old, and adult.**
- **The types of radiation considered were monoenergetic photons (initial energies between 0.01 and 8 MeV) and monoenergetic electrons (same energy range). These simulation results were later used to model organ dosimetry for environmental emissions of gamma-rays, conversion electrons, characteristic x-rays, Auger electrons, and bremsstrahlung x-rays.**
- **The organ and effective dose rate coefficients tabulated in this report are given normalised to environmental radioactivity concentrations for 1252 radionuclides whose nuclear decay data (energies, yields, and branching ratios) are provided in *Publication 107.***
- **The main text of the report provides effective dose rate coefficients for the reference person at each reference age, with additional information on organ equivalent dose rate coefficients provided in an electronic supplement to this report.**
- **The ambient dose equivalent and air kerma rates were obtained for both soil contamination and air submersion using Monte Carlo simulations for the environmental geometries considered. These data enable interpretation of monitoring data relating effective doses to measured values of ambient dose equivalent or air kerma.**

EXECUTIVE SUMMARY

(a) External irradiation from environmental sources of radionuclides is an important pathway of exposure to members of the public which may result from both routine discharges and major accidental releases from nuclear facilities, regions of high naturally occurring radionuclide soil concentrations, or environmental contamination following radiological terrorist events. In the early stages following a nuclear accident, internal exposures due to both inhalation and ingestion of radionuclides are likely to contribute significantly to organ and effective doses, within additional exposure from radionuclide decays in contaminated air plumes, all of which depend upon a variety of factors based upon regional weather conditions. Both external and internal exposures to the public are important after a nuclear accident, whereas external exposures are the more significant exposure pathway over longer timeframes. This was particularly the case following the nuclear power plant (NPP) accident in Fukushima Prefecture, Japan in March of 2011 (UNSCEAR, 2013). Radionuclide ingestion can also play an important role after a certain time following nuclear facility accidents, if appropriate restrictions are not performed promptly regarding the distribution and consumption of potentially contaminated foodstuffs.

(b) Age-dependent dose coefficients for the internal exposures have been evaluated comprehensively by ICRP in *Publications 56, 67, 69, 71*, and *72* (ICRP, 1990, 1993, 1995a,c, 1996a), with current updates published for the reference adults under the Occupational Intakes of Radionuclide (OIR) series (ICRP, 2015, 2016b, 2017). However, age-dependent dose coefficients for external environmental exposures have not been previously evaluated by ICRP. These data are especially important for dose evaluation in the environment where individuals across a wide range of age groups can be potentially exposed. The purpose of this report is, therefore, to provide reference age-dependent dose rate coefficients for external environmental exposures for members of the general public.

(c) Dose rate coefficients are needed to evaluate effective dose from measured or evaluated data on environmental radioactivity concentrations, air kerma rates, absorbed dose rates in air, or ambient dose equivalent rates. Calculation of dose rate coefficients requires evaluation of the environmental field (such as the exposure geometry, the density and composition of soil, and the radionuclide concentration distribution in the environmental media), anatomic computational models of the human body (such as reference voxel phantoms representing exposed members of the general public), and transport simulations of emitted radiations within both the environmental media and anatomy of the exposed individuals. Organ equivalent doses depend on body size since, in external photon exposures, increasing amounts of overlying tissue (skeletal muscle and subcutaneous fats in particular) enhance the shielding of deeper radiosensitive organs (ICRP, 2010). Resultantly, this publication considers the full range of ICRP reference individuals (newborn to adults) in these calculations.

(d) The Task Group has identified the most probable exposure scenarios for this publication. These scenarios are exposure to contamination on or below the ground surface and at different depths (ground exposure); submersion in a contaminated atmospheric cloud (air submersion); and immersion in contaminated water (water immersion). In the first two scenarios, air-over-ground geometry and a human body standing up-right above the ground were assumed.

(e) Organ and effective dose rate coefficients for environmental exposures were computed for the ICRP voxel-based adult male and female reference computational phantoms in *Publication 110* (ICRP, 2009a) as well as for the 10 ICRP reference paediatric phantoms which are a voxel format of the polygon mesh/NURBS (non-rational B-spline) surface phantoms of the University of Florida and National Cancer Institute (Lee et al., 2010). The latter, following some modifications, have been selected in 2013 to become the reference ICRP paediatric phantoms.

(f) ICRP establishes for the first time reference dose rate coefficients for exposure to environmental radionuclides in air, soil and water. Radiations considered include direct photons from radionuclide decays, scattered photons in the environment, beta particles and electrons and bremsstrahlung x-rays from beta particles and from conversion and Auger electrons. For contaminated soil and air, computations were performed in three steps. In Step 1, radiation transport of monoenergetic particles (photons and electrons) from the contaminated environment was conducted and with the resulting radiation field (particle type, energy, and direction) recorded to the surface of a virtual cylinder surrounding the exposed individual (a so-called coupling cylinder). In Step 2, the recorded particles on the surface of the coupling cylinder were subsequently transported, in turn, within the body of each of the 12 reference phantoms. In Step 3, values of organ equivalent dose rate for monoenergetic particles were spectrum weighted to yield radionuclide-specific dose rate coefficients. Additional simulations under the Step 2 included the placement of an air sphere for tallying ambient dose equivalent rate and air kerma rate at a height of 1 m from the ground surface so as to report organ and effective dose rate coefficients normalised to either the environmental radionuclide concentration, or measured values of ambient dose equivalent rate or air kerma rate, where the latter might be obtained from radiation environmental monitoring data.

(g) A data viewer code is provided which allows comfortable viewing and downloading of the dose rate coefficient data.

GLOSSARY

Absorbed dose, *D*

The absorbed dose is given by

$$D = \frac{\mathrm{d}\bar{\varepsilon}}{\mathrm{d}m}$$

where $\mathrm{d}\bar{\varepsilon}$ is the mean energy imparted by ionising radiation to matter of mass (d*m*). The unit of absorbed dose is joule per kilogramme (J kg^{-1}), and its special name is gray (Gy).

Active (bone) marrow

Active marrow is haematopoietically active and gets its red colour from the large numbers of erythrocytes (red blood cells) being produced. Active bone marrow serves as a target tissue for radiogenic risk of leukaemia.

Activity

The number of nuclear transformations of a radioactive material during an infinitesimal time interval, divided by its duration (s). The SI unit of activity is the becquerel (Bq; 1 Bq = 1 s^{-1}).

Activity concentration

Concentration of radioactivity per unit volume per of air or water. The SI unit of activity concentration is Bq m^{-3}.

Activity areal concentration

Concentration of radioactivity per unit area of soil. The SI unit of activity areal concentration is Bq m^{-2}.

Activity density

The activity of a specified radionuclide per unit mass, volume or area of a specified substance.

Air submersion or submersion to contaminated air

External exposure from radionuclides in the radioactive cloud or plume.

Ambient dose equivalent, $H^*(10)$

The dose equivalent at a point in a radiation field that would be produced by the corresponding expanded and aligned field in the ICRU sphere at depth of 10 mm on the radius opposing the direction of the aligned field. The unit of ambient dose equivalent is joule per kilogramme (J kg^{-1}) and its special name is sievert (Sv).

Ambient dose equivalent rate coefficient, $\dot{h}(10)$

The coefficient to convert the activity concentration to the ambient dose equivalent rate. The unit of the ambient dose equivalent rate coefficient for the environmental exposures as referred in this report is nSv h^{-1} Bq^{-1} m^3 or nSv h^{-1} Bq^{-1} m^2.

Becquerel

The special name for the SI unit of activity. 1 Bq = 1 s^{-1}, 1 MBq =10^6 Bq.

Bone marrow

Bone marrow is a soft, highly cellular tissue that occupies the cylindrical cavities of long bones and the cavities defined by the bone trabeculae of the axial and appendicular skeleton. Total bone marrow consists of a sponge-like, reticular, connective tissue framework called stroma, myeloid (blood-cell-forming) tissue, fat cells (adipocytes), small accumulations of lymphatic tissue, and numerous blood vessels and sinusoids. There are two types of bone marrow, red (or active) and yellow (inactive). See ‘Active (bone) marrow’; ‘Inactive (bone) marrow’.

Bone Surfaces

See ‘Endosteum’.

Charged-Particle Equilibrium

Charged-particle equilibrium in a volume of interest means that the energies, numbers, and directions of the charged particles are constant throughout this volume. This is equivalent to saying that the distribution of charged-particle energy radiance does not vary within the volume. In particular, it follows that the sums of the energies (excluding rest energies) of the charged particles entering and leaving the volume are equal.

Cross section,σ

The cross section of a target entity, for a particular interaction produced by incident charged or uncharged particles of a given type and energy, is given by

$$\sigma = \frac{N}{\Phi}$$

where N is the mean number of such interactions per target entity subjected to the particle fluence (Φ). The unit of cross section is m^2. A special unit often used for the cross section is the barn where 1 barn (b) = 10^{-28} m^2. A full description of an interaction process requires, ‘inter alia’, the knowledge of the distributions of cross sections in terms of energy and direction of all emergent particles from the interaction. Such distributions, sometimes called ‘differential cross sections’, are obtained by differentiations of σ with respect to energy and solid angle.

Deposition density

Activity of a specified radionuclide per unit ground area integrated into depth direction, resulted from fallout. The unit is Bq m^{-2}.

Deterministic effect

See ‘Tissue reaction’.

Dose coefficient

A coefficient relating a dose quantity to a physical quantity, both for internal and external radiation exposure. For external environmental exposures, the quantities activity concentration, ambient dose equivalent or air kerma are chosen.

Dose rate coefficient

A coefficient relating a dose quantity to a physical quantity, both for internal and external radiation exposure per unit time.

Dose equivalent, *H*

The dose equivalent at a point is given by

$$H = QD$$

where D is the absorbed dose and Q is the quality factor at that point. The unit of dose equivalent is joule per kilogramme (J kg^{-1}), and its special name is sievert (Sv).

Dose equivalent rate, $\dot{h}$

Dose equivalent per unit time.

Dose response function, *DRF*

A particular function used in this *publication* to represent the absorbed dose in a target region per particle fluence in that region, derived using models of the microscopic structure of the target region geometry, and the transport of the secondary ionising radiations in those regions.

Effective dose, *E*

The tissue-weighted sum of equivalent doses in all specified organs and tissues of the body, given by the expression

$$E = \sum_{T} w_T \sum_{R} w_R D_{T,R} = \sum_{T} w_T H_T$$

where H_T is the equivalent dose in an organ or tissue T, $D_{T,R}$ the mean absorbed dose in an organ or tissue T from radiation of type R, and w_T is the tissue weighting factor. The sum is performed over all organs and tissues of the human body considered to be sensitive to the induction of stochastic effects. The SI unit for effective dose is joule per kilogramme (J kg^{-1}), and its special name is sievert (Sv).

Effective dose rate coefficient, $\dot{e}$

Effective dose per unit time.

Endosteum (or endosteal layer)

A 50-µm-thick layer covering the surfaces of the bone trabeculae in regions of trabecular spongiosa and those of the cortical surfaces of the medullary cavities within the shafts of all long bones. It is assumed to be the target region for radiogenic bone cancer. This target region replaces that previously introduced in *Publications 26* and *30* – the bone surfaces – which had been defined as a single-cell layer, 10 µm in thickness, covering the surfaces of both the bone trabeculae and the Haversian canals of cortical bone.

Equivalent dose, H_T

The equivalent dose in an organ or tissue T is given by:

$$H_T = \sum_R w_R D_{T,R}$$

where $D_{T,R}$ is the mean absorbed dose from radiation R in an organ or tissue T, and w_R is the radiation weighting factor. The unit for equivalent dose is joule per kilogramme (J kg^{-1}) and its special name is sievert (Sv).

Equivalent dose rate coefficient, $\dot{h}_T$

Equivalent dose per unit time.

Fluence, Φ

The quotient of dN by da, where dN is the number of particles incident on a sphere of cross-sectional area da, thus:

$$\Phi = \frac{dN}{da}$$

The unit of fluence is m^{-2}.

ICRU 4-element tissue

ICRU 4-element tissue like material with density of 1 g cm^{-3}, and a mass composition: 76.2 % oxygen, 11.1 % carbon, 10.1 % hydrogen and 2.6 % nitrogen. The ICRU sphere has this assumed composition.

Inactive (bone) marrow

In contrast to the active marrow, inactive marrow is haematopoietically inactive (i.e., does not support haematopoiesis directly). It gets its yellow colour from fat cells (adipocytes) that occupy most of the space of the yellow bone marrow framework.

Kerma (K)

Quantity for uncharged ionising particles, defined by the quotient of dE_{tr} by dm, where dE_{tr} is the mean sum of the initial kinetic energies of all the charged particles liberated in a mass (dm) of a material by the uncharged particles incident on dm, thus:

$$K = \frac{\mathrm{d}E_{\mathrm{tr}}}{\mathrm{d}m}$$

The unit for kerma is joule per kilogramme (J kg^{-1}) and its special name is gray (Gy).

Kerma approximation

Kerma is sometimes used as an approximation to the absorbed dose. The numerical value of the kerma approaches that of the absorbed dose to the degree that charged-particle equilibrium exists, that radiative losses are negligible, and that the kinetic energy of the uncharged particles is large, compared to the binding energy of the liberated charged particles.

Marrow cellularity

The fraction of bone marrow volume in a given bone that is haematopoietically active. Age- and bone-site-dependent reference values for marrow cellularity are given in Table 41 of *Publication 70* (ICRP, 1995b). As a first approximation, marrow cellularity may be thought of as 1 minus the fat fraction of bone marrow.

Mean absorbed dose in an organ or tissue, D_T

The mean absorbed dose in a specified organ or tissue T, is given by

$D_T = 1/m_T \int D \, dm$,

where m_T is the mass of the organ or tissue, and D is the absorbed dose in the mass element (dm). The SI unit of mean absorbed dose is joule per kilogramme (J kg^{-1}), and its special name is gray (Gy).

Mean free path (mfp)

The average distance travelled by a particle without suffering a collision.

Operational quantities

Quantities used in practical applications for monitoring and investigating situations involving external exposure and intakes of radionuclides. They are defined for measurements and assessment of doses in the body.

Organ absorbed dose

Short phrase for 'mean absorbed dose in an organ or tissue'.

Organ equivalent dose

Short phrase for 'equivalent dose in an organ or tissue'.

Physical half life

The period of time for one-half of the atoms of a radionuclide to disintegrate.

Protection quantities

Dose quantities related to the human body that ICRP has developed for radiological protection to allow quantification of the detriment to people from exposure to ionising radiation from both whole and partial body external irradiation and from intakes of radionuclides.

Quality factor, Q

The quality factor at a point in tissue, is given by

$$Q = \frac{1}{D} \int_{L=0}^{\infty} Q(L) D_L \, dL$$

where D is the absorbed dose at that point, D_L is the distribution of D in unrestricted linear energy transfer L at the point of interest, and $Q(L)$ is the quality factor as function of L. The integration is to be performed over D_L, due to all charged particles, excluding their secondary electrons.

Radiation weighting factor, w_R

A dimensionless factor by which the organ or tissue absorbed dose is multiplied to reflect the higher biological effectiveness of high-linear energy transfer (LET) radiations compared with low-LET radiations. It is used to derive the equivalent dose from the absorbed dose averaged over an organ or tissue.

Red (bone) marrow

See 'Active (bone) marrow'.

Reference Male and Reference Female (Reference Individual)

An idealised male or female with characteristics defined by ICRP for the purpose of radiological protection, and with the anatomical and physiological characteristics defined in *Publication 89* (ICRP, 2002).

Reference Person

An idealised person, for whom the equivalent doses to organs and tissues are calculated by averaging the corresponding doses of the Reference Male and the Reference Female. The equivalent doses of the Reference Person are used for the calculation of effective dose.

Reference phantom

The computational phantom of the human body (male or female voxel phantom based on medical imaging data), defined in *Publication 110* (ICRP, 2009a) with anatomical and physiological characteristics defined in *Publication 89* (ICRP, 2002).

Reference value

Value of a quantity recommended by ICRP for use in dosimetric applications or biokinetic models. Reference values are fixed and specified with no uncertainty, independent of the fact that the basis of these values includes many uncertainties.

Relaxation mass per unit area

Activity concentrations in soil in many instances are described by a depth-dependant exponential function of the form $A = \exp(-z/\beta)$ where A is the activity concentration, z is the soil depth, and β is a parameter called the relaxation mass per unit area. The magnitude of beta is an indication of the radionuclide penetration in the soil with large values of β indicating a steeper exponential distribution. The unit of relaxation mass per unit area is g cm^{-2}.

Response function

See 'Dose response function'.

Soil contamination, ground source

A source describing deposited radionuclides on the surface and in the soil.

Spongiosa

Term referring to the combined tissues of the bone trabeculae and marrow tissues (both active and inactive) located beneath cortical bone cortices across regions of the axial and appendicular skeleton. Spongiosa is one of three bone regions defined in the *Publication 110* (ICRP, 2009a) reference phantoms, the other two being cortical bone and medullary marrow of the long bone shafts. As the relative proportions of trabecular bone, active marrow, and inactive marrow vary with skeletal site, the homogeneous elemental composition and mass density of spongiosa are not constant but vary with skeletal site [see Annex B of *Publication 110* (ICRP, 2009a)].

Tissue reaction

Injury in populations of cells, characterised by a threshold dose and an increase in the severity of the reaction as the dose is increased further. Tissue reactions are also termed 'deterministic effect'. In some cases, these effects are modifiable by post-irradiation procedures including biological response modifiers.

Tissue weighting factor, w_T

A factor by which the equivalent dose in an organ or tissue T is weighted to represent the relative contribution of that organ or tissue to the total health detriment resulting from uniform irradiation of the body (ICRP, 1991). It is defined such that:

$$\sum_{\mathrm{T}} w_{\mathrm{T}} = 1 \cdot$$

Voxel phantom

Computational anthropomorphic phantom based on medical tomographic images in which the anatomy is described by small three-dimensional volume elements (voxels). Collections of these voxels are used to specify the organs and tissues of the human body.

Yellow (bone) marrow

See 'Inactive (bone) marrow'.

Water immersion

External exposure from radionuclides in the radioactive water.

1. INTRODUCTION

(1) In the environment, the public is exposed to various external radiation sources such as naturally occurring radionuclides in soil and other environmental media, as well as cosmic radiation originating from solar particle events and galactic cosmic rays. Moreover, small quantities of radionuclides are discharged from nuclear facilities into the environment under routine operations, leading to small but constant exposures to the public. In the case of a major nuclear facility accidents, potentially large quantities of radionuclides could be released into the environment, resulting in wide geographic regions of contamination. Such was the case following the nuclear power plant (NPP) accidents in Chernobyl, Ukraine in 1987 and in Fukushima Prefecture, Japan in 2011. Both resulted in exposures to members of the general public, with the former being substantially more significant than the latter. In such cases, accurate evaluation of radiation doses to the exposed public is essential to estimate the impact of the accident and to take appropriate radiological protection measures.

(2) External exposure to environmental sources is an important pathway of exposure of the public after major releases of radionuclides to the environment. In the early stage after a nuclear accident, internal exposures due to inhalation and ingestion of radionuclides are likely to significantly contribute to organ equivalent and effective dose, together with external dose contributions from submersion within the radioactive cloud or plume, depending on many factors, such as the regional weather conditions. However, sometime after an accidental release, and if appropriate restrictions of foodstuffs based on reliable measurements are implemented, external exposures become the dominant contributor to the radiation dose to members of the public. As shown in Fig.1.1, this was specifically the case following the accident at the nuclear power plant in Fukushima Prefecture in 2011.

(3) Age-dependent dose coefficients for internal exposures have been evaluated comprehensively by ICRP in *Publications 56*, *67*, *69*, *71*, and *72* (ICRP, 1990, 1993, 1995a,c, 1996a), with recent revisions for adult exposures released as part of the OIR (Occupational Intakes of Radionuclides) (ICRP, 2015, 2016b, 2017). However, to date, reference values of age-dependent dose coefficients for external environmental exposures have not been evaluated by ICRP. In this *publication*, environmental radionuclide external exposures to the full range of ICRP reference individuals is addressed, as age-dependent dose rate coefficients are essential in dose evaluations from environmental exposures.

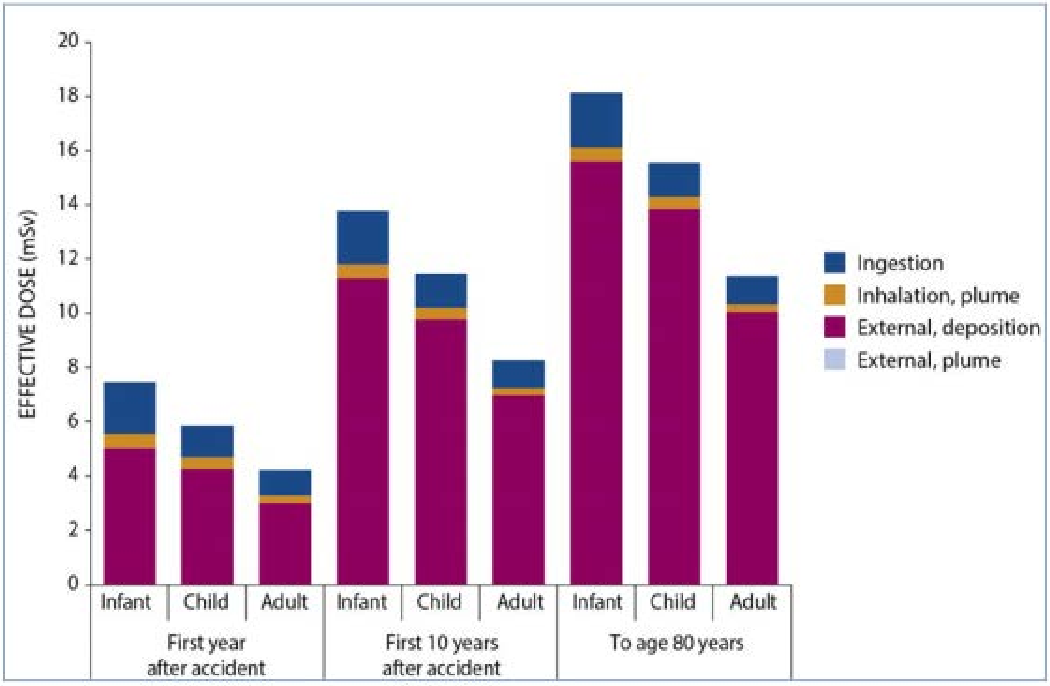

Fig. 1.1 Estimated district-averaged effective doses to adults, children and infants, living in Fukushima city (from UNSCEAR (2013)).

(4) The current ICRP system of radiological protection uses a generalised, gender and age averaged set of tissue and radiation weighting factors to convert organ absorbed dose to organ equivalent dose and then to the effective dose, *E*. While doses incurred at low levels of exposure may be measured or assessed with reasonable accuracy, the associated risks are uncertain. However, bearing in mind the uncertainties associated with risk projection to low doses, it is considered reasonable to use *E* as an approximate indicator of possible risk, with the additional consideration of variations in risk with age, sex, and population group (ICRP *publication* on Effective Dose, in preparation). *E*, according to *Publication 103* (ICRP, 2007), is calculated for sex-averaged Reference Persons at specified ages. *Publication 103* definition includes the specification of reference male and female anatomical models for radiation transport calculations. While exposures may relate to individuals or population groups, *E* is calculated for Reference Persons exposed in the same way.

(5) Organ equivalent doses depend on body size, and so dose rate coefficients for the adult are not adequate for the assessment of doses to children. However, tissue weighting factors and radiation weighting factors are approximate values determined by judgment based on in-vivo and other radiobiology or radiation epidemiological studies.

(6) For external exposures to environmental sources, the dosimetric quantities of interest are the radiation doses received by the radiosensitive organs and tissues of the body due to photons and electrons emitted by radionuclides distributed in soil, air or water. The types of radiation considered are those of importance for external exposure by radionuclides: photons including bremsstrahlung and electrons including beta particles. The neutron dose from radionuclides released to the environment after a nuclear accident is considered to be negligible. Also, neutrons as well as muons from cosmic radiation are not dealt with in this *publication*. If there is a need to estimate doses from cosmic radiation the reader is referred to the study by Sato (2016).

(7) The geographic pattern of radionuclide distribution in air or soil is dependent on time and duration of release, deposition pathways, the chemical form of released radionuclides, and on prevailing meteorological conditions at the time of the release. The latter can include the wind direction and any rainfall or snowfall occurring during the passage of the plume. For a routine or extended release, wind direction can be expected to vary over time. In the longer term, rainfall, snowfall, and weathering will allow penetration of deposited radionuclides into soil and some migration via water pathways or through resuspension. The deposition densities of released radionuclides are often quite heterogeneous. Generally in the longer term, one or a few radionuclides will dominate as the principal contributors to human exposure (such as ^{137}Cs and ^{134}Cs as in the case of the Fukushima NPP accident) (UNSCEAR, 2008, 2013; ICRP, 2009b; Saito et al., 2015).

(8) Soil contamination is the most important source in large-scale accidents since deposited radionuclides continue to expose member of the general public over wide geographical regions for long time periods (UNSCEAR, 2008, 2013; Mikami et al., 2015; Saito et al., 2015). Deposited radionuclides in the ground with respect to depth (via leaching) may be represented sometime after the accident by an exponentially decreasing concentration profile from the soil surface; moreover, the so-called relaxation mass per unit area (in units of g cm^{-2}), is an indicator of radionuclide migration into the ground and is observed to increase with elapsed time since initial soil deposition (ICRU, 1994; Matsuda et al., 2015). Further, the deposited radionuclides could have various concentration profiles – mostly exponential or profiles exhibiting a peak at a certain soil depth that can be approximated by a hyperbolic secant function (Matsuda et al., 2015). Since it is not possible to simulate all possible soil-depth distributions, simulations for planar sources at fixed depths below the ground surface can provide the basic data to enable the reconstruction of diverse and complex radionuclide sources with different depth profiles. A similar approach was employed by Eckerman and Ryman (1993) and by the ICRU (1994) where dose rate coefficients for planar sources were convoluted to approximate any specific or desired radionuclide concentration soil depth profile.

(9) Similarly, the source conditions following a radioactive release in air could change in various ways according to the prevailing and time-dependent meteorological conditions. Near the release point, the radionuclide concentrations in air are often modelled by Gaussian distributions perpendicular to the wind axis (Gaussian plume model), and typical metrological conditions are classified into several categories due to atmospheric turbulence conditions and temperature-altitude profiles. The degree of radionuclide dispersion could be entirely different according to these meteorological conditions; therefore, the relation of dose rates attributed to radionuclide concentrations and their distributions in air can vary greatly. Consequently, it is not practical to evaluate dose rate coefficients to cover all possible diverse conditions. At locations sufficiently far from the release point, the radionuclide distributions in air could be approximated to be uniform and the hemispherical submersion model is considered to be a good approximation at all exposure locations due to the rapid homogenisation of the radioactive material in air.

(10) Water immersion might be rare in the pathway of environmental exposure; however, radioactive releases to the oceans and seas, or the contamination of surface waters have been observed following major radiological accidents. In a large accident, aquatic systems such as rivers, ponds, and seas might be contaminated, and inhabitants might be immersed in water containing radionuclides. Generally, it is anticipated that exposure from water immersion is not significant in most cases, but in order to be able to evaluate such exposures, dose rate coefficients for water immersion are also needed.

(11) A number of publications have reported dose rate coefficients for external irradiation of the body for monoenergetic sources or for radionuclides distributed in the environment (Dillman, 1974; Poston and Snyder, 1974; O' Brien and Sanna, 1976; DOE, 1988; Petoussi et al., 1989, 1991; Jacob et al., 1990; Saito et al., 1990, 1991, 1998; Eckerman and Ryman, 1993; Zankl et al., 2002; Petoussi-Henss and Saito, 2009). Most of the above publications are based on mathematical computational phantoms, mainly of adults. Data on organ equivalent doses for external exposures to the newborn and children are scarce. The first calculated data based on voxel computational phantoms stemmed from work published in Saito et al. (1990), Jacob et al (1990) and Petoussi et al. (1991), who computed the dose rate coefficients for a baby of 8 weeks of age and for a 7-year-old child.

(12) After 2011, many research studies re-visited these calculations using current and more state-of-the-art Monte Carlo methods and anatomic phantoms. An update of the work of Saito et al. (1990) and Jacob et al (1990) can be found in Petoussi-Henss et al. (2012). Saito et al. (2012) estimated effective dose rate coefficients, assuming an exponential distribution of radioactivity in the ground and over a wide range of depths for both adults and the newborn. Yoo et al (2013a,b) presented nuclide-specific dose rate coefficients for air submersion, ground surface contamination, and water immersion exposure situations for the ICRP adult reference phantoms. Satoh et al (2015) presented dose rate coefficients for exposure to both ^{134}Cs and ^{137}Cs for different age-groups using both the ICRP adult reference phantoms and the University of Florida paediatric NURBS-based computational phantoms. Bellamy et al (2016) employed age-specific mathematical phantoms for calculations of effective dose rates for submersion in radioactive air, and for water immersion. Veinot et al (2017) computed these values for the same phantoms following exposure to contaminated soil.

(13) The purpose of the present report is, therefore, to provide ICRP reference age-dependent dose rate coefficients for external exposures to environmentally present radionuclides as needed for both prospective and retrospective radiological protection assessment to exposed populations of children and adults. Experience from post-accident situations suggests that there is broad public concern that children are more at risk from radiation exposure than adults, and that the protection of children in particular is of high importance to the population, and consequently, for radiological protection. The variability of organ equivalent dose with gender, body size, and age has been demonstrated by investigations covering various types of external exposures (Zankl et al., 2002; Johnson et al., 2009; Cassola et al., 2011; Petoussi-Henss et al., 2012; Lv et al., 2017).

(14) Today the main method for assessment of absorbed doses in the human body from external radiation fields is by the application of Monte Carlo radiation transport methods. The simulation results are then expressed in terms of organ equivalent dose rate coefficients giving the organ equivalent dose rate per unit of environmental activity concentration, or external dose rate measurement. Hereafter in this *publication*, they will be referred to as dose rate coefficients, or simply as coefficients.

(15) For simulating the exposure to fields of environmental radiation, the following three typical cases of environmental sources have been addressed in this report: (1) soil (ground) contamination, simulated as fully infinite planar sources on the ground surface and at selected depths below the ground surface; (2) air submersion, simulated as a semi-infinite volume source of radionuclides in air; and (3) water immersion, simulated as a fully infinite radionuclide source in water. The dose rate coefficients have been computed for the ICRP voxel-based adult male and female reference computational phantoms (ICRP, 2009a) as well as for the 10 paediatric NURBS-based phantoms of the University of Florida/National Cancer Institute series (Lee et al., 2010). The latter are voxelized computational phantoms and have

been selected, following specific modifications, to become the reference ICRP paediatric phantoms (Bolch et al., 2016; Chang et al., 2017).

(16) Computations performed for soil contamination and submersion to contaminated air were carried out in three distinct steps: Step 1 involves radiation transport of monoenergetic particles from the contaminated environment (soil or air) to a virtual cylinder surrounding the exposed individual subsequently referred to as the 'coupling cylinder'; Step 2 involves transport of the primary and secondary radiation particles recorded on the surface of the coupling cylinder into the phantom; Step 3 entails spectrum weighting of the resultant organ equivalent doses to yield radionuclide-specific dose rate coefficients. Additional simulations under Step 2 include the placing of an air sphere for tallying air kerma and ambient dose equivalent rates at a height of 1 m above the ground surface. This additional step is needed in order to report organ and effective dose rate coefficients both in terms of environmental radionuclide concentration, but also in terms of these measured quantities. Separation of Steps 1 and 2 significantly improves the calculation efficiency and statistical accuracy of the computed results, because the same radiation fields recorded at the coupling cylinder can be repeatedly used for different exposed computational phantoms. For water immersion, the organ equivalent dose rate coefficients for monoenergetic particles were computed directly, without the use of the coupling cylinder.

(17) The expected applications of the dose rate coefficients are: (a) pre-accidental evaluations in order to predict the possible impacts to the public by postulated radiological accidents, (b) post-accidental evaluations to estimate doses in order to develop a radiological protection strategy for the exposed populace, (c) evaluations following discharge of radionuclides from nuclear and radioisotope facilities during routine operations, and (d) evaluations of naturally occurring radionuclides in the environment. The pre/post-accident analyses are performed typically by software packages (e.g. codes for severe accidents). The software predicts the dispersion, migration, and distribution of radionuclides in the environment. The dose rate coefficients of the present publication can thus be implemented in these codes.

(18) It should be noted that dose rate coefficients are calculated for idealised and hypothetical source geometries such as semi-infinite and uniform distributions, for reference phantoms wearing no clothing, and for an idealised, upright postures, even for the exposed newborn. As a result, they do not fully reflect actual exposures for a particular situation and exposed individual.

2. SCHEMA FOR DOSE ASSESSMENT FROM ENVIRONMENTAL EXPOSURE

(19) Dose rate coefficients are needed to evaluate effective dose from measurable quantities such as radioactivity concentrations (i.e., surface activity density and air activity density), air kerma rate, absorbed dose rates in air, or ambient dose equivalent rates. These quantities are mostly obtained from environmental measurements but also from evaluation using computational models or computer simulations. Calculation of dose rate coefficients requires the evaluation of the environmental field (i.e., exposure geometry, density and composition of soil and air, and radionuclide concentration depth profiles), anatomic models of the human body (i.e., reference phantoms for various members of the general public), and the simulation of the radiation transport through the environment and into the body of the exposed individual. Organ equivalent doses depend on body size since, in external exposures, increasing amounts of overlying muscle and adipose tissue enhances the shielding of deeper seated radiosensitive organs (ICRP, 2010). Furthermore, the characteristics of radiation fields change with height above ground soon after the deposition, especially for sources on and in the ground, and thus the body height, and extension the differing locations of radiosensitive internal organs, can impact the magnitude of assessed organ equivalent dose. For example, in the early stages after the accident in Fukushima nuclear power plant, it was reported that the dose rate in air at 0.5 m height was higher than that at 1 m, which caused many concerns regarding the reliable evaluation of exposures to children.

(20) Fig. 2.1. shows a schematic representation of the evaluation of organ equivalent and effective dose rates in the environment. The measurable quantities used mostly for the evaluation of exposures in the environment are the radionuclide concentration in the soil, air, or water, and the dose rates in air at 1 m height. To evaluate organ equivalent dose rates or effective dose rates from these quantities, dose (rate) coefficients are necessary. Generally, there are three methods for dose assessment for external environmental exposures, as shown in Fig. 2.1.

(21) The first method (DC1 in Fig. 2.1) is the direct conversion from radionuclide concentration in the environmental media such as soil, air, and water. The radionuclide concentrations, expressed in units of Bq kg^{-1} or Bq m^{-3}, are usually determined by collection and analyses of environmental samples of these environmental media. In case of soil contamination, deposition density per unit area (Bq m^{-2}) is often used because this quantity indicates the contamination level of a location regardless of radionuclide depth profile. Alternatively, in situ measurements using a portable Ge semiconductor detectors are sometimes performed (Mikami et al., 2015). Furthermore, computer modelling could be used to determine the radionuclide concentrations in the environment. For example, simulations of air dispersion enable the analysis of the movement of radionuclides within the environment, and thus provide predicted values of radionuclide concentrations in air and on the ground. For evaluating the exposure, these data need to be related to the effective dose rates or organ equivalent dose rates experienced by exposed individuals located within the vicinity of where the modelled or measured radionuclide environmental concentration is present.

(22) The second method (DC2 in Fig. 2.2) is employing conversions based upon measurement of dose rates in air. Historically, dose rates in air have been measured in terms of air kerma rate or air absorbed dose rate (both in units of Gy h^{-1}). After the introduction of the operational quantity ambient dose equivalent, the ambient dose equivalent rate (in Sv h^{-1}) was also applied to environmental radiation monitoring and has been widely used. An enormous amount of air dose rate data has been accumulated in terms of Gy h^{-1} and Sv h^{-1}, and these data are converted to effective dose and equivalent dose rates with dose rate

coefficients expressed in units of Sv Gy^{-1} or Sv Sv^{-1}. UNSCEAR (2013) has used the value of 0.7 for conversion from air absorbed dose (Gy) to effective dose (Sv). This is considered to be a representative value for adults; however, this value could change according to the source distribution, energy spectrum and age of exposed individual. For example, this value is obviously lower for low energy photon sources. It must be noted that ambient dose equivalent needs also to be converted to effective dose for appropriate dose evaluations in the environment even though the units are the same (i.e. Sv h^{-1}). After the radiological accident in the Fukushima NPP, ambient dose equivalent was often erroneously regarded to be equal to effective dose without the application of any dose rate coefficients, and this resultantly led to overestimation of exposure doses to members of the public.

(23) The third method (DC3 and then DC2) demonstrated in Fig. 2.1 is employed when the estimation of dose rates in air (i.e. absorbed dose rates in Gy h^{-1} and ambient equivalent dose rates in Sv h^{-1}) is necessary in addition to the estimation of effective dose and equivalent dose rates (Sv h^{-1}). From a viewpoint of environmental radiation monitoring, the measured dose rate in air at 1 m height is a very important quantity and can be compared with the value calculated using method DC3. To calculate the effective or equivalent dose a two-step approach, DC3 followed by DC2, can be used. First, the radionuclide concentration in the environment (Bq m^{-2} or Bq m^{-3}) is converted to dose rate in air at 1 m height using DC3 and then the dose rate in air can be converted to effective dose and equivalent dose rate with DC2. In principle, the effective dose and equivalent dose rates obtained by the two-step method provide similar values to those which would have been obtained directly using DC1 given the same initial conditions.

(24) If the source conditions are not typical and DC3 cannot provide reliable estimation of dose rates in air, and if direct measurements are difficult, a modified two-step approach could be applied. First, dose rates are evaluated taking into account the specific conditions of the contamination situation, then the evaluated air dose rates are converted to effective dose and equivalent dose rates using DC2. This approach was used after the Fukushima NPP accident, for cases where the deposition density per unit area and depth profile of radionuclides deposited on the ground varied significantly with location, especially if decontamination was performed. In such complex contamination conditions, dose rates in air in terms of ambient equivalent dose rate are evaluated, taking into account precisely the horizontal and vertical distribution of radioactive caesium, as performed by Malins et al. (2016) who aimed at investigating the efficiency of decontamination work postulating different decontamination methods and extents. The dose rate in air obtained in this way could be further converted into effective dose or equivalent dose rates by applying DC2, which is an approach less sensitive to source distribution.

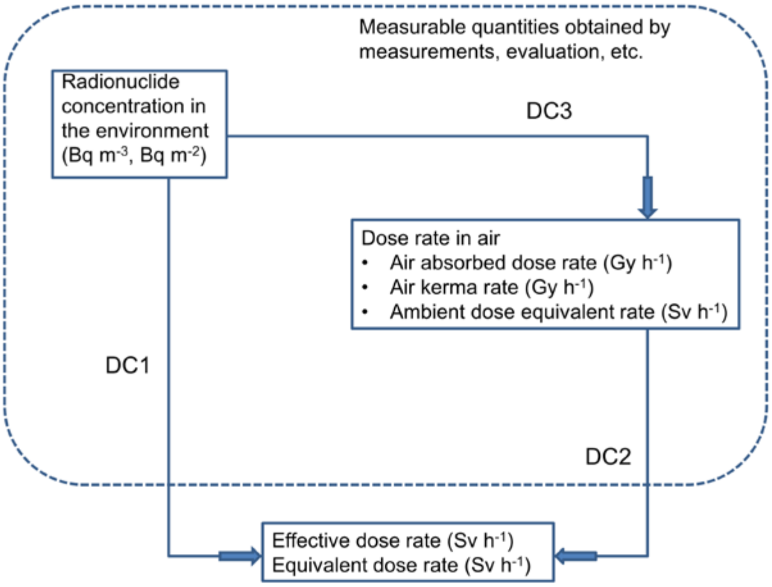

Fig. 2.1. Schematic representation of evaluation of effective and organ equivalent dose rates in the environment. DC1-DC3 indicate the different methods of dose evaluation, as explained in section 2.

3. DOSIMETRIC QUANTITIES USED IN RADIOLOGICAL PROTECTION

3.1. Organ absorbed dose and equivalent dose

(25) The mean absorbed dose averaged over the volume of organs and tissues is the primary scientific quantity from which effective dose, *E*, is calculated. Absorbed dose (*D*) is defined as the quotient of mean energy $\mathrm{d}\bar{\varepsilon}$, imparted by ionising radiation in a volume element and the mass, d*m*, of the matter in that volume:

$$D = \frac{\mathrm{d}\bar{\varepsilon}}{\mathrm{d}m} \qquad (3.1)$$

(26) The SI unit of absorbed dose is J kg^{-1} and its special name is gray (Gy). Absorbed dose is derived from the mean value of the stochastic quantity of energy imparted, ε, and does not reflect the random fluctuations of the interaction events in tissue. While it is defined at any point in matter, its value is obtained as an average over a mass element d*m* and hence over many atoms or molecules of matter.

(27) When using the quantity absorbed dose in radiological protection, doses are averaged over tissue volumes. It is assumed that for low doses, the mean value of absorbed dose averaged over a specific organ or tissue can be correlated with radiation detriment for stochastic effects in that tissue with an accuracy sufficient for the purposes of radiological protection. The averaging of absorbed dose is carried out over the volume of a specified organ (e.g. liver) or tissue (e.g. active bone marrow) or the sensitive region of a tissue (e.g. endosteal surfaces of the skeleton). Absorbed dose *D* is used to set limits on organ/tissue doses to prevent tissue reactions (deterministic effects).

(28) Equivalent dose, H_T to a tissue or organ is defined as:

$$H_\mathrm{T} = \sum_\mathrm{R} w_\mathrm{R} D_\mathrm{T,R} \qquad (3.2)$$

where w_R is the radiation weighting factor for radiation type R, and $D_{T,R}$ is the organ absorbed dose from radiation type R in a tissue or organ T of the age-specified Reference Male or Female. Since w_R is dimensionless, the SI unit for the equivalent dose is the same as for absorbed dose, J kg^{-1}, and its special name is sievert (Sv). Values of w_R are shown in Table 3.1 and are taken from *Publication 103* (ICRP, 2007).

Table 3.1. ICRP radiation weighting factors.

Radiation Type	Radiation Weighting Factor, w_R
Photons	1
Electrons and muons	1
Protons and charged pions	2
Alpha particles, fission fragments, heavy ions	20
Neutrons	Continuous function of neutron energy See Eqn. 4.3 of *Publication 103*

3.2. Effective dose

(29) The effective dose, E, introduced in *Publication 60* (ICRP, 1991) is the risk-related quantity in radiation protection and is defined as a weighted sum of tissue equivalent doses. In accordance with the definition of effective dose in *Publication 103* (ICRP, 2007), the effective dose is computed as:

$$E = \sum w_T \left[\frac{H_T^M + H_T^F}{2}\right] \qquad (3.3)$$

where H_T^M and H_T^F are the equivalent doses to the tissues or organs T of the Reference Male and Female, respectively, and w_T is the tissue weighting factor for target tissue T, with $\Sigma w_T = 1$. The sum is performed over all organs and tissues of the human body considered to be sensitive to the induction of stochastic effects. Values of w_T are given in Table 3.2. (ICRP, 2007). Since w_R and w_T are dimensionless, the SI unit for effective dose is the same as for absorbed dose, J kg^{-1}, and its special name is Sievert (Sv).

(30) Effective dose (E) was originally introduced for the control of occupational exposures to external and internal sources of radiation. While the concept has remained essentially unchanged through *Publication 60* (ICRP, 1991) to *Publication 103* (ICRP, 2007), its use has been extended to members of the public of all ages, including in utero exposures of the foetus (ICRP, 2001, 2004, 2006).

(31) ICRP provides effective dose coefficients for situations of external and internal exposures of workers and members of the public, and for radiopharmaceutical administrations to patients, as reference values for use in prospective and retrospective dose assessments.

Table 3.2. ICRP tissue weighting factors (ICRP, 2007).

Tissue	w_T	$\sum w_T$
Bone-marrow, breast, colon, lung, stomach, remainder tissues *(13*)*	0.12	0.72
Gonads	0.08	0.08
Urinary bladder, oesophagus, liver, thyroid	0.04	0.16
Bone surface, brain, salivary glands, skin	0.01	0.04

*Remainder tissues: adrenals, extrathoracic (ET) regions of the respiratory tract, gall bladder, heart, kidneys, lymphatic nodes, muscle, oral mucosa, pancreas, prostate (male), small intestine, spleen, thymus, uterus/cervix (female).

(32) E is calculated for sex-averaged Reference Persons at specified ages as defined in *Publication 89.* The *Publication 103* definition includes the specification of reference male and female anatomical models for radiation transport calculations. While exposures may relate to individuals or population groups, E is calculated for Reference Persons exposed in the same way.

(33) Effective dose (E), in units of sievert (Sv), is accepted internationally as the central radiological protection quantity and is used for regulatory purposes worldwide, providing a risk-adjusted measure of total body dose from both external and internal sources in relation to stochastic risks of cancer and hereditary effects, expressed in terms of detriment. It has proved to be a valuable and robust quantity for use in the optimisation of protection and in setting of control criteria such as dose limits, constraints and reference levels. In its general application, effective dose does not provide an individual-specific dose but it rather applies to a reference

person under the same exposure situation. As such, the effective dose cannot be used for the assessment of individual risk (ICRP, 2007).

3.3. Air kerma

(34) For measuring external radiation, basic physical quantities that relate the radioactivity in the environment with the protection and the operational quantities are required. National and international standards laboratories maintain standards and reference radiation fields that are specified and described in terms of these quantities for calibration of instruments and dosimeters. Air kerma free-in-air, K_{air}, has been used for this purpose (ICRU, 1994, 2014; ICRP, 1996b). In further text throughout this *publication*, the quantity air kerma free-in-air is usually referred to simply as 'air kerma'.

(35) The kerma, K, for ionising uncharged particles, is given by

$$K = \frac{\mathrm{d}E_{\mathrm{tr}}}{\mathrm{d}m} \qquad (3.4)$$

where $\mathrm{d}E_{\mathrm{tr}}$ is the mean sum of the initial kinetic energies of all the charged particles liberated in the mass ($\mathrm{d}m$) of a material by the uncharged particles incident on $\mathrm{d}m$. The unit of kerma is J kg^{-1}, and has the special name gray (Gy). The quantity ($\mathrm{d}E_{\mathrm{tr}}$) includes the kinetic energy of the charged particles emitted in the decay of excited atoms/molecules or in nuclear de-excitation or disintegration.

3.4. Operational quantities

(36) The protection quantities 'organ equivalent dose' and 'effective dose' are not measurable, and therefore cannot be used directly as quantities in radiation monitoring. Operational quantities are thus used for the assessment of the protection quantities (effective dose, or equivalent dose in tissues or organs). The operational quantities aim to provide a reasonable estimate of the values of protection quantities relevant to the exposure of humans to external radiations under most irradiation conditions (ICRU, 1985, 1988, 1993).

(37) The operational quantities are defined using the quantity dose equivalent, H (ICRU, 1985). H is the product of Q and D at a point in tissue; thus, $H = QD$, where D is the absorbed dose and Q is the quality factor at that point. Q is defined as a function of unrestricted linear energy transfer (L_∞, often denoted as L or LET) of charged particles in water (ICRP, 1996b).

(38) For area monitoring, two quantities, namely, the ambient dose equivalent, $H^*(d)$, and the directional dose equivalent, $H'(d, \boldsymbol{\Omega})$, are used to link external radiations to the effective dose and to the equivalent dose in the lens of the eye and local skin. $H^*(d)$, at a point in a radiation field, is the dose equivalent that would be produced by the corresponding expanded and aligned field, in the ICRU sphere at a depth (d), on the radius opposing the direction of the aligned field. $H'(d, \boldsymbol{\Omega})$, at a point in a radiation field, is the dose equivalent that would be produced by the corresponding expanded field, in the ICRU sphere at a depth (d) on a radius in a specified direction (**$\boldsymbol{\Omega}$**).

(39) For individual monitoring, the personal dose equivalent, $H_{\mathrm{p}}(d)$, is used. $H_{\mathrm{p}}(d)$ is the dose equivalent in soft tissue, at an appropriate depth, d, below a specified point on the body. The specified point is usually given by the position where the individual's dosimeter is worn.

(40) The recommended values of d are chosen for the assessment of various doses: d =10 mm for effective dose, d = 3 mm for dose to the eye lens, and d = 0.07 mm for dose to the

skin and to the hands and feet. The unit of ambient dose equivalent, directional dose equivalent, and personal dose equivalent is J kg^{-1}, and has the special name sievert (Sv).

4. THE ICRP REFEENCE PHANTOM

4.1. Adult reference computational phantoms

(41) Computational phantoms of the human body – together with radiation transport codes – have been employed for many years in the evaluation of organ equivalent dose rate coefficients in environmental radiation protection. During the last two decades, voxel phantoms were introduced that are derived mostly from (whole body) medical image data of real persons instead of the older mathematical MIRD-type body models. A voxel model (or phantom) is a three-dimensional representation of the human body in the form of an array of identification numbers, arranged in slices, rows, and columns. Each entry in this array represents a tissue voxel; organs are then represented by those voxels having the same identification number and are spatially arranged to represent the organ volume. More information on voxel phantoms, their development and use can be found elsewhere (Xu and Eckerman, 2010).

(42) For the computation of organ absorbed doses, the adult male and female reference computational phantoms, representing the ICRP Reference Adult Male and Reference Adult Female (ICRP, 2007) were used in this report. These phantoms were adopted by ICRP and ICRU as the phantoms for the computation of the ICRP reference dose coefficients and are extensively described in *Publication 110* (ICRP, 2009a). The reference computational phantoms are based on human computed tomographic (CT) data and were constructed by modifying the voxel models (Zankl and Wittmann, 2001; Zankl et al., 2005) of two individuals (Golem and Laura) whose body height and mass closely resembled the reference data. The organ masses of both phantoms were adjusted to the ICRP data given in *Publication 89* (ICRP, 2002) on the Reference Male and Reference Female with high precision, without significantly altering their realistic anatomy. The phantoms contain all target regions relevant to the assessment of human exposure to ionising radiation for radiological protection purposes, including all tissues and organs that contribute to the protection quantity effective dose (ICRP, 2007).

(43) The male reference computational phantom consists of approximately 1.95 million tissue voxels (excluding voxels representing the surrounding vacuum) each with a slice thickness (corresponding to the voxel height) of 8.0 mm and an in-plane resolution (i.e. voxel width and depth) of 2.137 mm, corresponding to a voxel volume of 36.54 mm^3. The number of slices is 220, resulting in a body height of 1.76 m and total body mass of 73 kg. The female reference computational phantom consists of approximately 3.89 million tissue voxels, each with a slice thickness of 4.84 mm and an in-plane resolution of 1.775 mm, corresponding to a voxel volume of 15.25 mm^3. The number of slices is 346, and thus the body height is 1.63 m and the total body mass is 60 kg. The number of individually segmented structures is 136 in each phantom, and 53 different tissue compositions have been assigned to them. The various tissue compositions reflect both the elemental composition of the tissue parenchyma (ICRU, 1992) and each organ's blood content (ICRP, 2002) (i.e. organ composition inclusive of blood). Fig. 4.1 shows frontal (coronal) views of the male (right) and female (left) computational phantom, respectively.

(44) Due to the limited resolution of the source tomographic data upon which these phantoms were constructed, and the very small dimensions of some of the ICRP defined source and target regions, not all tissues could be explicitly represented. In the skeleton, for example, the target tissues of interest are the haematopoietically active bone marrow located within the marrow cavities of spongiosa, as well as the endosteal layer lining the surfaces of

the bone trabeculae and the inner surfaces of the medullary cavities of the long bones (presently assumed to be 50 µm in thickness). Due to their small dimensions, these two target tissues had to be incorporated as homogeneous constituents of spongiosa within the reference phantoms. At lower energies of photon and neutrons, secondary charged-particle equilibrium is not fully established in these tissue regions over certain energy ranges. Consequently, more refined techniques for accounting for these effects in skeletal dosimetry were used in this report, and are discussed more fully within Annex A.

Fig. 4.1. Images of the adult male (right) and adult female (left) computational phantoms (ICRP, 2009a). The following organs can be identified by different surface colours: breast, colon, eyes, lungs, liver, pancreas, salivary glands, small intestine, stomach, thyroid and urinary bladder, testes, teeth. Muscle and adipose tissue are semi-transparent.

4.2. The paediatric phantoms

(45) The series of ten ICRP paediatric computational phantoms are the following:

- Newborn – Male and Female
- 1-year-old – Male and Female
- 5-year-old – Male and Female
- 10-year-old – Male and Female
- 15-year-old – Male and Female

(46) These phantoms were derived from a series of computational phantoms developed originally at the University of Florida (UF) and later in collaboration with the National Cancer Institute (NCI). Consequently, the original phantoms from which the ICRP paediatric phantoms were derived are presently referred to as the UF/NCI phantom series (Lee et al., 2010). The UF/NCI phantoms are of a third generation of phantom technology – hybrid phantoms – in which the outer body contour and internal organ surfaces are modelled using the computer animation techniques of either polygon mesh or NURBS (Non-Uniform

Rational B-Spline) surfaces depending on the complexity of anatomical structures. The polygon meshes are a cluster of adjacent triangles, while the NURBS surfaces are a cluster of 3D points in space between which a surface is interpolated. Within the past few years, computational phantoms in these two formats can be directly used in some Monte Carlo transport codes as necessary. However, most transport codes still utilise a voxel format, composed of tiny cuboidal prisms. A computer script was thus used to convert the UF/NCI hybrid phantoms from their surface format to a voxel format for Monte Carlo simulations conducted in the current *Publication*. These ICRP reference paediatric phantoms in voxel format are thus consistent with the format of the ICRP *Publication 110* reference adult phantoms (ICRP, 2009a).

(47) As noted in Lee et al. (2010), the UF/NCI series of phantoms are traceable directly to real human anatomy. The newborn phantom is based upon full-body CT imaging of a 6-day female cadaver, while the remainder of the paediatric series (1-year-old to 15-year-old phantoms) are based upon combinations of head CT images, full torso CT images, and rescaled CT-based images of adult arms and legs. The latter approach was necessary since medical imaging of children rarely include the arms within the imaging field. From the initial series of segmented images, various anatomic sources were used to resize both internal organ anatomy and exterior body size. The most important document used was *Publication 89* (ICRP, 2002) providing internal organ masses, and values of total weight and height. Additional reference sources were used to target various body circumferential dimensions not given as reference values in *Publication 89*. The final series of the UF/NCI hybrid phantoms thus fully conforms to reference anatomy specified by the Commission and are fully traceable to real human CT anatomy. In this manner, the ICRP paediatric phantom series is fully compatible with the process used to develop the *Publication 110* phantoms, which also were based upon segmentation of real human CT anatomy.

(48) Another unique feature of the ICRP paediatric phantoms (and of the UF/NCI phantoms), is their explicit coupling to microCT based models of skeletal dosimetry. As noted in Hough et al. (2011) and in Johnson et al. (2011), an extensive series of cadaver bone harvests, ex-vivo skeletal CT imaging, and ex-vivo spongiosa core microCT imaging, were used to construct models of tissue dosimetry in the skeletons of the ICRP reference adult phantoms. This work is more formally described Annexes D and E of *Publication 116* (ICRP, 2010). The paediatric series of ICRP reference phantoms similarly have accompanying models of skeletal anatomy at both its macrostructural and microstructural dimensions. Thus, the methods proposed in *Publication 116* (ICRP, 2010) for external photons and neutrons, and in *Publication 133* (ICRP, 2016a) for internal beta and alpha particles, as well as photons, for the ICRP *Publication 110* adult phantoms, are available in reporting skeletal tissue dosimetry to paediatric members of the reference series.

(49) The following further refinements have been made to the UF/NCI series of paediatric phantoms (Pafundi, 2009; Wayson, 2012):

- A sub-segmented skeletal model to include regions of cortical bone, spongiosa, and medullary marrow
- Photon dose response functions for internal and external photon dosimetry to active marrow and endosteum
- New age-specific regional blood distribution model (Wayson, 2012)
- Corresponding model of the major blood vessels
- Separation of subcutaneous fat and skeletal muscle from what was formally residual soft tissues (RST)
- Inclusion of lymphatic nodes - see Lee et al. (2013)

(50) The series of ICRP paediatric reference phantoms are in voxel format, and fully conform to the framework established in *Publication 110* (ICRP, 2009a). All organs and tissue structures modelled in the ICRP *Publication 110* reference adult male and female phantoms are included in the series of ICRP paediatric phantoms with consistent ID numbers (see Annex A of *Publication 110*). Representative images of the ICRP paediatric series are given in Fig. 4.2.

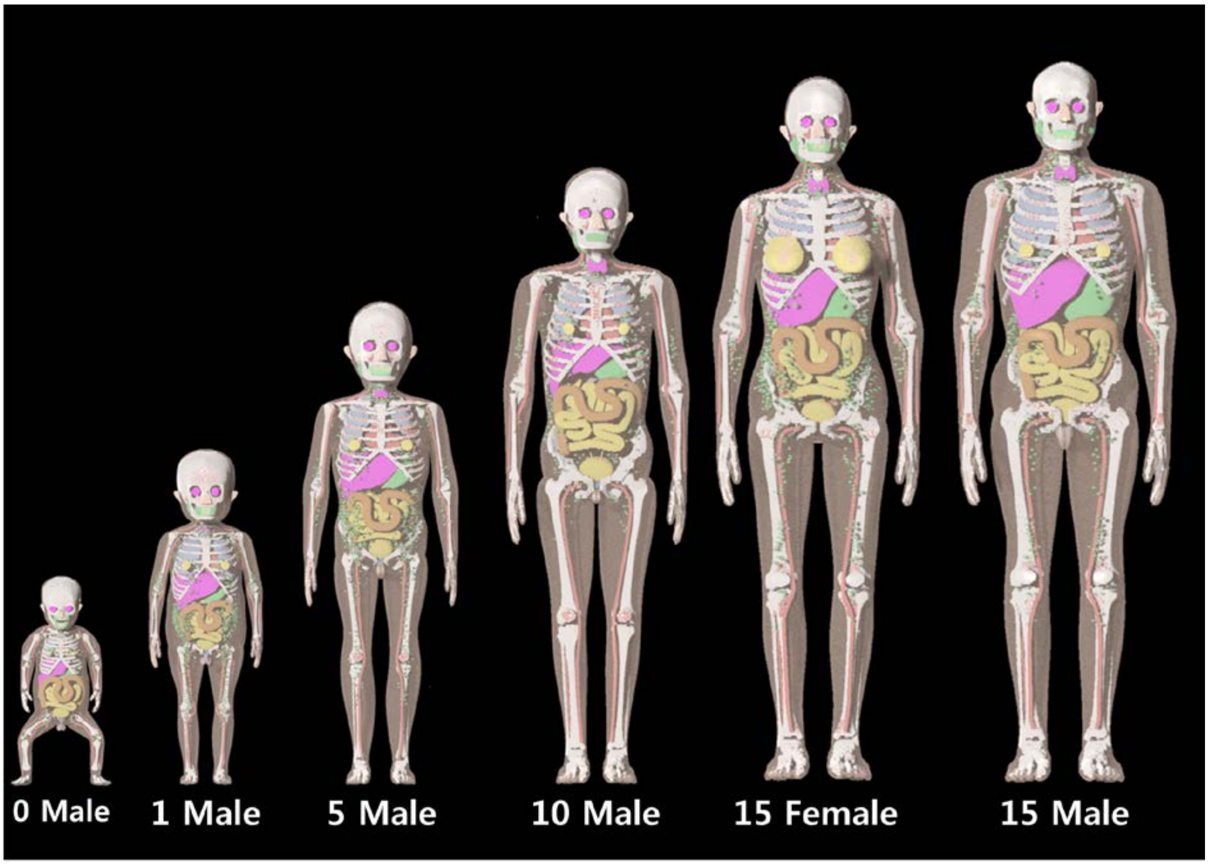

Fig. 4.2. Series of ICRP reference paediatric phantoms. The male and female newborn, 1-, 5- and 10-year-old phantoms are anatomically identical, except for their gonads.

(51) While the ICRP paediatric reference phantoms are identical in format to the ICRP *Publication 110* (ICRP, 2009a) adult phantoms regarding the ID numbers of the various source and target organs, one important difference is the voxel resolution. One of the main advantages of hybrid phantom technology is that in the conversion of the polygon mesh/NURBS format of the phantom to the voxel format of that same anatomy, one can select the voxel resolution. Table 4.1 tabulates the voxel resolutions, array size, and total matrix size finally adopted for the ICRP paediatric phantoms. These ensure continuous conformance with the 1% matching of reference masses as well as conform to reference total skin thickness as given by data in *Publication 89*. It is noted that for the newborn phantom, the voxels are cubic (i.e., same thickness in x, y, and z directions), while rectangular prisms with larger z-dimension than xy-dimensions were adopted for the older phantoms so as to keep the matrix size constant at 55 million voxels in total. In contrast, the ICRP *Publication* 110 adult male and female phantoms have total matrix sizes of 1.9 and 3.9 million voxels, respectively. The need for higher resolution is to preserve organ anatomy in the smaller anatomy of the paediatric reference individuals.

Table 4.1. Voxel resolution, voxel number, and total matrix size of the ICRP paediatric computational phantom series.

Phantom	Resolution (cm)			Array size			Matrix size (million)
	X	Y	Z	X	Y	Z	
Newborn Female	0.0663	0.0663	0.0663	350	215	720	54.2
Newborn Male	0.0663	0.0663	0.0663	350	215	720	54.2
1 –Year Female	0.0663	0.0663	0.1400	396	253	550	55.1
1 –Year Male	0.0663	0.0663	0.1400	396	253	550	55.1
5 –Year Female	0.0850	0.0850	0.1928	424	235	576	57.4
5 –Year Male	0.0850	0.0850	0.1928	424	235	576	57.4
10 –Year Female	0.0990	0.0990	0.2425	432	226	580	56.6
10 –Year Male	0.0990	0.0990	0.2425	432	226	580	56.6
15 –Year Female	0.1200	0.1200	0.2828	408	242	574	56.7
15 –Year Male	0.1250	0.1250	0.2832	416	230	590	56.5

5. SIMULATION OF THE ENVIRONMENTAL RADIATION FIELD (STEP 1)

(52) Photons emitted from sources distributed in the environment are scattered and/or absorbed in both air and soil, and their energy spectrum and angular distribution in air have specific features dependent on the initial energy and spatial distribution of the emission sites. In the case of volumetric sources in air or ground, the angular distribution of incident photons is nearly uniform for the hemisphere from which the source originates, while small amounts of scattered photons emerge from the opposing semi-sphere (Saito et al., 1998). In case of deposited sources in the ground, the dominant component of photons is incident along horizontal directions. Monte Carlo method is a suitable tool able to simulate the particle transport and the detailed environmental conditions.

(53) For simulating the exposure to environmental radiation, the following three typical cases of environmental sources have been addressed in this report: (1) soil (ground) contamination, simulated as fully infinite planar sources on the surface and at different depths in the ground; (2) air submersion, simulated as a semi-infinite volume source in air; and (3) water immersion, simulated as a fully infinite source in water. The first source simulates the deposition of radionuclides on and below the ground surface, by assuming an infinite planar source on the surface and in the soil. The second source configuration models the gaseous radioactive release into the atmosphere at locations which are not too near to the release point, by assuming a homogeneous contamination of the air in a semi-spherical region above a smooth air-ground interface of radius whose dimension depends on the mean free path of the photons of interest. The third source simulates immersion in uniformly contaminated water. For the first and second source configurations, the human body is assumed to be standing up-right on the ground, while for water exposures, the human body is assumed to be fully immersed.

(54) The transport of radiation particles in the environment was simulated using the Monte Carlo simulation package Particle and Heavy Ion Transport code System (PHITS) (Sato et al., 2013). PHITS is a multi-purpose Monte Carlo code that simulates the transport and interaction of hadrons, leptons, and heavy ions in arbitrary three-dimensional geometries. Version 2.66 of the PHITS code was used in this report (Sato et al., 2013). For simulating photon and electron transport, respectively, the atomic data libraries MCPLIB04 (White, 2003) and EL03 (Adams, 2000) were employed. These libraries provide precise cross-section data and can treat various physical processes of both photons and electrons.

(55) PHITS defines the geometry of the calculation model in terms of the combinatorial geometry (CG) and the general geometry (GG). In addition, a capability for describing repeated structures and lattice geometries is available to define three-dimensional voxel phantoms. PHITS has a function to draw 2-dimensional and 3-dimensional figures of the calculation geometries as well as the computed data results using a graphic package ANGEL (Niita et al., 2010).

(56) In the environmental radiation transport simulation for photon sources, only photons were transported and secondary electrons generated by photon interactions were not followed. This is because the secondary electrons lose their energies continuously and stop within a short distance in the environmental media. However, bremsstrahlung photons generated by secondary electrons have maximum energies comparable to those of the secondary electrons and are able to propagate across long distances. The production of the bremsstrahlung photons, and their energy and emission angle were sampled at the interaction point based on a thick-target bremsstrahlung approximation model (MCNP, 2003). For electron sources, both the primary electrons and their secondary photons were transported in the environment.

(57) As previously mentioned, the radiation field computed due to monoenergetic radiation emissions from within the contaminated air and soil was expressed as the position, angle of incidence, and energy of the particles incident on the surface of a virtual cylinder of 2 m height and 0.6 m diameter, which surrounds the exposed individual, and is termed the coupling cylinder. As the phantom was not present in this first step, the same coupling cylinder source could be applied for all phantoms. Saito et al (1990) had previously examined the perturbation of the photon fields on the human body and found it to be insignificant under the conditions considered above. Fig. 5.1 shows schematically which particles were recorded on the surface of the coupling cylinder.

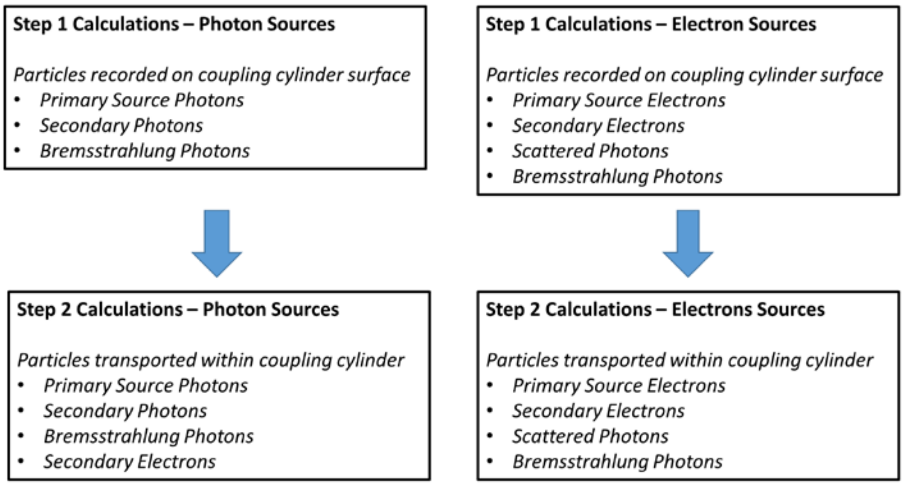

Fig. 5.1. Schematic representation of particle transport during Step 1 and Step 2 of the calculation.

(58) To cover the wide energy range of radiations that are emitted by many different radionuclides, the monoenergetic photon and electron energies considered were varied from 0.01 to 8 MeV.

5.1. Soil contamination

(59) Soon after deposition, radionuclides deposited on the ground are assumed to form a planar source at the ground surface. Over time, these radionuclides will migrate or leach into the soil thereby developing diverse concentration depth profiles in terms of both shape and degree of soil penetration (Matsuda et al., 2015). In many cases, the distribution of radionuclides with respect to soil depth could be approximated as being due to many infinite planar sources within the ground. These functions could have various characteristics, showing peaks at different depths in the soil. Since it is not practical to simulate every radionuclide/soil migration function, the simulation of a series of planar radiation sources at different depths can provide basic data enabling one to extrapolate or interpolate these results to model diverse source profiles within the contaminated ground.

(60) The air-over-ground geometry was modelled such as air bounds on the ground with an infinite flat surface. In the real environment, the terrain is not normally flat nor infinite; however, the infinite flat terrain could well represent most real situations for dose evaluation.

For example, in case of an exponentially distributed ground source with a relaxation mass per area of 1 g cm^{-2}, which is a typical depth observed soon after radionuclide ground deposition, approximately half of the measured ambient dose equivalent at 1 m height is attributed to photons from sources within a radius of 5 m in the ground (Malins et al., 2016). Thus, a limited series of flat ground surface areas is considered to adequately model the exposure for many real exposure situations.

(61) The monoenergetic radioactive sources were defined as planar sources at depths in soil expressed in terms of mean free paths (mfp) of photons in soil: 0.0 (i.e. the contamination is on the surface), 0.2, 1, 2.5 and 4 mfp. For most exposure situations, the consideration of mean free paths up to 4 would be sufficient (Eckerman and Ryman, 1993); however, the source depth profile might be changed, due to, for example, ploughing. Thus, dose rate coefficients for a wider range of mean free paths would be useful and had been therefore considered to facilitate an accurate integration when determining dose rate coefficients for continuous source-depth profiles. The air-ground interface (0 mm) is a flat planar source without any soil covering the source. This is an idealised geometry and does not exist in reality, as there is a variety of factors that provide shielding from ground surface sources. These include the presence of vegetation, surface roughness, and particle movement due to gravitational forces (Burson and Profio, 1977; Kocher and Sjoreen, 1985; Jacob and Paretzke, 1986). Furthermore, the depth of 0.5 g cm^{-2} was considered, as representative of the surface roughness and initial migration following precipitation. It simulates the deposition of radionuclides in the ground the first years after migration (ICRU, 1994). This source depth is consistent with earlier work by Saito et al. (1990) and Petoussi et al. (1991) and with the recent work of Petoussi-Henss et al. (2012), Yoo et al. (2013a), Bellamy et al. (2018). It has been also shown previously that for a ^{137}Cs/^{137m}Ba source distributed as a planar source at a depth of 0.5 g cm^{-2}, the air kerma in air is reduced by a factor of 0.67, compared to a purely surface planar source on the ground (UNSCEAR, 2016). Therefore, in the present report, dose rate coefficients for contaminated ground planes are presented for surface contamination, contamination at depths expressed as mfp, as described before, as well as for a planar source at depth of 0.5 g cm^{-2} which is equivalent to 3 mm of soil with density of 1.6×10^3 kg m^{-3} representing the ground roughness.

(62) Fig. 5.2 (left) shows schematically the simulation geometry, which consists of a right circular cylinder constructed from a layer of air with a height of 3 mfp and of soil with a depth depending on the photon energy: 2 mfp of photons in soil for source depth 0.0 mfp and 0.2 mfp; 3 mfp for source depth of 1.0 mfp; 3.5 mfp for source depth of 2.5 mfp; 5 mfp for source depth of 4.0 mfp. The additional thickness of at least 1 mfp below the source depth was considered sufficient to account for backscatter events in the deeper layers. The radius of the cylinder corresponds to about five times the mean free path of the relevant photons in air. A previous study (Satoh et al., 2014) has shown that this size of simulation geometry is sufficient to properly treat photon transport in the contaminated environment.

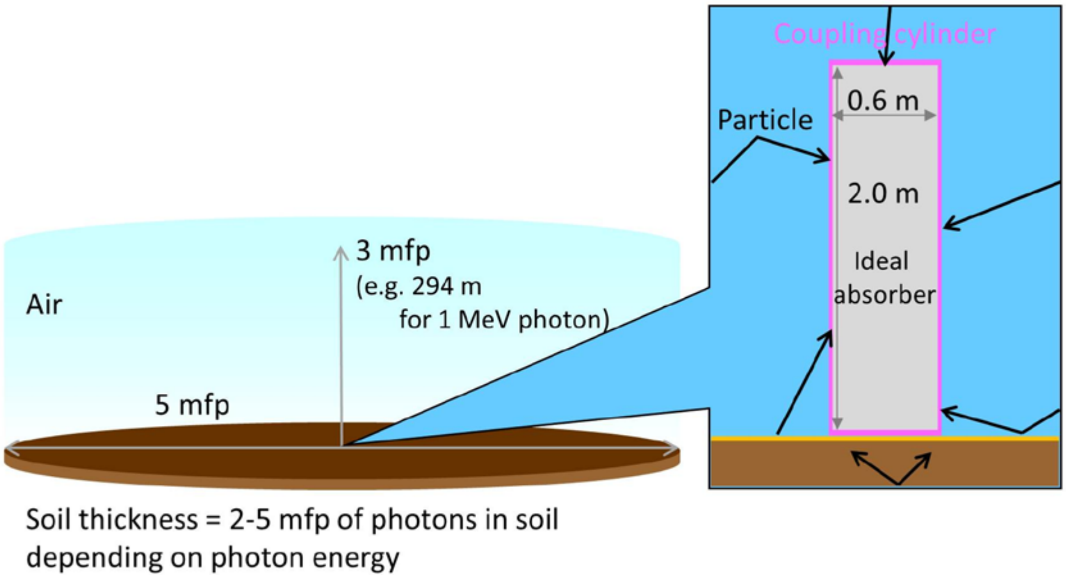

Fig. 5.2. Schematic representation of the geometry simulating the environmental field due to soil contamination, mfp: mean free path.

(63) Table 5.1 lists the density and elemental composition of air and soil adopted in the computations of this report. The values were obtained from the data for soil (Type 1) provided by the International Commission on Radiation Units & Measurements (ICRU) (ICRU, 1994) and dry air from the National Institute of Standards and Technology (NIST) (Berger et al., 2005), respectively. The densities of soil and air were considered to be 1 g cm^{-3} and $1.2x10^{-3}$ g cm^{-3}, respectively. In real environmental exposure situations, the soil densities are mostly higher than 1×10^{3} kg m^{-3} and could vary according to both location and depth; however, this variation does not affect the relation of source intensity to the radiation field in air, if source depth is expressed in terms of g cm^{-2}. Furthermore, it has been shown that changes in soil composition do not significantly alter the transported photon fields at the phantom coupling surface (Saito and Jacob, 1995).

Table 5.1. Density and elemental composition of air (Berger et al., 2005) and soil (ICRU, 1994).

	Density	Elemental composition (wt%)							
Material	g cm^{-3}	H	C	N	O	Al	Si	Ar	Fe
Air	$1.2x10^{-3}$	-	$1.24x10^{-2}$	75.53	23.18	-	-	1.28	-
Soil	1.0	2.20	-	-	57.50	8.50	26.20	-	5.60

(64) The radiation field was derived for 25 initial photon energies, ranging from 0.01 to 8 MeV, so as to cover the wide energy spectra of natural occurring and artificially produced radionuclides. The soil was assumed as a planar air-ground interface and scatter and absorption of the radiation fields in both air and ground were considered in the calculations.

(65) Electron planar sources were also considered for the surface of the soil; for other depths, primary electron sources were not transported since they will not travel sufficiently far to reach the surface. Initial electron energies from 0.01 to 8 MeV were considered. For

electron sources, both electrons and secondary photons were transported. It should be noted that bremsstrahlung x-rays were considered in both the soil and air exposure scenarios.

(66) From the transport calculations in the environment, individual particles were recorded at the surface of a virtual cylinder termed the ‘coupling cylinder’. This cylinder is positioned on the ground concentric with the simulation geometry, as depicted in Fig. 5.2 (right). The diameter of the cylinder is 0.6 m, and its height is 2 m. The phase-space coordinates are recorded for particles that cross the surface of the cylinder and consists of the spatial coordinates (x, y, x), momentum (p_x, p_y, p_z), kinetic energy, and Monte Carlo weight. In order to avoid counting a particle as it exits the cylinder, the space inside the coupling cylinder is treated as an ideal absorber such that the Monte Carlo code terminates the transport of the particle when it enters this region. The data were recorded to an external file in ASCII format to be used for the Step 2 calculations - organ equivalent dose calculations within the phantoms. The small fraction of those photons that could be scattered back into the cylinder from the ground or air, is followed in Step 2 calculations (i.e., particles starting from the surface of coupling cylinder). More details on the method can be found in Satoh et al. (2015).

(67) To reduce the variance of the Monte Carlo simulations, the uniform source was reproduced by increasing the number of radioactive decays per unit area and decreasing the Monte Carlo weight of particles released by radioactive decay as its emission point approaches the coupling cylinder (Satoh et al., 2015).

(68) Fig. 5.3 shows an example of the energy and angular distribution of environmental photons from a source of 0.5 MeV at a depth of 0.2 mfp, at heights 0 - 0.40 m and 1.60 - 2.00 m, as this is recorded on the surface of the coupling cylinder. The incident directions of photons are expressed as the sine of a vector parallel to the ground surface and the angles are expressed as elevation angles. It can be seen, that, quite a large portion of the photons comes from the direction of 30° upwards and the majority of photons are between 0 and 30° with respect to the horizontal plane. Consequently, they exhibit a rather pronounced horizontal bias.

(69) Uncollided photons are recorded in the highest energy bin. Overall, about 20% of the recorded photons on the coupling cylinder never interact with the air. It should be noted that the shape of the energy and angular spectra are rather independent of height.

(70) The directional distributions of scattered and uncollided photons for a source of 0.1 MeV at 1 and 4 mfp depths in the ground, respectively, are shown in Fig. 5.4. The scattered photons show a small local maximum at shallow directions downwards, which is more pronounced for 1 mfp than for 4 mfp. This is in agreement with the angular dependence of air kerma for sources at 1 and 4 mfp, respectively, as reported by Eckerman and Ryman (1993). The relative number of uncollided photons is considerably decreased from about 22% at 1 mfp to about 7% at 4 mfp.

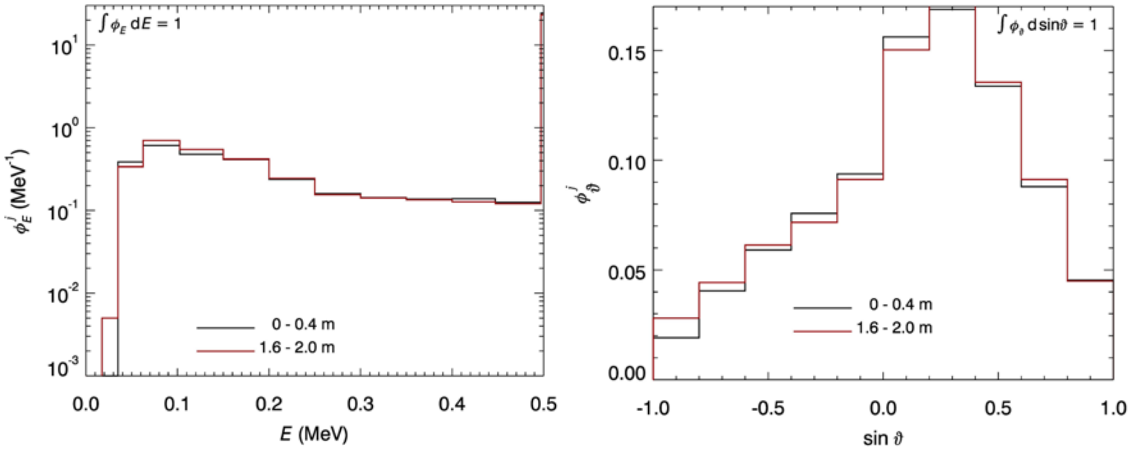

Fig. 5.3. Energy (left) and angular (right) distribution of an isotropic infinite source in the soil at a depth of 0.2 mfp, emitting 0.5 MeV monoenergetic photons. (left) The y axis shows the number of photons per energy bin (right). The y axis shows the number of photons per sine angle at the indicated height range. To differentiate these distributions from the respective distribution for all heights (*Φ*), they are marked by the superscript *j*.

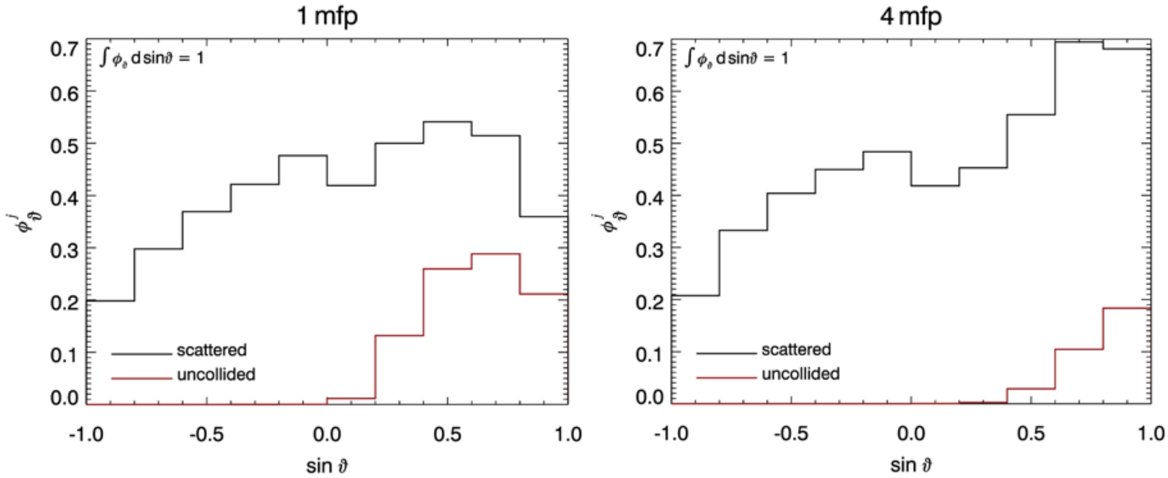

Fig. 5.4. Angular distribution of scattered and uncollided photons for an isotropic infinite source in the soil at a depth of 1 mfp (left) and 4 mfp (right) emitting 0.1 MeV monoenergetic photons. The y axis shows the number of photons per sine angle. To differentiate these distributions from the respective total distribution (*Φ*), they are marked by the superscript *j*.

5.2. Submersion to contaminated air

(71) In the air submersion exposure scenario, the contaminated air represents the gaseous radioactive release into the atmosphere at locations which are not too near to the release point, and are assumed to be homogeneous in air activity concentration above a smooth air-ground interface. Near the release point, radionuclides in air distribute according to the Gaussian plume model, and positional relations between the Gaussian plume and the human body significantly affect the features of the radiation fields at the location where doses are evaluated (Saito et al., 1998). For example, photons enter a human body mostly from above, if the human body is positioned below the plume; while, incident angles of photons are biased in horizontal directions, if the human body is at a far distance from the plume. Evaluating dose

rate coefficients considering these complex situations is not practical, and thus the submersion model of this report is a reasonable approximation of exposures for most cases. Fig. 5.5 shows schematically the air submersion geometry. The geometry is considered to be semi-infinite in extent. The ground interface is assumed to be an uncontaminated flat surface of infinite area. The elemental composition of air is shown in Table 5.1 and corresponds to dry air at a density of 1.2 x 10^{-3} g cm^{-3}. Bellamy et al. (2018) have estimated air kerma as a function of air density and shows an example of these results for 1 MeV photons. The authors found that the functional relation between air kerma and air density is virtually independent of photon energy. Using these values, the dose rate coefficients for air submersion can be scaled to account for different air densities. With increasing humidity, the air density increases and consequently the air kerma decreases (see Fig. 5.6). Thus, the dose rate coefficient per air kerma increases with increasing humidity.

(72) The number of histories, reduction variance techniques, and scoring of the particles were similar to those mentioned above for soil contamination.

(73) The particles originated from the air region are transported and scored on the surface of the coupling cylinder, placed on the air ground interface. The coupling surface records the position, angle, energy of incident photons, and Monte Carlo weight as discussed in Section 5.1 regarding soil contamination. This method produces energy-dependent fluences. As for the soil contamination exposure scenario, calculations were performed for 25 monoenergetic sources of photons and electrons ranging from 0.01 to 8 MeV.

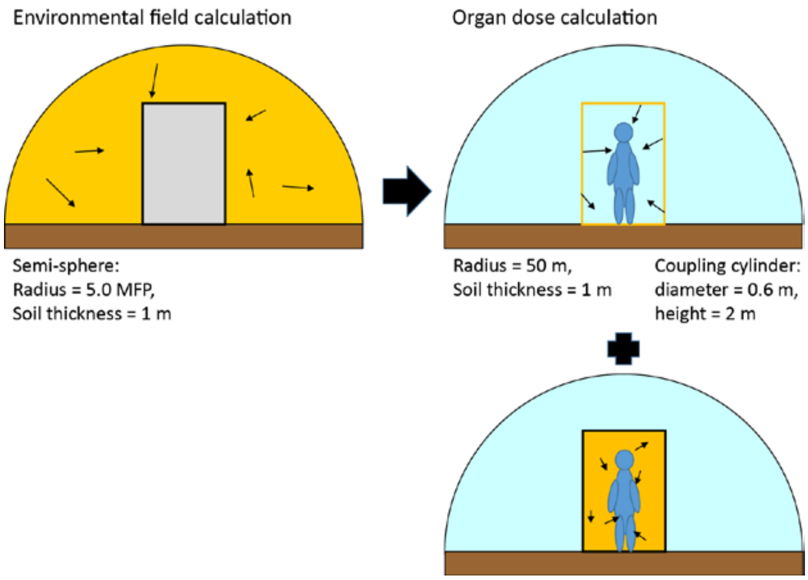

Fig. 5.5. Schematic view of the geometry simulating submersion into contaminated air. The region coloured with yellow indicates the source region. For organ equivalent dose calculations, the medium inside the coupling cylinder is air. For electron exposures, the particles start not only from the surface of the cylinder but also from the inside of the cylinder (for photons this is not necessary since the mean free path of photons in air is long and the source inside the cylinder does not significantly contribute to the results of organ equivalent dose calculations).

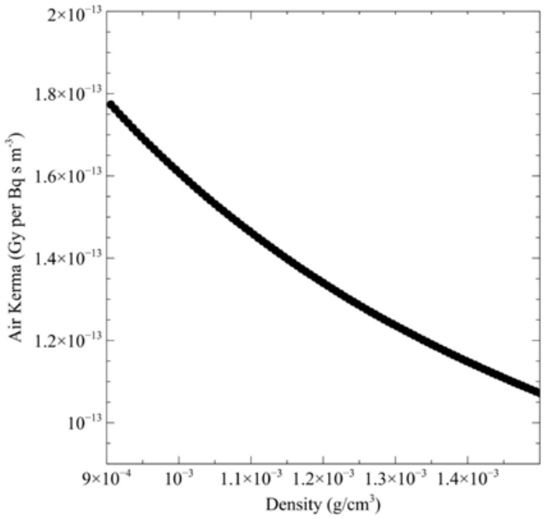

Fig. 5.6 Air kerma as a function of air density for 1 MeV photons from Bellamy et al. (2018).

(74) Fig. 5.7 shows the energy spectrum of environmental photons from a source of 0.5 MeV at heights 0 - 0.40 m and 1.60 - 2.00 m. The incident directions of photons are expressed as the sine of the vector parallel to the ground surface. It can be seen that for many photons, no scattering is observed and most photons come from upper directions with little dependence of their directional distribution on height.

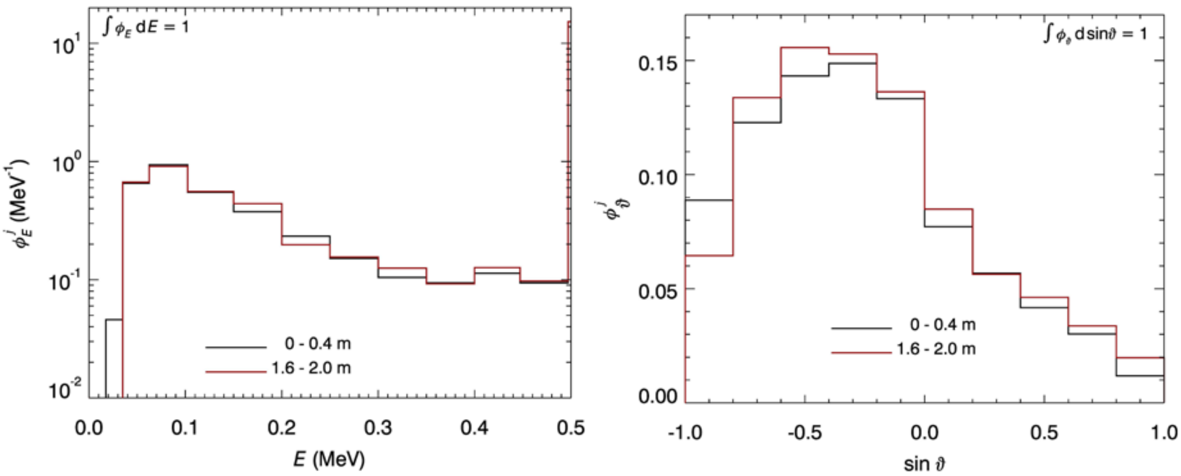

Fig. 5.7. Energy (left) and angular (right) distribution of a semi-infinite source in the air emitting 0.5 MeV monoenergetic photons. (left) The y axis shows the number of photons per energy bin. (right) The y axis shows the number of photons per sine angle at the indicated height range. To differentiate these distributions from the respective spectrum for all heights (Φ), they are marked by the superscript j.

5.3. Water immersion

(75) Water immersion might be rare in the pathway of environmental exposure. Nevertheless, many facilities have routine liquid effluent releases, and radioactive releases to

the sea or contamination of surface waters have been observed after major radiological accidents. Highly contaminated water from a damaged reactor core and water pools resulting from damaged nuclear fuels can be released through direct or ground water discharge, as they occurred as a consequence of the accident at the nuclear power plant in Fukushima Prefecture, Japan, in 2011 (Buesseler et al., 2017). Radionuclides such as radioactive iodine and caesium were detected in tap water and the exposure due to contaminated water used for bathing had to be estimated. Moreover, radionuclides were also released into the sea and could be potentially harmful for people who enter the sea around the power plant following the accident.

(76) Fig. 5.8 shows schematically the water immersion geometry. The source geometry is assumed to be infinite in extent. The water density is 1.0×10^3 kg m^{-3} and the composition by mass fraction is 0.112 for H and 0.888 for O, representing pure liquid water. The phantoms are assumed to be completely immersed in the water and are placed at the centre of a sphere with a radius of 2 m, corresponding to 5 mfp at a photon energy of 8 MeV in water. Monoenergetic sources photons and electrons are generated uniformly in the contaminated water. As for the other geometries, bremsstrahlung photons are directly transported by the PHITS Monte Carlo transport code. The organ equivalent dose rate coefficients for water immersion of the male and female phantoms at the six reference ages have been calculated in a single-step and thus no coupling cylinder was required.

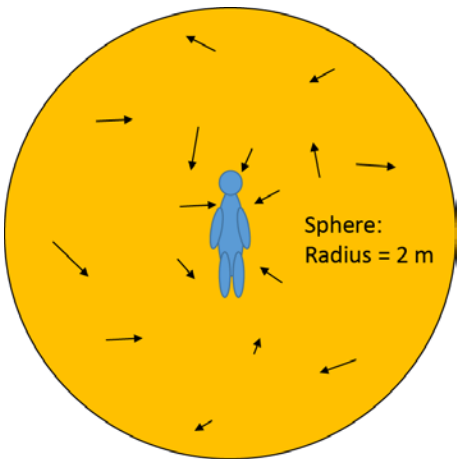

Fig. 5.8. Schematic view of water immersion. The sphere is centred on the midpoint of the three axes of the phantom.

5.4. Calculation of air kerma and ambient dose equivalent in the environmental field

(77) Air kerma and ambient dose equivalent has been widely used for the purpose of radiation protection after environmental exposures (ICRU, 1994; IAEA, 2000b). The air kerma is a basic quantity related to photon energy fluence, and in natural environments it is substantially equivalent to the air absorbed dose which has been used by UNSCEAR to express dose rates in air (UNSCEAR, 2000, 2008). Absorbed dose in air has been used in environmental monitoring for many years, but it has been gradually replaced by the operational quantity ambient dose equivalent as seen in worldwide environmental monitoring data (European Commission Joint Research Centre, 2017). The ambient dose equivalent, defined as the dose equivalent for aligned and expanded radiation fields at a depth of 10 mm

in the International Commission on Radiation Units and Measurements (ICRU) sphere consisting of ICRU 4-element tissue, is aimed to conservatively evaluate effective doses for diverse exposures (ICRU, 1993). Though originally the operational quantity ambient dose equivalent was introduced for radiation protection of workers (workplace monitoring), this dosimetric quantity has also been applied to environmental monitoring: the instruments for monitoring of $H^*(10)$ generally have an isotropic response with respect to both energy and angular distributions of incident photons. Resultantly, these instruments work well in environmental fields which exhibit complex angular and energy distributions, even if they are calibrated under simple conditions such as for unidirectional irradiation using monoenergetic sources. Consequently, environmental monitoring data worldwide are generally expressed as dose rates in air reported as the operational quantity ambient dose equivalent (European Commission Joint Research Centre, 2017).

(78) In order to relate the air contamination and ground deposition densities of a radionuclide to dose rates in air, coefficients are required for both air kerma and ambient dose equivalent rates. Many authors have published coefficients relating radionuclide concentration in the environment to air kerma rate (Dillman, 1974; O' Brien and Sanna, 1976; ICRU, 1994; Saito and Jacob, 1995), and to ambient equivalent rate (Lemercier et al., 2008; Saito and Petoussi-Henss, 2014), and these data have been used in environmental dose evaluations. In the present report, these coefficients have been recalculated considering air kerma and ambient dose equivalent rates at 1 m height above ground for both the soil contamination and air submersion exposure geometries described above from monoenergetic photon sources. For the simulations, the Monte Carlo code PHITS (see section 5) was used and the same environmental conditions were considered as those applied in the calculation of the environmental fields – see sections 5.1 and 5.2.

(79) The calculation was made by simulating a 30 cm diameter sphere filled with and surrounded by air, at 1 m above the ground and by scoring the particles entering the sphere. The 30 cm sphere represents the size of a human torso and this size was considered appropriate. The transport simulation was restarted from the surface of the coupling cylinder using the data in the external file created in the Step 1 of the calculations. Fig. 5.9 shows a schematic representation of the calculation geometry. The photon fluence scored at the air sphere is then converted to an air kerma rate and ambient dose equivalent rate using the dose coefficients given in *Publication 74* (ICRP, 1996b). The relative uncertainties of these quantities were less than 1%.

(80) For soil and air contamination, the air kerma depends on the distance from the ground; while this dependence is weak for sources in air, it is pronounced for planar sources in the ground.

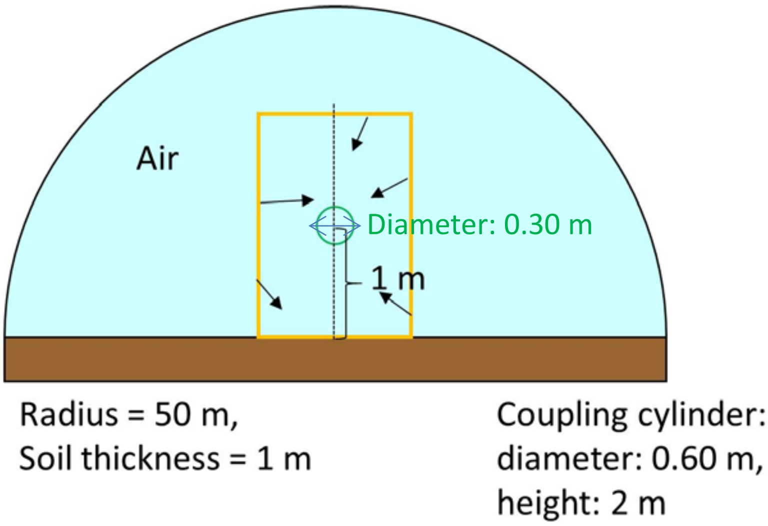

Fig. 5.9. Schematic representation of calculation of air kerma and ambient dose equivalent.

(81) On the basis of these results, ambient dose equivalent rate coefficients, $\dot{h}^*(10)$), in units of nSv h^{-1} Bq^{-1} m^2 or nSv h^{-1} Bq^{-1} m^3 can be derived to relate the activity concentration to the ambient dose equivalent rate. Thus, the ambient dose equivalent rate can be subsequently related to the effective dose rate.

(82) Individual monitoring of the effective dose is performed with dosimeters calibrated in terms of personal dose equivalent, $H_p(d)$. The Task Group which developed this publication decided not to include dose coefficients for $H_p(d)$. $H_p(d)$ is defined as the dose equivalent in soft tissue, at an appropriate depth, d, below a specified point on the body. The specified point is usually given by the position where the individual's dosimeter is worn. Calibration of personal dosimeters is performed by exposure to unidirectional radiation at an incident angle (α), where α is the angle between the direction of incidence of radiation and the reference direction of the personal dosimeter mounted on the front face of the calibration phantom. These calibrations are typically performed for normally incidence radiations i.e. α=0.0. On the other hand, for the environmental fields considered in this publication, photons of wide energy distribution are incident from various angles. Standardising reference radiation fields and calibration procedures simulating the environmental radiation have not been recommended by international organisations, such as the International Organization for Standardization (ISO) and the International Electrotechnical Commission (IEC). The coefficients for $H_p(10)$ could be calculated using phantoms and environmental radiation sources by Monte Carlo simulations. However, methods of calibration of personal dosimeters to link dosimeter readings to the dose rate coefficients of H_p(d) have not yet been established for environmental exposures.

(83) Individual monitoring in environmental radiation fields has often been performed in Japan after 2011, with dosimeters calibrated by irradiation of unidirectional radiation (Nuclear Regulation Authority Japan website, 2013). It is of significant concern whether the personal dosimeters calibrated in this way provide reasonable values for assessment of effective dose in the environmental fields. To address the question, Satoh et al. (2017) analysed the relation of *E*, *H*(10)*, and $H_p(10)$ in radiation fields originating from photon emissions from both ^{134}Cs and ^{137}Cs distributed in different depths in soil, where the personal dosimeters were calibrated under the above simplified exposure conditions. A conclusion of their analysis is

that, both area monitoring and individual monitoring do provide reasonable estimates of effective dose, for the conditions investigated.

6. DETERMINATION OF DOSE RATE COEFFICIENTS FOR MONOENERGETIC PARTICLES (STEP 2)

6.1. Monte Carlo photon and electron transport calculation in the anthropomorphic phantoms

(84) For the above discussed exposure geometries of contaminated soil and air, Step 2 calculations involved the computation of organ equivalent dose rate coefficients in each gender-age-specific phantom resulting from the simulated radiation fields from Step 1 calculations. The recorded particle histories on the coupling cylinder were used as the source irradiating the phantom and each phantom was placed inside the air-filled coupling cylinder.

(85) Particle transport calculations starting from the surface of the coupling cylinder were performed with PHITS, version 2.66 (Sato et al., 2013). The atomic data libraries MCPLIB04 (White, 2003) and EL03 (Adams, 2000) were utilised for photon and electron transport, respectively.

(86) Step 2 considers photon as well as electron fields as these were recorded on the coupling cylinder. For photon fields, also secondary electrons were transported. The combined relative uncertainty (i.e. one standard deviation) from both Steps 1 and 2 computations was less than 10% for most organs and tissues, where the dominating contribution stems from the environmental field calculations.

(87) The computational methods for determining the equivalent dose rate to active marrow and skeletal endosteum are described in Annex A.

(88) For evaluating the absorbed doses to the sensitive layer of the skin, which is considered to be 50-100 μm below the skin surface, polygon mesh formats of the reference phantoms were applied, together with the Monte Carlo code GEANT4 (Agostinelli et al., 2003). Further details on estimates of skin dose are given in Annex B.

(89) The organ equivalent doses were evaluated in the form of dose rate coefficients giving the mean organ equivalent dose rate normalised to a measurable environmental radioactivity quantity. The doses are then estimated on the basis of the measured ground deposition levels (i.e. surface activity densities) or photon dose rate in the air, normalised to a unit deposit of each radionuclide. As gamma ray measurements in the environment are performed at a height of 1 m above the ground surface, the normalisation quantity for measurements in air was selected to be air kerma and ambient dose equivalent at height 1 m above the ground at the position of the body's longitudinal axis. Values of air kerma at 1 m height above the ground normalized to source activity are also given (see section 6.2). These coefficients are used to facilitate normalisation to source activity (i.e. photon emission per unit area or per unit volume).

(90) Organ equivalent dose rate coefficients for all defined organs/tissues, including all those explicitly noted in the definition of the effective dose, are given as equivalent dose rates per radioactivity concentration. Since this document refers to environmental exposures of photons and electrons, both of which have radiation weighting factor (w_R) equals to unity, the equivalent dose coefficients are numerically equivalent to their corresponding absorbed dose coefficients.

(91) In order to avoid fluctuation by statistical uncertainty and obtain smooth curves of the organ equivalent dose rate coefficients as a function of photon and electron energy, data fitting was applied using the piecewise cubic Hermite function (Fritsch and Carlson, 1980).

(92) It should be noted that, for monoenergetic photon and electron sources below 0.05 and 0.10 MeV, respectively, the organ equivalent dose rate coefficients were set to zero, if their contribution to effective dose was below 1% and the value of the precedent energy was zero. This was done to avoid discontinuities on the curves or to improve their smoothness.

(93) Reference values of the equivalent dose rate coefficients of organs and tissues for which tissue weighting factors are defined (ICRP, 2007), as well as for the remainder tissues, can be found in the electronic supplement to this report. The data are given separately for the male and female adult and paediatric reference phantoms. These, since they have been calculated with the ICRP reference phantoms, for reference geometries and following ICRP methodology, are considered to be the ICRP reference data.

(94) The results of these calculations are used to derive radionuclide-specific dose rate coefficients through energy interpolation to obtain coefficients for the detailed photon and electron decay spectrum of each radionuclide as given in *Publication 107* - see section 7.

6.2. Dose rate coefficients for soil contamination

(95) The absorbed dose delivered to internal organs and tissues is calculated by exposing the computational phantoms to the radiation fields obtained previously. The particle transport is re-started based on information on the particles histories written in the external file during the Step 1. The calculation efficiency is significantly improved by using the environmental radiation field obtained in the Step 1 which is in common to the Step 2 calculations for each reference phantom age and gender.

(96) The right side of the Fig. 6.1 illustrates the geometry of the Step 2 calculation. The phantom is placed inside the coupling cylinder, and the remaining space is filled with air. Owing to the fact that the simulation geometry is cylindrically symmetric, the transport calculation is repeated 36 times by rotating the source position in 10° steps at the surface of the cylinder around the central axis to avoid any directional bias.

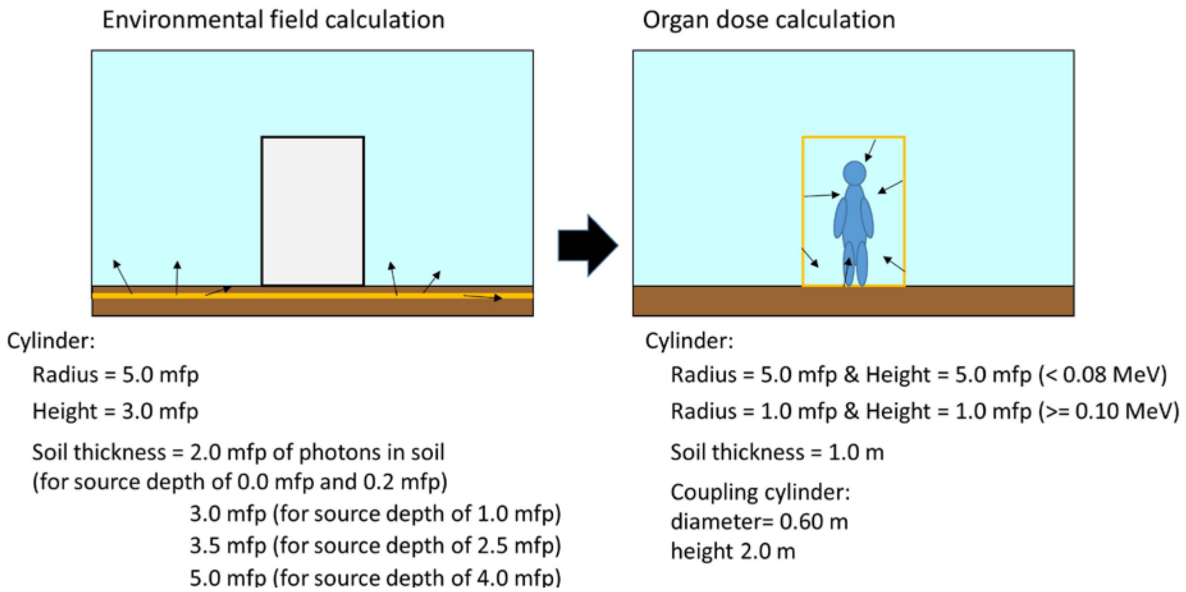

Fig. 6.1. Schematic representation of the geometry simulating the soil contamination. Left describes the Step 1 of the calculation and the right side of the Figure, the Step 2. "mfp" indicates mean free path.

(97) Dose rate coefficients for soil contamination were evaluated as the effective dose rate per activity concentration for monoenergetic sources of photons and electrons in soil, whose energy ranges from 0.01 to 8 MeV along 25 energy points. The coefficients are given in the unit of nSv h^{-1} Bq^{-1} m^2. The effective dose rates were computed from the data of organ equivalent dose rates computed using the ICRP adult and paediatric (newborn, 1-, 5-, 10- and 15-year-old) reference computational phantoms as described in Section 4.2. The data for photons were evaluated for the sources uniformly distributed in the soil over a planar area and at specific depths of 0.0, 0.2, 1.0, 2.5 and 4.0 mfp for the photons emitted in the soil. Electrons were evaluated only for the sources located on the air-ground interface (i.e. no accounting for electrons emitted at depth within the soil).

(98) For each source depth, 10 – 20 million photon histories were started, depending on the photon energy, from the recorded distributions on the coupling cylinder. This led to coefficients of variance that were generally around 0.5% for large organs and around 1% for small organs. For electron irradiations, 20 million – 2 billion particle histories were followed. This led to coefficients of variance that were generally around 5% for all organs. Note that these coefficients of variance refer only to Step 2 organ equivalent dose calculations and not to the environmental field calculations.

(99) For photon sources, coefficients for air kerma and ambient dose equivalent rates were also evaluated in air at a height of 1m above the ground as described in Section 5.4.

(100) The effective dose rate coefficients are given in Tables 6.1 to 6.5 for photon sources at specific depths of 0.0, 0.2, 1.0, 2.5 and 4.0 mfp for photons emitted within the soil together with the data on the corresponding air kerma rates and ambient dose equivalent rates. The effective dose rate coefficient for electron sources on the ground surface are given in Table 6.6. Effective dose rate coefficients are shown graphically in Fig. 6.2 to Fig. 6.7. The equivalent dose rate coefficients for all organs contributing to the effective dose as well as of the remainder tissues are tabulated in regard to both age and gender, and are compiled in an electronic supplement to this publication.

(101) These figures demonstrate the age-dependence of the effective dose rate for environmental photon and electron exposures. For most energies and all geometries, the smaller the phantom, the larger the effective dose rate coefficient. Larger differences are observed for the adult phantom and the newborn which could amount to 140% for energies lower than 50 keV and contamination on the surface of the ground. Also, it can be seen that the ambient dose equivalent rate, $\dot{h}^*(10)$, for most cases, is a conservative approximation of the effective dose. Exceptions are observed for the newborn phantoms, the 1-year-old and 5-year-old phantoms at energy of 0.01 MeV, where the effective dose rate coefficient is higher than the ambient dose equivalent rate, $\dot{h}^*(10)$. This could be explained by considering that, for decreasing photon energies, the mean free path of photons in air is also decreasing. $\dot{h}^*(10)$ is estimated in air at 1 m height from the ground surface, whereas the phantoms are standing on the ground surface. Furthermore, it can be noted that**,** $\dot{h}^*(10)$, becomes more and more conservative as the source depth increases. This could be explained by the photon energy spectrum which is shifted to lower energies.

Table 6.1. Effective dose rate, ambient dose equivalent rate and air kerma rate coefficients for monoenergetic photon sources distributed at a depth of 0.0 mean free paths in the soil. Ambient dose equivalent rate and air kerma rate coefficients were calculated at 1 m above ground.

Energy	Effective dose rate coefficient						$\dot{h}^*(10)$	$\dot{k}_a$
(MeV)	($nSv\ h^{-1}\ Bq^{-1}\ m^2$)							($nGy\ h^{-1}\ Bq^{-1}\ m^2$)
	Adult	15 yr	10 yr	5 yr	1 yr	Newborn		
0.010	5.33E-06	5.15E-06	7.04E-06	8.97E-06	1.70E-05	3.25E-05	5.24E-06	6.36E-04
0.015	1.41E-05	1.58E-05	2.50E-05	3.12E-05	4.65E-05	9.23E-05	2.06E-04	7.86E-04
0.020	2.89E-05	3.42E-05	4.57E-05	6.55E-05	8.39E-05	1.51E-04	4.14E-04	6.73E-04
0.030	7.23E-05	8.32E-05	1.01E-04	1.43E-04	1.80E-04	2.68E-04	4.92E-04	4.49E-04
0.040	1.12E-04	1.27E-04	1.48E-04	1.94E-04	2.39E-04	3.15E-04	4.89E-04	3.40E-04
0.050	1.43E-04	1.61E-04	1.88E-04	2.29E-04	2.80E-04	3.41E-04	4.85E-04	2.96E-04
0.060	1.77E-04	1.94E-04	2.18E-04	2.56E-04	3.07E-04	3.63E-04	5.02E-04	2.94E-04
0.070	2.08E-04	2.27E-04	2.51E-04	2.90E-04	3.41E-04	3.93E-04	5.29E-04	3.06E-04
0.080	2.39E-04	2.59E-04	2.85E-04	3.26E-04	3.80E-04	4.29E-04	5.64E-04	3.30E-04
0.100	3.02E-04	3.24E-04	3.48E-04	3.90E-04	4.52E-04	5.13E-04	6.64E-04	3.98E-04
0.150	4.65E-04	4.92E-04	5.30E-04	5.97E-04	6.81E-04	7.70E-04	9.57E-04	6.25E-04
0.200	6.28E-04	6.66E-04	7.15E-04	8.09E-04	9.16E-04	1.04E-03	1.25E-03	8.60E-04
0.300	9.67E-04	1.02E-03	1.10E-03	1.23E-03	1.39E-03	1.59E-03	1.82E-03	1.34E-03
0.400	1.31E-03	1.37E-03	1.49E-03	1.65E-03	1.87E-03	2.13E-03	2.38E-03	1.82E-03
0.500	1.66E-03	1.72E-03	1.87E-03	2.07E-03	2.34E-03	2.67E-03	2.91E-03	2.29E-03
0.600	2.01E-03	2.07E-03	2.24E-03	2.47E-03	2.78E-03	3.18E-03	3.41E-03	2.74E-03
0.800	2.63E-03	2.72E-03	2.92E-03	3.20E-03	3.58E-03	4.08E-03	4.28E-03	3.52E-03
1.000	3.12E-03	3.25E-03	3.49E-03	3.78E-03	4.20E-03	4.75E-03	4.86E-03	4.10E-03
1.500	4.57E-03	4.68E-03	5.02E-03	5.42E-03	5.93E-03	6.65E-03	6.69E-03	5.77E-03
2.000	5.87E-03	6.01E-03	6.43E-03	6.92E-03	7.50E-03	8.38E-03	8.36E-03	7.31E-03
3.000	8.18E-03	8.43E-03	8.97E-03	9.61E-03	1.03E-02	1.14E-02	1.13E-02	1.01E-02
4.000	1.02E-02	1.06E-02	1.12E-02	1.20E-02	1.27E-02	1.40E-02	1.39E-02	1.25E-02
5.000	1.21E-02	1.25E-02	1.32E-02	1.41E-02	1.48E-02	1.62E-02	1.63E-02	1.47E-02
6.000	1.38E-02	1.44E-02	1.51E-02	1.61E-02	1.68E-02	1.83E-02	1.84E-02	1.67E-02
8.000	1.76E-02	1.80E-02	1.91E-02	2.03E-02	2.09E-02	2.26E-02	2.28E-02	2.10E-02

Table 6.2. Effective dose rate, ambient dose equivalent rate and air kerma rate coefficients for monoenergetic photon sources distributed at a depth of 0.2 mean free paths in the soil. Ambient dose equivalent rate and air kerma rate coefficients were calculated at 1 m above ground.

Energy	Effective dose rate coefficient						$\dot{h}^*(10)$	$\dot{k}_a$
(MeV)	(nSv h^{-1} Bq^{-1} m^2)							(nGy h^{-1} Bq^{-1} m^2)
	Adult	15 yr	10 yr	5 yr	1 yr	Newborn		
0.010	3.02E-06	2.89E-06	4.18E-06	4.90E-06	9.31E-06	1.65E-05	3.58E-06	4.36E-04
0.015	7.40E-06	8.21E-06	1.34E-05	1.55E-05	2.23E-05	3.80E-05	1.19E-04	4.54E-04
0.020	1.44E-05	1.61E-05	2.21E-05	3.05E-05	3.16E-05	5.30E-05	2.05E-04	3.33E-04
0.030	3.06E-05	3.53E-05	4.22E-05	5.47E-05	6.06E-05	8.69E-05	2.22E-04	2.04E-04
0.040	4.73E-05	5.34E-05	6.18E-05	7.64E-05	8.44E-05	1.03E-04	2.23E-04	1.57E-04
0.050	6.42E-05	7.15E-05	8.02E-05	9.60E-05	1.07E-04	1.24E-04	2.29E-04	1.42E-04
0.060	8.17E-05	8.92E-05	9.90E-05	1.15E-04	1.26E-04	1.38E-04	2.46E-04	1.46E-04
0.070	9.98E-05	1.08E-04	1.18E-04	1.32E-04	1.45E-04	1.56E-04	2.71E-04	1.59E-04
0.080	1.17E-04	1.26E-04	1.36E-04	1.50E-04	1.64E-04	1.75E-04	3.00E-04	1.76E-04
0.100	1.50E-04	1.59E-04	1.69E-04	1.87E-04	1.98E-04	2.11E-04	3.55E-04	2.12E-04
0.150	2.33E-04	2.43E-04	2.60E-04	2.84E-04	3.03E-04	3.21E-04	5.13E-04	3.29E-04
0.200	3.03E-04	3.21E-04	3.44E-04	3.76E-04	3.98E-04	4.28E-04	6.56E-04	4.41E-04
0.300	4.38E-04	4.63E-04	4.95E-04	5.41E-04	5.70E-04	6.17E-04	9.04E-04	6.43E-04
0.400	5.66E-04	5.89E-04	6.29E-04	6.86E-04	7.20E-04	7.80E-04	1.11E-03	8.22E-04
0.500	6.88E-04	7.06E-04	7.50E-04	8.17E-04	8.55E-04	9.27E-04	1.29E-03	9.83E-04
0.600	8.01E-04	8.16E-04	8.65E-04	9.39E-04	9.82E-04	1.06E-03	1.45E-03	1.13E-03
0.800	9.97E-04	1.04E-03	1.10E-03	1.18E-03	1.24E-03	1.34E-03	1.77E-03	1.42E-03
1.000	1.15E-03	1.19E-03	1.25E-03	1.33E-03	1.40E-03	1.51E-03	1.94E-03	1.59E-03
1.500	1.58E-03	1.62E-03	1.70E-03	1.80E-03	1.89E-03	2.04E-03	2.51E-03	2.12E-03
2.000	1.95E-03	2.00E-03	2.09E-03	2.21E-03	2.31E-03	2.48E-03	3.00E-03	2.57E-03
3.000	2.56E-03	2.62E-03	2.73E-03	2.87E-03	2.99E-03	3.19E-03	3.79E-03	3.31E-03
4.000	3.05E-03	3.11E-03	3.22E-03	3.38E-03	3.50E-03	3.71E-03	4.38E-03	3.85E-03
5.000	3.45E-03	3.52E-03	3.62E-03	3.79E-03	3.89E-03	4.12E-03	4.84E-03	4.29E-03
6.000	3.82E-03	3.90E-03	3.98E-03	4.17E-03	4.25E-03	4.47E-03	5.24E-03	4.68E-03
8.000	4.67E-03	4.77E-03	4.83E-03	5.07E-03	5.09E-03	5.33E-03	6.18E-03	5.62E-03

Table 6.3. Effective dose rate, ambient dose equivalent rate and air kerma rate coefficients for monoenergetic photon sources distributed at a depth of 1.0 mean free paths in the soil. Ambient dose equivalent rate and air kerma rate coefficients were calculated at 1 m above ground.

Energy	Effective dose rate coefficient						$\dot{h}^*(10)$	$\dot{k}_a$
(MeV)	($nSv\ h^{-1}\ Bq^{-1}\ m^2$)							($nGy\ h^{-1}\ Bq^{-1}\ m^2$)
	Adult	15 yr	10 yr	5 yr	1 yr	Newborn		
0.010	7.79E-07	7.40E-07	1.07E-06	1.18E-06	2.09E-06	3.28E-06	1.05E-06	1.28E-04
0.015	1.62E-06	1.75E-06	2.83E-06	3.03E-06	4.25E-06	6.41E-06	2.78E-05	1.07E-04
0.020	2.85E-06	3.25E-06	4.37E-06	5.41E-06	6.44E-06	9.45E-06	4.54E-05	7.41E-05
0.030	6.09E-06	6.84E-06	8.20E-06	1.05E-05	1.23E-05	1.67E-05	5.03E-05	4.64E-05
0.040	1.06E-05	1.17E-05	1.33E-05	1.66E-05	1.88E-05	2.34E-05	5.56E-05	3.97E-05
0.050	1.60E-05	1.76E-05	1.94E-05	2.29E-05	2.61E-05	3.04E-05	6.33E-05	3.99E-05
0.060	2.21E-05	2.42E-05	2.68E-05	3.08E-05	3.33E-05	3.83E-05	7.53E-05	4.51E-05
0.070	2.87E-05	3.15E-05	3.46E-05	3.91E-05	4.20E-05	4.66E-05	8.92E-05	5.25E-05
0.080	3.58E-05	3.90E-05	4.26E-05	4.76E-05	5.13E-05	5.53E-05	1.04E-04	6.13E-05
0.100	5.02E-05	5.36E-05	5.78E-05	6.41E-05	6.91E-05	7.27E-05	1.34E-04	7.96E-05
0.150	8.22E-05	8.73E-05	9.25E-05	1.02E-04	1.09E-04	1.15E-04	2.01E-04	1.26E-04
0.200	1.10E-04	1.17E-04	1.24E-04	1.36E-04	1.44E-04	1.52E-04	2.60E-04	1.70E-04
0.300	1.58E-04	1.66E-04	1.77E-04	1.93E-04	2.02E-04	2.15E-04	3.56E-04	2.44E-04
0.400	1.96E-04	2.05E-04	2.19E-04	2.38E-04	2.48E-04	2.66E-04	4.27E-04	3.04E-04
0.500	2.26E-04	2.36E-04	2.52E-04	2.73E-04	2.84E-04	3.06E-04	4.79E-04	3.52E-04
0.600	2.51E-04	2.61E-04	2.78E-04	3.01E-04	3.13E-04	3.39E-04	5.16E-04	3.89E-04
0.800	2.90E-04	3.02E-04	3.19E-04	3.45E-04	3.61E-04	3.90E-04	5.71E-04	4.42E-04
1.000	3.28E-04	3.41E-04	3.60E-04	3.88E-04	4.07E-04	4.37E-04	6.22E-04	4.91E-04
1.500	4.22E-04	4.37E-04	4.59E-04	4.93E-04	5.16E-04	5.52E-04	7.48E-04	6.11E-04
2.000	5.01E-04	5.19E-04	5.43E-04	5.81E-04	6.08E-04	6.50E-04	8.52E-04	7.11E-04
3.000	6.24E-04	6.49E-04	6.75E-04	7.18E-04	7.48E-04	7.97E-04	1.01E-03	8.62E-04
4.000	7.09E-04	7.45E-04	7.70E-04	8.13E-04	8.44E-04	8.96E-04	1.11E-03	9.63E-04
5.000	7.72E-04	8.17E-04	8.42E-04	8.83E-04	9.13E-04	9.64E-04	1.18E-03	1.03E-03
6.000	8.24E-04	8.79E-04	9.03E-04	9.42E-04	9.69E-04	1.02E-03	1.23E-03	1.09E-03
8.000	9.48E-04	1.02E-03	1.05E-03	1.09E-03	1.11E-03	1.16E-03	1.37E-03	1.23E-03

Table 6.4. Effective dose rate, Ambient dose equivalent rate and air kerma rate coefficients for monoenergetic photon sources distributed at a depth of 2.5 mean free paths in the soil. Ambient dose equivalent rate and air kerma rate coefficients were calculated at 1 m above ground.

Energy	Effective dose rate coefficient						$\dot{h}^*(10)$	$\dot{k}_a$
(MeV)	($nSv\ h^{-1}\ Bq^{-1}\ m^2$)							$nGy\ h^{-1}\ Bq^{-1}\ m^2$)
	Adult	15 yr	10 yr	5 yr	1 yr	Newborn		
0.010	9.54E-08	9.07E-08	1.38E-07	1.35E-07	2.29E-07	3.81E-07	1.43E-07	1.74E-05
0.015	1.86E-07	2.02E-07	3.38E-07	3.16E-07	4.54E-07	6.91E-07	3.45E-06	1.23E-05
0.020	3.24E-07	3.83E-07	5.11E-07	5.63E-07	6.95E-07	1.00E-06	5.78E-06	9.44E-06
0.030	7.53E-07	8.47E-07	9.67E-07	1.28E-06	1.52E-06	2.05E-06	7.00E-06	6.50E-06
0.040	1.47E-06	1.60E-06	1.79E-06	2.19E-06	2.51E-06	3.21E-06	8.47E-06	6.07E-06
0.050	2.42E-06	2.71E-06	3.00E-06	3.58E-06	4.02E-06	4.88E-06	1.08E-05	6.83E-06
0.060	3.80E-06	4.15E-06	4.55E-06	5.34E-06	5.82E-06	6.72E-06	1.41E-05	8.47E-06
0.070	5.35E-06	5.79E-06	6.30E-06	7.26E-06	7.77E-06	8.75E-06	1.76E-05	1.04E-05
0.080	7.04E-06	7.58E-06	8.21E-06	9.36E-06	9.91E-06	1.10E-05	2.13E-05	1.26E-05
0.100	1.07E-05	1.14E-05	1.23E-05	1.38E-05	1.45E-05	1.58E-05	3.01E-05	1.79E-05
0.150	1.90E-05	2.03E-05	2.17E-05	2.40E-05	2.54E-05	2.67E-05	4.96E-05	3.09E-05
0.200	2.56E-05	2.73E-05	2.90E-05	3.21E-05	3.39E-05	3.57E-05	6.50E-05	4.18E-05
0.300	3.59E-05	3.81E-05	4.05E-05	4.48E-05	4.76E-05	5.03E-05	8.87E-05	5.95E-05
0.400	4.38E-05	4.63E-05	4.92E-05	5.43E-05	5.77E-05	6.13E-05	1.05E-04	7.27E-05
0.500	4.98E-05	5.24E-05	5.56E-05	6.14E-05	6.50E-05	6.93E-05	1.15E-04	8.22E-05
0.600	5.43E-05	5.70E-05	6.05E-05	6.65E-05	7.01E-05	7.51E-05	1.21E-04	8.92E-05
0.800	6.08E-05	6.35E-05	6.73E-05	7.37E-05	7.71E-05	8.31E-05	1.32E-04	9.94E-05
1.000	6.70E-05	7.01E-05	7.42E-05	8.10E-05	8.45E-05	9.13E-05	1.41E-04	1.09E-04
1.500	7.82E-05	8.16E-05	8.64E-05	9.41E-05	9.79E-05	1.06E-04	1.57E-04	1.26E-04
2.000	8.78E-05	9.11E-05	9.64E-05	1.05E-04	1.09E-04	1.18E-04	1.70E-04	1.40E-04
3.000	1.03E-04	1.07E-04	1.13E-04	1.22E-04	1.26E-04	1.37E-04	1.89E-04	1.61E-04
4.000	1.15E-04	1.18E-04	1.25E-04	1.34E-04	1.39E-04	1.49E-04	2.01E-04	1.74E-04
5.000	1.23E-04	1.27E-04	1.34E-04	1.44E-04	1.48E-04	1.58E-04	2.08E-04	1.82E-04
6.000	1.30E-04	1.35E-04	1.41E-04	1.51E-04	1.54E-04	1.64E-04	2.12E-04	1.87E-04
8.000	1.42E-04	1.49E-04	1.56E-04	1.64E-04	1.68E-04	1.76E-04	2.22E-04	1.97E-04

Table 6.5. Effective dose rate, ambient dose equivalent rate and air kerma rate coefficients for monoenergetic photon sources distributed at a depth of 4 mean free paths in the soil. Ambient dose equivalent rate and air kerma rate coefficients were calculated at 1 m above ground.

Energy	Effective dose rate coefficient						$\dot{h}^{*}(10)$	$\dot{k}_a$
(MeV)	(nSv h^{-1} Bq^{-1} m^2)							nGy h^{-1} Bq^{-1} m^2)
	Adult	15 yr	10 yr	5 yr	1 yr	Newborn		
0.010	1.48E-08	1.39E-08	2.09E-08	2.08E-08	3.29E-08	5.34E-08	2.32E-08	2.82E-06
0.015	2.79E-08	3.01E-08	4.83E-08	4.82E-08	6.61E-08	9.63E-08	5.59E-07	2.03E-06
0.020	5.02E-08	5.79E-08	7.65E-08	8.73E-08	1.03E-07	1.52E-07	9.55E-07	1.56E-06
0.030	1.20E-07	1.40E-07	1.57E-07	2.05E-07	2.40E-07	3.26E-07	1.23E-06	1.14E-06
0.040	2.44E-07	2.79E-07	3.06E-07	3.69E-07	4.42E-07	5.59E-07	1.54E-06	1.10E-06
0.050	4.42E-07	4.97E-07	5.49E-07	6.57E-07	7.48E-07	8.74E-07	2.11E-06	1.35E-06
0.060	7.69E-07	8.46E-07	9.18E-07	1.09E-06	1.19E-06	1.32E-06	3.04E-06	1.82E-06
0.070	1.15E-06	1.24E-06	1.34E-06	1.56E-06	1.67E-06	1.83E-06	3.95E-06	2.33E-06
0.080	1.55E-06	1.67E-06	1.80E-06	2.08E-06	2.20E-06	2.37E-06	4.89E-06	2.89E-06
0.100	2.45E-06	2.63E-06	2.84E-06	3.20E-06	3.40E-06	3.59E-06	7.15E-06	4.24E-06
0.150	4.81E-06	5.09E-06	5.54E-06	6.08E-06	6.47E-06	6.76E-06	1.30E-05	8.10E-06
0.200	6.65E-06	7.04E-06	7.66E-06	8.36E-06	8.90E-06	9.35E-06	1.76E-05	1.13E-05
0.300	9.13E-06	9.93E-06	1.08E-05	1.17E-05	1.24E-05	1.31E-05	2.41E-05	1.60E-05
0.400	1.09E-05	1.18E-05	1.27E-05	1.38E-05	1.46E-05	1.55E-05	2.77E-05	1.90E-05
0.500	1.22E-05	1.28E-05	1.37E-05	1.50E-05	1.58E-05	1.68E-05	2.95E-05	2.08E-05
0.600	1.30E-05	1.35E-05	1.43E-05	1.57E-05	1.65E-05	1.76E-05	3.02E-05	2.18E-05
0.800	1.39E-05	1.48E-05	1.56E-05	1.71E-05	1.79E-05	1.92E-05	3.20E-05	2.39E-05
1.000	1.47E-05	1.53E-05	1.61E-05	1.76E-05	1.84E-05	1.97E-05	3.29E-05	2.46E-05
1.500	1.65E-05	1.74E-05	1.83E-05	1.99E-05	2.08E-05	2.22E-05	3.45E-05	2.72E-05
2.000	1.81E-05	1.90E-05	2.01E-05	2.19E-05	2.27E-05	2.43E-05	3.59E-05	2.93E-05
3.000	2.04E-05	2.15E-05	2.28E-05	2.47E-05	2.55E-05	2.72E-05	3.83E-05	3.26E-05
4.000	2.20E-05	2.31E-05	2.45E-05	2.64E-05	2.72E-05	2.88E-05	4.00E-05	3.48E-05
5.000	2.32E-05	2.41E-05	2.56E-05	2.75E-05	2.82E-05	2.97E-05	4.13E-05	3.64E-05
6.000	2.41E-05	2.50E-05	2.66E-05	2.84E-05	2.89E-05	3.03E-05	4.25E-05	3.78E-05
8.000	2.66E-05	2.78E-05	2.98E-05	3.13E-05	3.18E-05	3.26E-05	4.49E-05	4.16E-05

Table 6.6. Effective dose rate coefficients for monoenergetic electron sources distributed at a depth of 0.0 mean free paths in the soil.

Energy	Effective dose rate coefficient					
(MeV)	($nSv\ h^{-1}\ Bq^{-1}\ m^2$)					
	Adult	15 yr	10 yr	5 yr	1 yr	Newborn
0.010	2.44E-10	2.25E-10	2.21E-10	2.26E-10	2.22E-10	5.49E-10
0.015	6.18E-10	6.83E-10	7.33E-10	7.30E-10	1.46E-09	1.52E-09
0.020	1.43E-09	1.60E-09	2.03E-09	2.99E-09	6.01E-09	2.73E-09
0.030	4.67E-09	5.54E-09	8.68E-09	1.59E-08	4.34E-08	1.54E-08
0.040	1.04E-08	1.69E-08	2.97E-08	5.04E-08	1.16E-07	3.91E-08
0.050	2.22E-08	4.44E-08	6.55E-08	1.00E-07	1.98E-07	5.33E-08
0.060	9.52E-08	9.13E-08	1.12E-07	1.45E-07	2.95E-07	1.18E-07
0.070	1.77E-06	5.99E-07	6.23E-07	7.86E-07	1.32E-06	1.59E-06
0.080	7.98E-06	3.47E-06	3.84E-06	4.10E-06	6.31E-06	8.62E-06
0.100	3.13E-05	2.29E-05	2.23E-05	2.20E-05	2.45E-05	3.86E-05
0.150	7.88E-05	7.63E-05	6.73E-05	6.61E-05	8.02E-05	1.42E-04
0.200	1.16E-04	1.10E-04	9.70E-05	1.11E-04	1.54E-04	2.85E-04
0.300	2.20E-04	1.93E-04	2.07E-04	2.60E-04	3.65E-04	5.84E-04
0.400	2.75E-04	2.52E-04	2.68E-04	3.29E-04	4.32E-04	6.53E-04
0.500	3.30E-04	3.09E-04	3.27E-04	3.97E-04	5.02E-04	7.44E-04
0.600	3.86E-04	3.65E-04	3.86E-04	4.64E-04	5.83E-04	9.22E-04
0.800	5.06E-04	4.75E-04	5.08E-04	6.01E-04	8.38E-04	1.74E-03
1.000	6.42E-04	5.81E-04	6.52E-04	7.68E-04	1.31E-03	3.26E-03
1.500	1.11E-03	8.95E-04	1.44E-03	1.77E-03	4.16E-03	9.94E-03
2.000	1.81E-03	1.50E-03	3.19E-03	4.04E-03	8.66E-03	1.56E-02
3.000	3.79E-03	3.35E-03	7.21E-03	8.73E-03	1.56E-02	2.58E-02
4.000	6.14E-03	6.12E-03	1.14E-02	1.33E-02	2.04E-02	3.56E-02
5.000	8.30E-03	9.21E-03	1.53E-02	1.84E-02	2.41E-02	4.54E-02
6.000	1.05E-02	1.24E-02	1.89E-02	2.38E-02	2.79E-02	5.61E-02
8.000	1.62E-02	1.84E-02	2.43E-02	3.56E-02	3.97E-02	8.33E-02

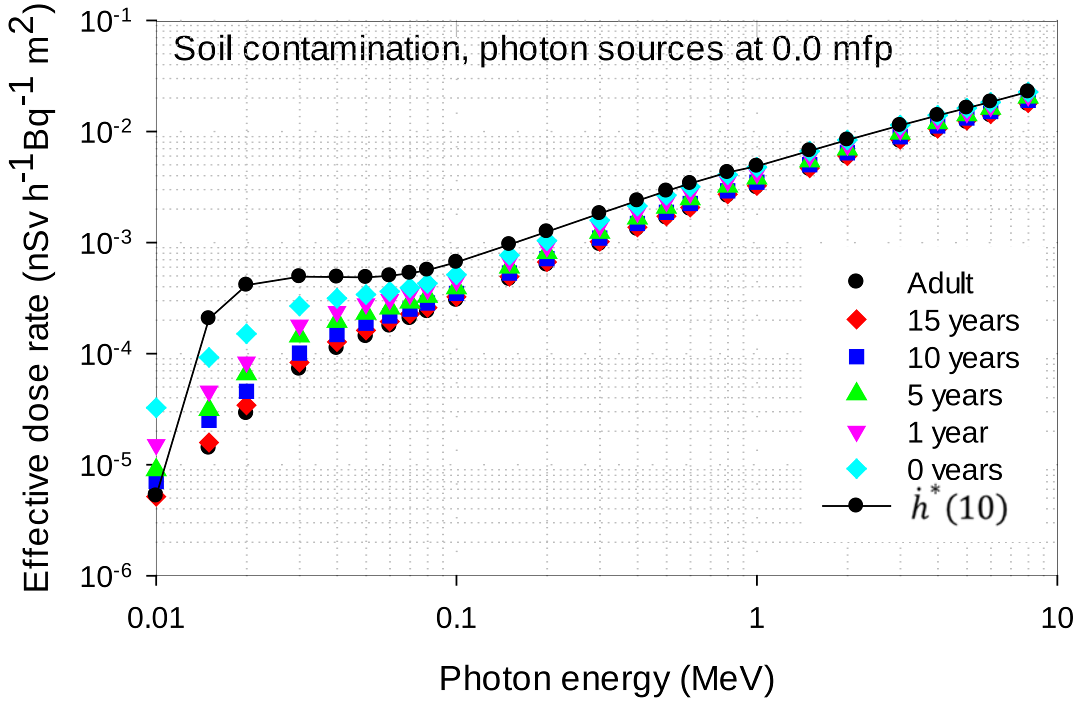

Fig. 6.2. Effective dose rate coefficients for monoenergetic photon sources distributed at the surface as a ground plane source and the corresponding ambient dose equivalent rate, $\dot{h}^*(10)$, at 1 m above the ground.

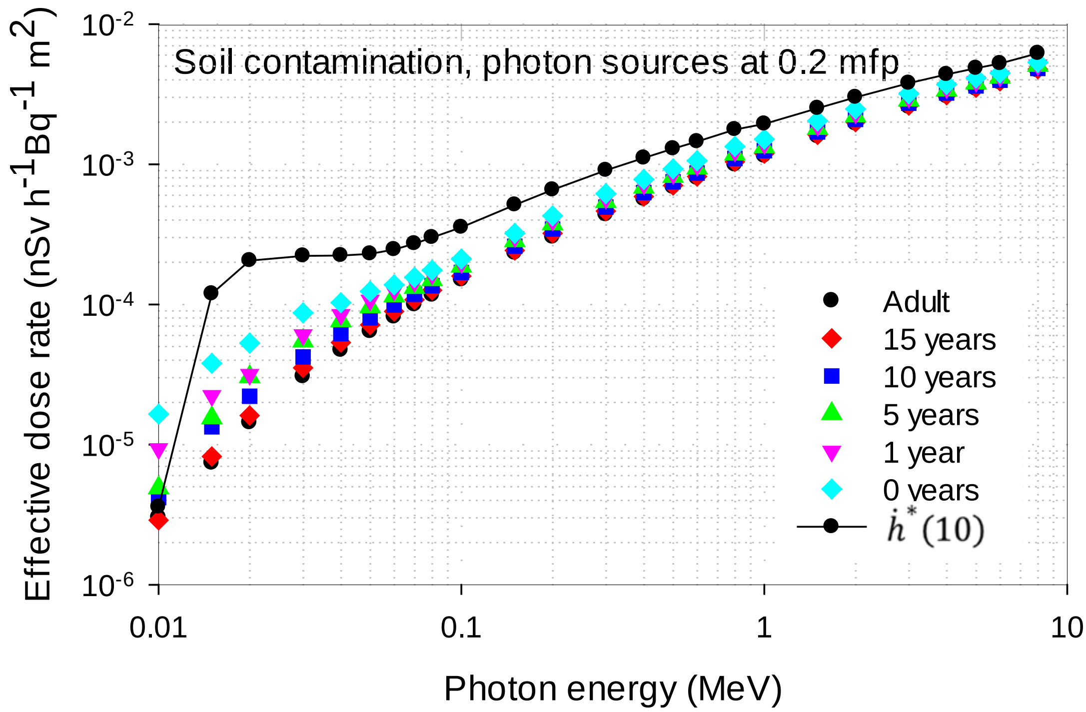

Fig. 6.3. Effective dose rate coefficients for monoenergetic photon sources distributed at a depth of 0.2 mean free paths in the soil and the corresponding ambient dose equivalent rate, $\dot{h}^*(10)$, at 1 m above ground.

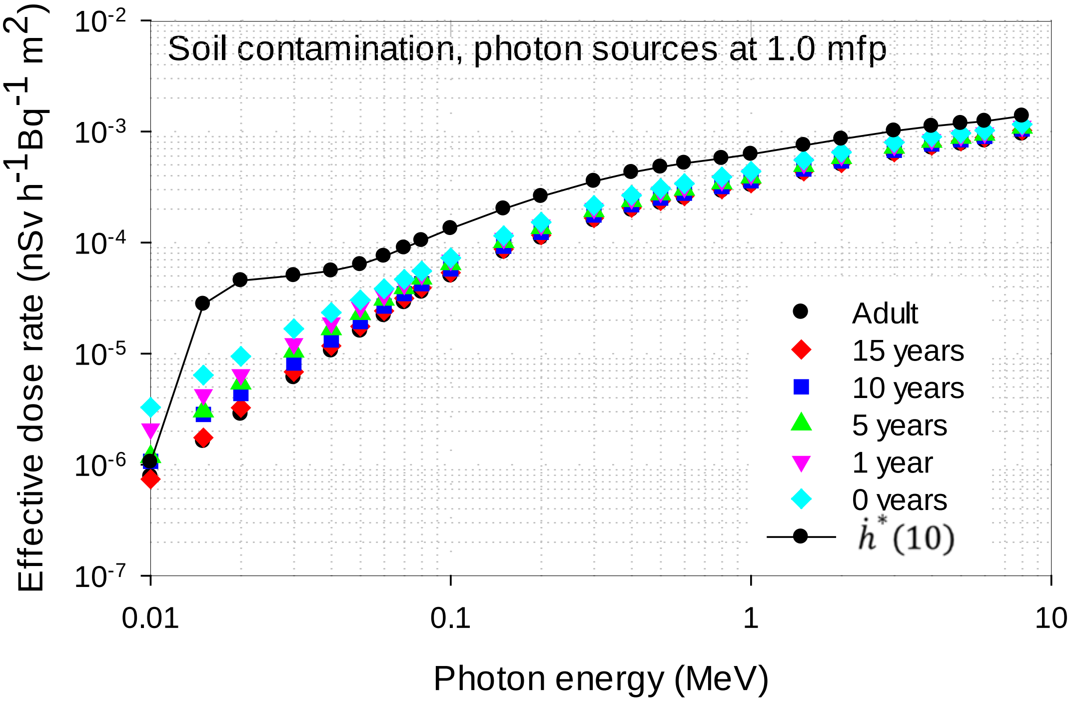

Fig. 6.4. Effective dose rate coefficients for monoenergetic photon sources distributed at a depth of 1 mean free paths in the soil and the corresponding ambient dose equivalent rate, $\dot{h}^{*}(10)$, at 1 m above ground.

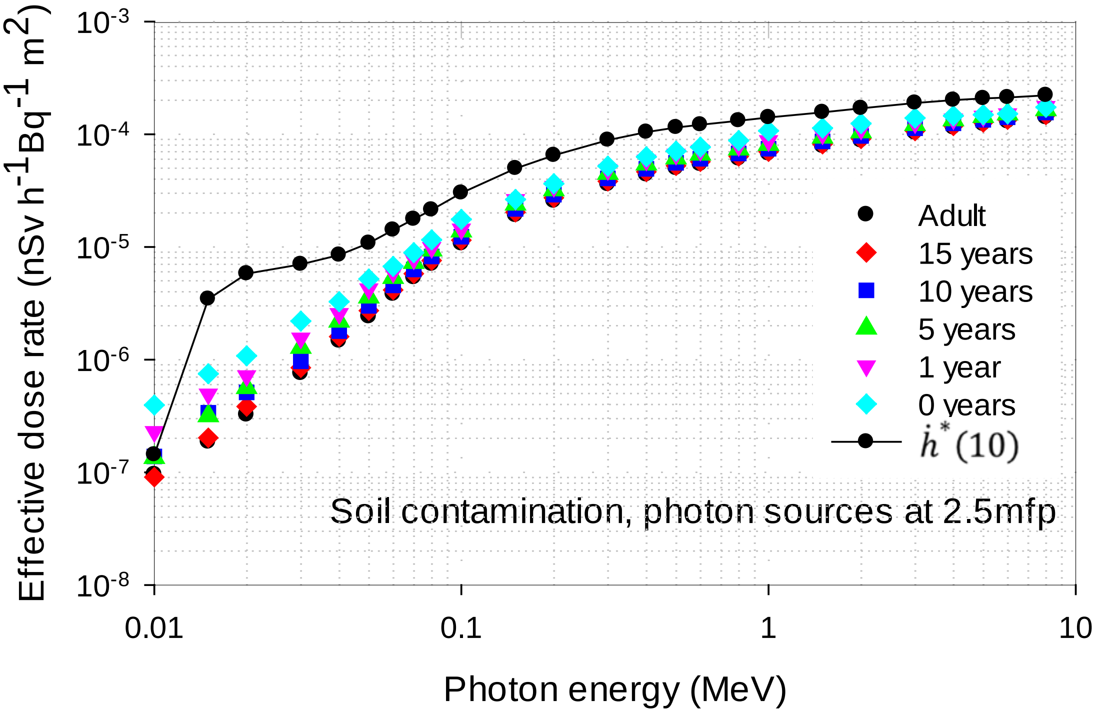

Fig. 6.5. Effective dose rate coefficients for monoenergetic photon sources distributed at a depth of 2.5 mean free paths in the soil and the corresponding ambient dose equivalent rate, $\dot{h}^{*}(10)$, at 1 m above ground.

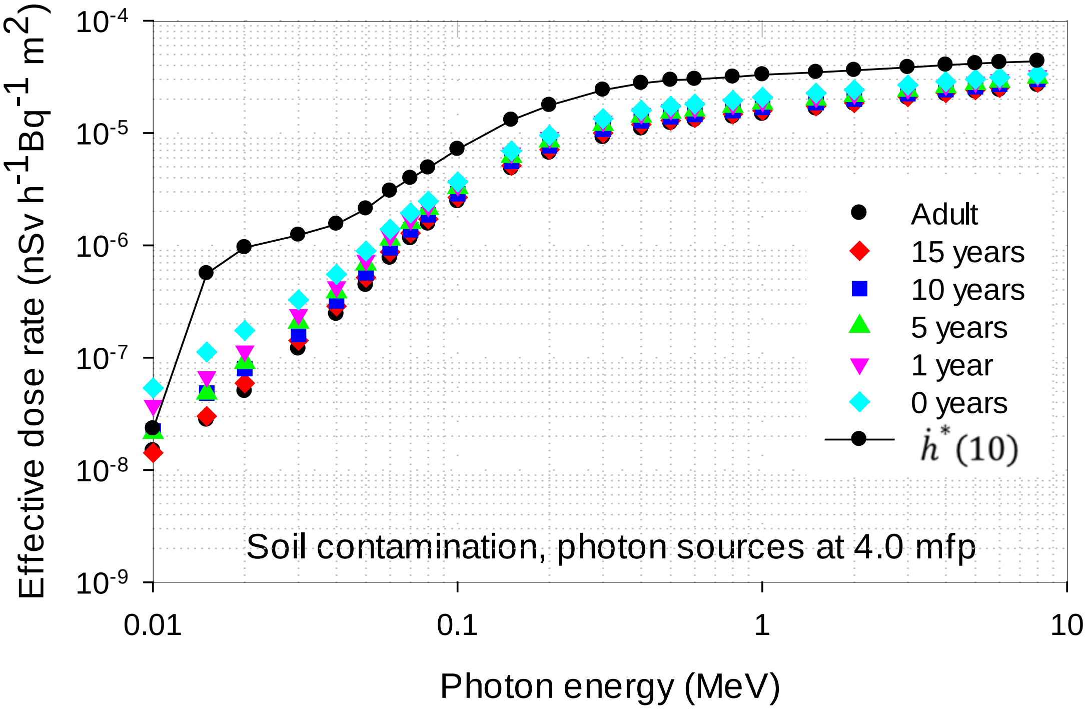

Fig. 6.6. Effective dose rate coefficients for monoenergetic photon sources distributed at a depth of 4 mean free paths in the soil and the corresponding ambient dose equivalent rate, $\dot{h}^*(10)$, at 1 m above ground.

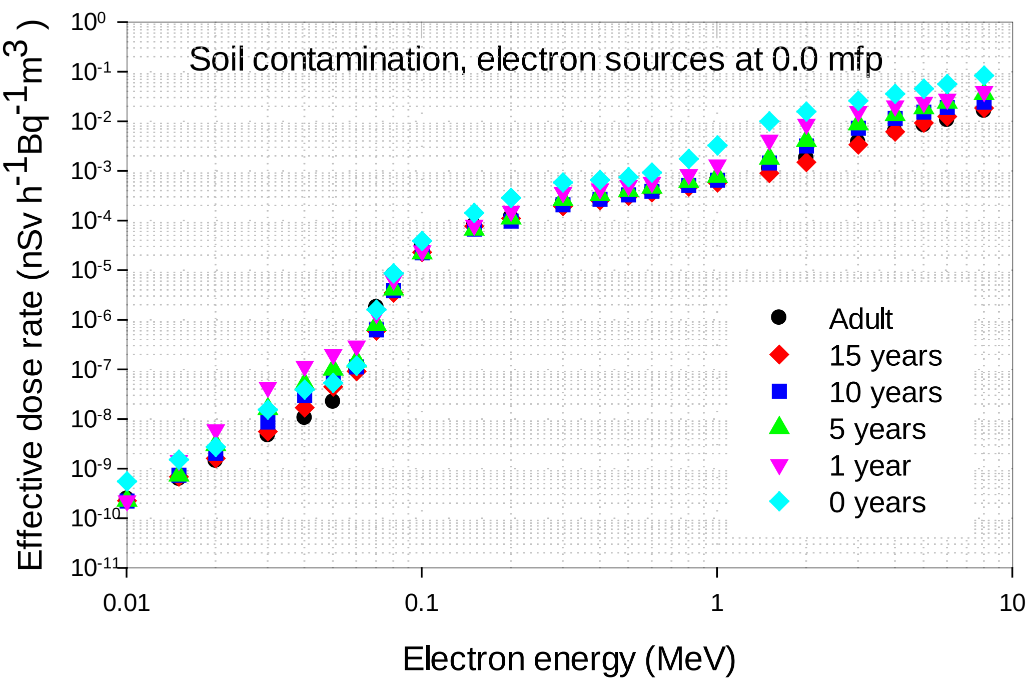

Fig. 6.7. Effective dose rate coefficients for monoenergetic electron sources distributed at the surface as a ground plane source.

(102) Fig. 6.8 shows the variation of effective dose rate coefficients for an adult as a function of mean free path (mfp) of photons in soil.

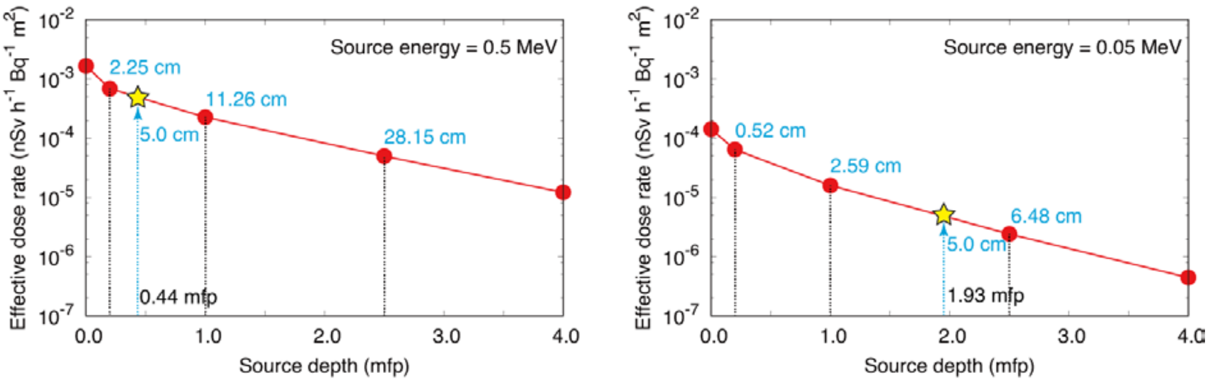

Fig. 6.8. Effective dose rate coefficients for the adult phantom as a function of mean free path in the soil, for source energy of 0.5 and 0.05 MeV photons. The bullets indicate the depths for which calculations were explicitly performed. The star indicates the effective dose rate at depth of 5 cm, evaluated through interpolation.

6.3. Dose rate coefficients for air submersion

(103) The air submersion exposure geometry involves an individual standing in a large volume of uniformly contaminated air. It is assumed that the individual is standing on an uncontaminated flat surface of infinite area. The source for the submersion dose calculations is a semi-infinite cloud containing a uniformly-distributed monoenergetic photon and electron emitter surrounding a human phantom standing on the soil at the air-ground interface. Fig. 5.5 (right) illustrates the irradiation geometry for the organ equivalent dose calculations.

(104) As for ground planar sources, organ equivalent dose rate coefficients in each phantom are computed using the environmental photon and electron data as recorded to the external ASCII file. It should be noted that for electron sources, the electrons do not only start from the surface of the coupling cylinder but also from within the volume of the cylinder, which is filled with contaminated air. Transport calculations for cylinder-surface source and cylinder-volume sources were performed separately.

(105) The effective dose rate coefficients of monoenergetic sources distributed uniformly in the atmosphere are shown in Tables 6.7 and 6.8 and in Fig. 6.9 and Fig. 6.10 as a function of photon and electron energies, respectively. A total of 25 source energies were selected from 0.01 to 8 MeV. The unit of the dose rate coefficients is nSv h^{-1} Bq^{-1} m^3. The air kerma and ambient dose equivalent rate coefficients at a height of 1 m above the ground are also listed in Table 6.7 for photon sources. The supplementary data of the organ equivalent dose rate coefficients can be found at the electronic data accompanying this report. Fig. 6.9 shows also the $\dot{h}^*(10)$, and demonstrates that the conservative approach is retained (i.e. the ambient dose equivalent is higher than the effective dose for all phantoms considered).

Table 6.7. Effective dose rate, ambient dose equivalent rate and air kerma rate coefficients for monoenergetic photons and air submersion.

Energy	Effective dose rate coefficient						$\dot{h}^{*}(10)$	$\dot{k}_a$
(MeV)	(nSv h^{-1} Bq^{-1} m^{3})							(nGy h^{-1} Bq^{-1} m^{3})
	Adult	15 yr	10 yr	5 yr	1 yr	Newborn		
0.010	2.10E-05	2.04E-05	2.81E-05	2.84E-05	3.32E-05	3.70E-05	2.50E-05	3.12E-03
0.015	8.54E-05	9.79E-05	1.40E-04	1.44E-04	1.58E-04	1.71E-04	1.13E-03	4.46E-03
0.020	2.31E-04	2.81E-04	3.25E-04	3.71E-04	3.74E-04	5.88E-04	3.18E-03	5.33E-03
0.030	9.72E-04	1.14E-03	1.25E-03	1.53E-03	1.70E-03	2.20E-03	6.61E-03	6.31E-03
0.040	2.26E-03	2.48E-03	2.66E-03	3.18E-03	3.54E-03	4.14E-03	1.08E-02	8.02E-03
0.050	3.76E-03	3.99E-03	4.29E-03	5.00E-03	5.56E-03	6.04E-03	1.30E-02	8.48E-03
0.060	5.19E-03	5.65E-03	5.98E-03	6.71E-03	7.39E-03	7.84E-03	1.68E-02	1.05E-02
0.070	6.92E-03	7.56E-03	7.85E-03	8.62E-03	9.47E-03	9.82E-03	2.06E-02	1.26E-02
0.080	8.65E-03	9.42E-03	9.74E-03	1.05E-02	1.15E-02	1.18E-02	2.41E-02	1.45E-02
0.100	1.11E-02	1.19E-02	1.27E-02	1.35E-02	1.46E-02	1.54E-02	2.87E-02	1.75E-02
0.150	1.95E-02	2.08E-02	2.17E-02	2.28E-02	2.38E-02	2.52E-02	4.54E-02	2.90E-02
0.200	2.77E-02	2.97E-02	3.07E-02	3.23E-02	3.31E-02	3.51E-02	6.18E-02	4.10E-02
0.300	4.36E-02	4.63E-02	4.76E-02	5.06E-02	5.14E-02	5.45E-02	9.20E-02	6.42E-02
0.400	5.91E-02	6.19E-02	6.38E-02	6.80E-02	6.94E-02	7.36E-02	1.19E-01	8.66E-02
0.500	7.48E-02	7.74E-02	7.98E-02	8.52E-02	8.75E-02	9.27E-02	1.45E-01	1.09E-01
0.600	9.10E-02	9.37E-02	9.62E-02	1.03E-01	1.06E-01	1.12E-01	1.71E-01	1.31E-01
0.800	1.27E-01	1.32E-01	1.33E-01	1.40E-01	1.46E-01	1.54E-01	2.27E-01	1.79E-01
1.000	1.64E-01	1.73E-01	1.73E-01	1.81E-01	1.87E-01	1.98E-01	2.83E-01	2.29E-01
1.500	2.58E-01	2.72E-01	2.70E-01	2.82E-01	2.87E-01	3.04E-01	4.19E-01	3.49E-01
2.000	3.55E-01	3.72E-01	3.68E-01	3.83E-01	3.86E-01	4.06E-01	5.52E-01	4.68E-01
3.000	5.51E-01	5.73E-01	5.68E-01	5.92E-01	5.85E-01	6.08E-01	8.11E-01	7.02E-01
4.000	7.52E-01	7.76E-01	7.73E-01	8.06E-01	7.84E-01	8.08E-01	1.06E+00	9.34E-01
5.000	9.57E-01	9.84E-01	9.83E-01	1.03E+00	9.86E-01	1.01E+00	1.31E+00	1.16E+00
6.000	1.17E+00	1.20E+00	1.20E+00	1.25E+00	1.19E+00	1.22E+00	1.56E+00	1.40E+00
8.000	1.59E+00	1.65E+00	1.64E+00	1.70E+00	1.62E+00	1.66E+00	2.06E+00	1.87E+00

Table 6.8. Effective dose rate coefficients for monoenergetic electrons and air submersion.

Energy (MeV)	Effective dose rate coefficient ($nSv\ h^{-1}\ Bq^{-1}\ m^3$)					
	Adult	15 yr	10 yr	5 yr	1 yr	Newborn
0.010	3.91E-09	1.37E-09	1.57E-09	5.85E-10	6.93E-10	4.46E-10
0.015	9.15E-09	3.88E-09	4.51E-09	1.88E-09	2.77E-09	1.28E-09
0.020	2.06E-08	9.19E-09	1.14E-08	3.87E-09	8.78E-09	2.48E-09
0.030	6.31E-08	3.77E-08	3.78E-08	3.23E-08	5.28E-08	4.30E-08
0.040	1.63E-07	1.18E-07	1.10E-07	1.85E-07	1.43E-07	1.23E-07
0.050	3.34E-07	2.60E-07	3.00E-07	4.19E-07	3.23E-07	2.82E-07
0.060	5.99E-07	4.83E-07	5.45E-07	7.14E-07	6.49E-07	6.00E-07
0.070	1.82E-06	1.60E-06	1.72E-06	1.96E-06	2.09E-06	1.91E-06
0.080	5.57E-06	5.84E-06	6.11E-06	6.11E-06	6.21E-06	5.55E-06
0.100	2.84E-05	3.00E-05	3.08E-05	3.04E-05	3.02E-05	2.85E-05
0.150	1.16E-04	1.30E-04	1.28E-04	1.27E-04	1.31E-04	1.32E-04
0.200	2.51E-04	2.60E-04	2.57E-04	2.64E-04	2.70E-04	2.68E-04
0.300	5.77E-04	5.81E-04	5.73E-04	5.79E-04	5.78E-04	5.34E-04
0.400	8.24E-04	8.10E-04	8.03E-04	7.90E-04	7.90E-04	7.76E-04
0.500	1.09E-03	1.05E-03	1.05E-03	1.02E-03	1.02E-03	1.05E-03
0.600	1.38E-03	1.31E-03	1.35E-03	1.28E-03	1.31E-03	1.55E-03
0.800	2.04E-03	1.86E-03	1.99E-03	1.90E-03	2.22E-03	3.26E-03
1.000	3.06E-03	2.56E-03	3.14E-03	3.08E-03	3.96E-03	5.90E-03
1.500	6.70E-03	5.23E-03	8.20E-03	8.50E-03	1.20E-02	1.66E-02
2.000	1.21E-02	1.08E-02	1.64E-02	1.75E-02	2.54E-02	3.32E-02
3.000	2.65E-02	2.81E-02	4.90E-02	4.65E-02	6.07E-02	7.08E-02
4.000	4.73E-02	5.51E-02	8.44E-02	8.31E-02	9.56E-02	1.18E-01
5.000	7.36E-02	9.02E-02	1.24E-01	1.26E-01	1.33E-01	1.74E-01
6.000	1.05E-01	1.32E-01	1.70E-01	1.73E-01	1.77E-01	2.40E-01
8.000	1.77E-01	2.26E-01	2.95E-01	2.74E-01	3.05E-01	4.00E-01

(106) Regarding the age-dependency of the coefficients, it was observed that in general, the smaller the body mass of the phantom, the higher the organ and effective dose due the smaller amount of body shielding of internal organs in the younger and smaller reference phantoms. The difference in effective dose between the adult and the newborn is highest at 0.01 MeV photon energy (150%), while it is less than 40% above a photon energy of 0.07 MeV.

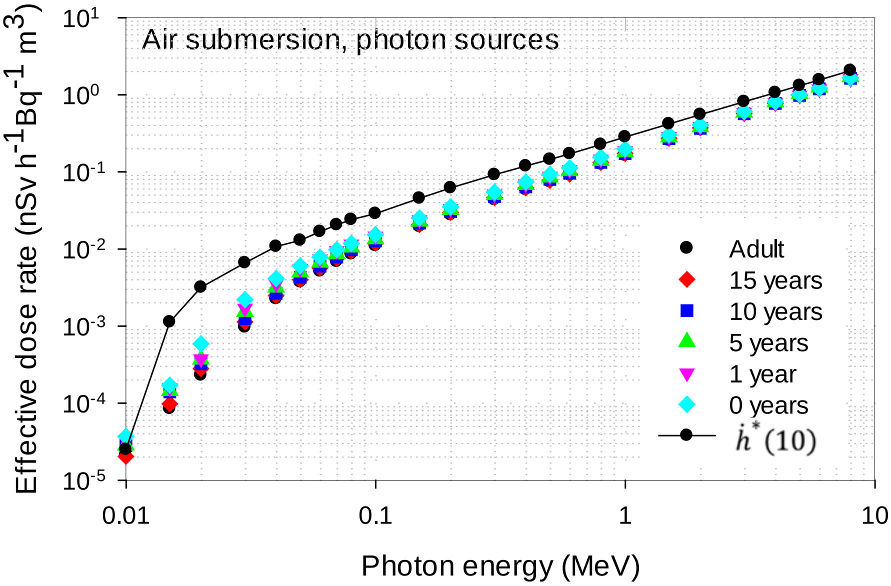

Fig. 6.9. Effective dose rate coefficients for monoenergetic photon sources distributed uniformly in the atmosphere as a function of photon energy and ambient dose equivalent $\dot{h}^{*}(10)$ at 1 m above ground.

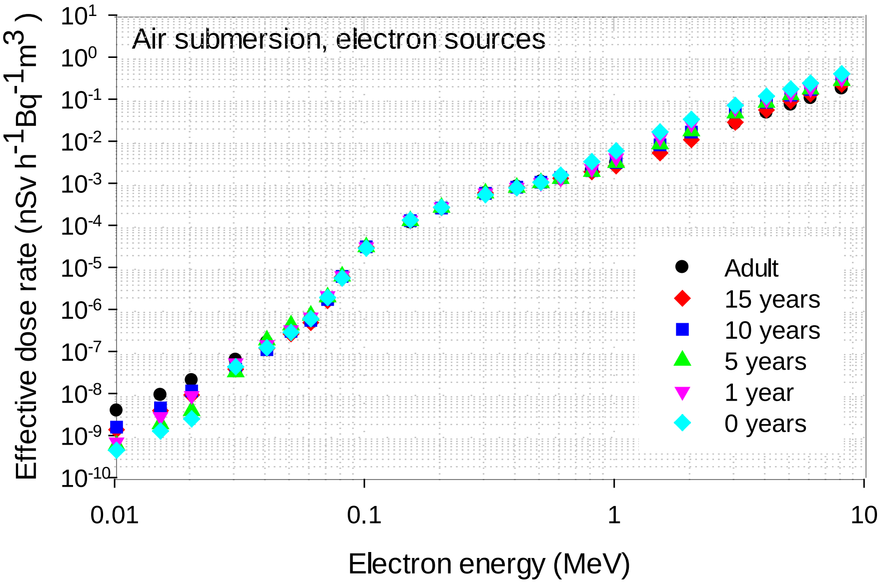

Fig. 6.10. Effective dose rate coefficients for monoenergetic electron sources distributed uniformly in the atmosphere as a function of electron energy.

6.4. Dose rate coefficients for water immersion

(107) Dose rate coefficients for water immersion were calculated under the assumption that an individual is completely immersed in an infinite volume of uniformly contaminated water. For the water photon exposure, the whole spherical geometry is sampled, including those voxels in the phantom matrix outside the body that are identified as water.

(108) Contributors to the organ equivalent doses from electron sources in the water immersion geometry are the primary electrons emitted from the water near the body surface and the bremsstrahlung photons generated by electron interactions in water.

(109) Calculations were performed for 25 monoenergetic sources of photons and electrons ranging from 0.01 to 8 MeV and for all male and female adult and paediatric phantoms. Tables 6.9 and 6.10 present the evaluated coefficients of effective dose rate for photon and electron sources, respectively, distributed uniformly in water, while Fig. 6.11 and Fig. 6.12 depict those same data as a function of photon and electron energies, respectively. The data are given in units of nSv h^{-1} Bq^{-1} m^3.

Table 6.9. Effective dose rate coefficients for monoenergetic photon sources and water immersion.

Energy	Effective dose rate coefficient (nSv h^{-1} Bq^{-1} m^3)					
(MeV)	Adult	15 yr	10 yr	5yr	1yr	newborn
0.010	3.62E-08	2.87E-08	4.91E-08	4.43E-08	5.14E-08	7.66E-08
0.015	1.64E-07	1.86E-07	2.89E-07	3.00E-07	3.41E-07	4.67E-07
0.020	4.95E-07	5.88E-07	7.19E-07	9.08E-07	9.11E-07	1.27E-06
0.030	2.18E-06	2.45E-06	2.78E-06	3.81E-06	4.04E-06	5.13E-06
0.040	5.01E-06	5.77E-06	6.60E-06	8.10E-06	9.07E-06	1.07E-05
0.050	8.53E-06	9.66E-06	1.06E-05	1.29E-05	1.46E-05	1.64E-05
0.060	1.21E-05	1.36E-05	1.50E-05	1.77E-05	1.97E-05	2.24E-05
0.070	1.57E-05	1.75E-05	1.92E-05	2.24E-05	2.48E-05	2.79E-05
0.080	1.93E-05	2.13E-05	2.33E-05	2.69E-05	2.98E-05	3.32E-05
0.100	2.66E-05	2.85E-05	3.12E-05	3.57E-05	3.92E-05	4.35E-05
0.150	4.32E-05	4.64E-05	4.97E-05	5.59E-05	6.03E-05	6.61E-05
0.200	6.00E-05	6.37E-05	6.80E-05	7.59E-05	8.18E-05	8.92E-05
0.300	9.41E-05	9.92E-05	1.05E-04	1.17E-04	1.25E-04	1.36E-04
0.400	1.29E-04	1.36E-04	1.43E-04	1.58E-04	1.69E-04	1.83E-04
0.500	1.65E-04	1.72E-04	1.82E-04	1.99E-04	2.13E-04	2.30E-04
0.600	2.01E-04	2.10E-04	2.21E-04	2.41E-04	2.57E-04	2.76E-04
0.800	2.74E-04	2.84E-04	2.98E-04	3.23E-04	3.40E-04	3.65E-04
1.000	3.62E-04	3.76E-04	3.93E-04	4.25E-04	4.46E-04	4.75E-04
1.500	5.71E-04	5.87E-04	6.12E-04	6.57E-04	6.84E-04	7.22E-04
2.000	7.82E-04	8.03E-04	8.34E-04	8.90E-04	9.24E-04	9.71E-04
3.000	1.21E-03	1.25E-03	1.29E-03	1.36E-03	1.41E-03	1.47E-03
4.000	1.66E-03	1.70E-03	1.76E-03	1.85E-03	1.90E-03	1.99E-03
5.000	2.12E-03	2.18E-03	2.25E-03	2.35E-03	2.40E-03	2.51E-03
6.000	2.60E-03	2.67E-03	2.75E-03	2.87E-03	2.91E-03	3.04E-03
8.000	3.62E-03	3.70E-03	3.82E-03	3.99E-03	3.98E-03	4.14E-03

Table 6.10. Effective dose rate coefficients for monoenergetic electron sources and water immersion.

Energy	Effective dose rate coefficient (nSv h^{-1} Bq^{-1} m^3)					
(MeV)	Adult	15 yr	10 yr	5yr	1yr	Newborn
0.010	2.97E-12	1.31E-12	1.13E-12	5.15E-13	4.72E-13	5.26E-13
0.015	1.08E-11	4.08E-12	3.92E-12	1.77E-12	1.66E-12	1.76E-12
0.020	2.90E-11	1.30E-11	1.45E-11	5.95E-12	1.37E-11	1.39E-11
0.030	9.75E-11	6.09E-11	7.18E-11	8.71E-11	8.61E-11	1.11E-10
0.040	2.68E-10	2.01E-10	2.60E-10	3.32E-10	3.13E-10	4.11E-10
0.050	5.92E-10	4.96E-10	6.28E-10	8.01E-10	7.60E-10	9.71E-10
0.060	1.13E-09	9.71E-10	1.19E-09	1.56E-09	1.46E-09	1.97E-09
0.070	2.91E-09	2.54E-09	2.89E-09	3.54E-09	3.37E-09	4.17E-09
0.080	8.78E-09	8.04E-09	8.56E-09	9.52E-09	9.32E-09	1.03E-08
0.100	4.04E-08	3.88E-08	4.02E-08	4.10E-08	4.20E-08	4.35E-08
0.150	1.84E-07	1.80E-07	1.83E-07	1.85E-07	1.87E-07	1.93E-07
0.200	3.52E-07	3.45E-07	3.51E-07	3.54E-07	3.58E-07	3.67E-07
0.300	7.07E-07	6.97E-07	7.07E-07	7.09E-07	7.19E-07	7.38E-07
0.400	1.09E-06	1.05E-06	1.08E-06	1.08E-06	1.11E-06	1.15E-06
0.500	1.51E-06	1.43E-06	1.50E-06	1.49E-06	1.53E-06	1.64E-06
0.600	1.99E-06	1.84E-06	1.97E-06	1.95E-06	2.01E-06	2.27E-06
0.800	3.11E-06	2.77E-06	3.15E-06	3.09E-06	3.50E-06	4.33E-06
1.000	4.50E-06	3.92E-06	4.79E-06	4.80E-06	6.17E-06	8.24E-06
1.500	1.01E-05	8.44E-06	1.24E-05	1.42E-05	2.18E-05	3.04E-05
2.000	1.83E-05	1.61E-05	2.66E-05	2.96E-05	4.70E-05	6.35E-05
3.000	4.55E-05	4.89E-05	7.66E-05	8.04E-05	1.09E-04	1.44E-04
4.000	8.29E-05	9.41E-05	1.43E-04	1.47E-04	1.82E-04	2.45E-04
5.000	1.32E-04	1.52E-04	2.18E-04	2.29E-04	2.68E-04	3.66E-04
6.000	1.93E-04	2.23E-04	3.04E-04	3.27E-04	3.68E-04	5.07E-04
8.000	3.56E-04	4.06E-04	5.23E-04	5.70E-04	6.23E-04	8.46E-04

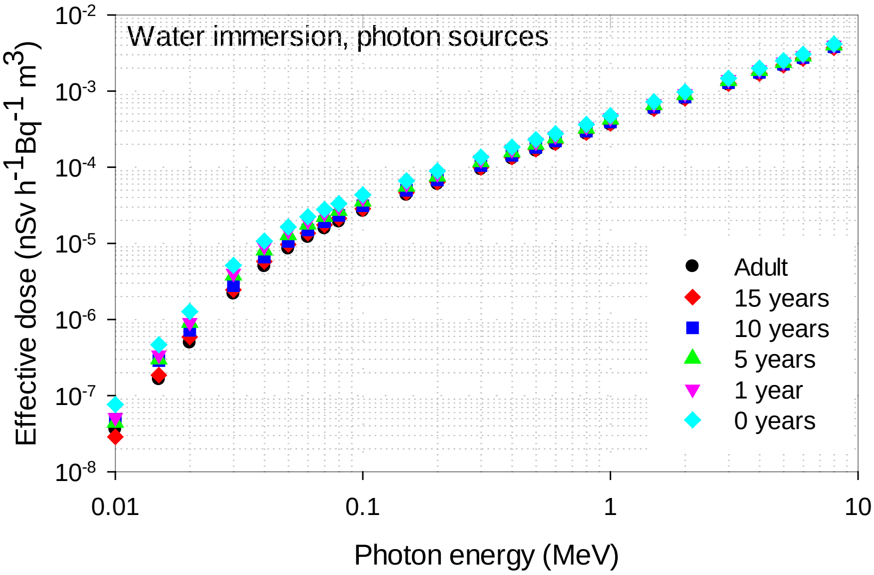

Fig. 6.11. Effective dose rate coefficients for monoenergetic photon sources distributed uniformly in the water (i.e. water immersion).

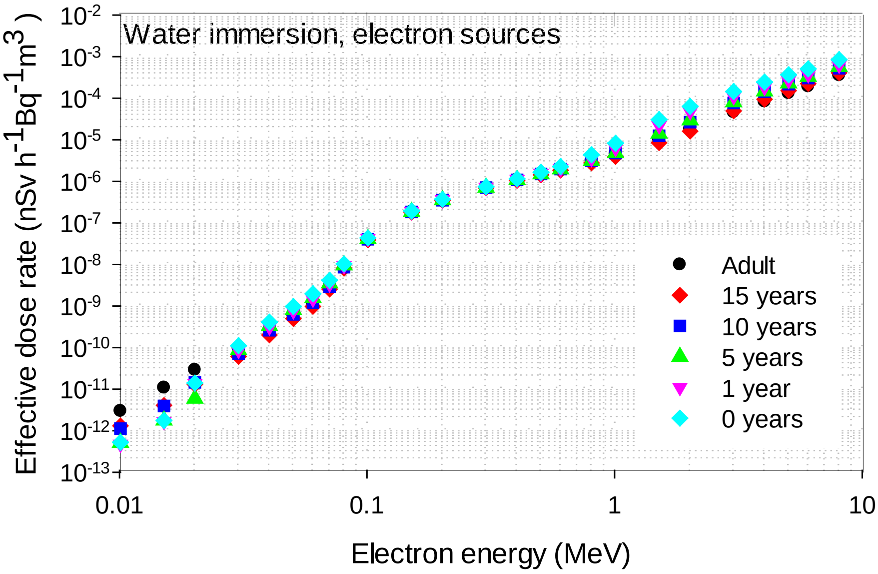

Fig. 6.12. Effective dose rate coefficients for monoenergetic electron sources distributed uniformly in the water (i.e. water immersion).

(110) Fig. 6.13 shows the effective dose rate of the newborn for monoenergetic electrons, together with the skin equivalent dose multiplied by tissue weighting factor, 0.01. The skin equivalent dose has been computed with the polygon mesh-type phantoms in order to evaluate the dose at the radiosensitive region of the epidermis which is considered to be 50 to 100 µm below the skin surface (see Annex B). It can be seen, that up to about 1 MeV, the dose to the skin is the main contributor to the effective dose for environmental electron exposures.

(111) The age-dependency of the effective dose coefficients is similar to the case of immersion to contaminated air, the effective dose for newborns being up to 150% higher than for adults, for photon energies of 0.02 MeV.

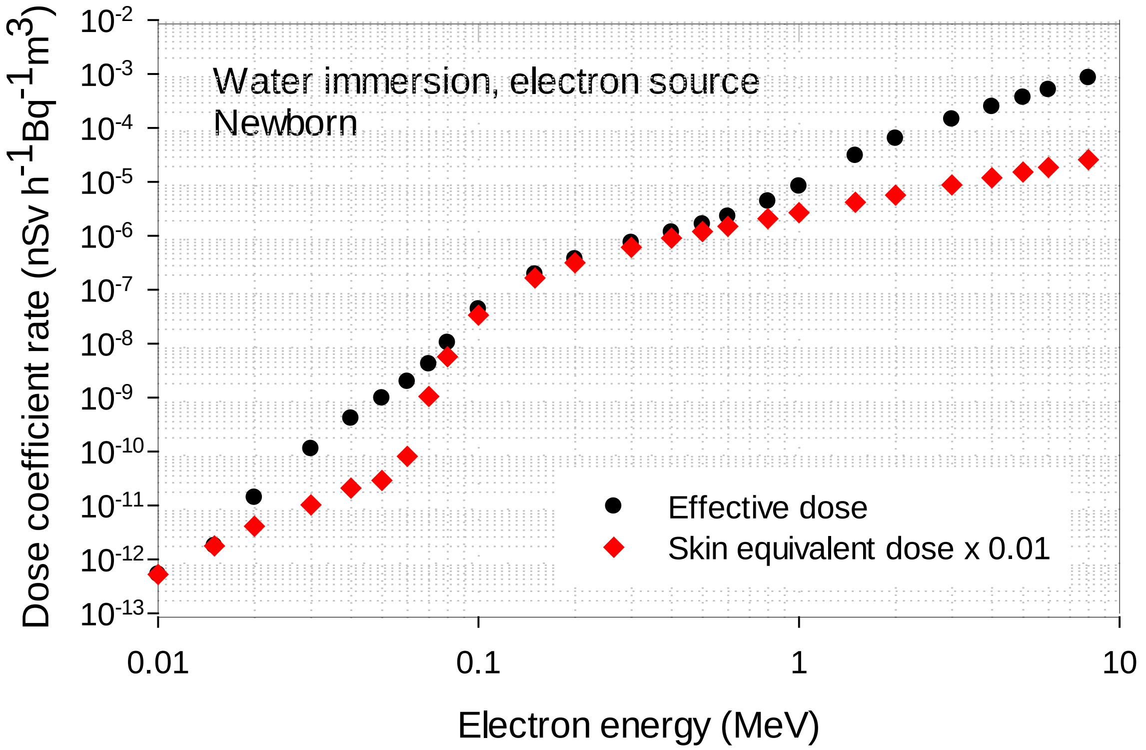

Fig. 6.13. Comparison of effective and skin dose rate coefficients for monoenergetic electrons distributed uniformly in the water (i.e. water immersion), for a newborn phantom. For comparison's sake, the skin dose rate has been multiplied by 0.01 i.e. the w_T of skin.

6.5. Verification of the calculations (spot-checks)

(112) The environmental fields specific for the exposure situations selected as being representative of the most common exposure scenarios were calculated specifically for this report by Daiki Satoh, Japan Atomic Energy Agency (JAEA), a member of the Task Group, using the Monte Carlo code PHITS (see section 4). The organ equivalent dose calculations for all geometries, particles and phantoms were also performed by D. Satoh with PHITS – see previous sections. Separate calculations were performed for skin dosimetry by Yeon Soo Yeom (Hanyang University) using GEANT4 and the mesh format of the phantoms – see Annex B on skin dosimetry. The reference coefficients tabulated in this report have been evaluated by the above data after smoothing and least squares polynomial fitting.

(113) For quality assurance purposes, several organ equivalent dose data sets have been re-calculated by different members of the Task Group using the same environmental fields and the same reference computational phantoms but different radiation transport codes. The Monte Carlo codes used were the GEANT4 -YS Yeom (Hanyang University), EGSnrc - H Schlattl (Helmholtz Zentrum München, HMGU) and MCNPX - SJ Yoo (Korean Institute of Nuclear Safety, KINS), MCNP6 - J Jansen (Public Health England, PHE), MCNPX – C Lee, National Cancer Institute, NCI), Visible Monte Carlo - J Hunt (Instituto de Radioproteção e Dosimetria, IRD). This section describes briefly the Monte Carlo calculations performed for the spot-checks.

6.5.1. GEANT4 (user Hanyang University)

(114) The GEANT4 code is a general-purpose Monte Carlo code, which was developed in the C++ programming language, exploiting software engineering and object-oriented technology (Agostinelli et al., 2003). Since the first public release in 1998, the GEANT4 code has been improved and maintained by the GEANT4 collaboration of various international research groups (http://geant4.cern.ch/). The GEANT4 code can simulate a large set of particles, covering a wide energy range from 100 eV to 10 TeV or, for some particles, 10 PeV (Allison et al., 2016). It is widely used in various applications including radiation dosimetry, medical application, space science and accelerator physics.

(115) GEANT4 Version 10.2 was used for the calculations of this report for the spot-check to validate organ equivalent dose rate coefficients for soil contamination, photon and electron sources. The reference voxel phantoms were implemented in the GEANT4 code by using the G4VNestedParameterisation class, which, among the GEANT4 classes, provides the best features for implementation of voxel geometry (Schümann et al., 2012). The physics library of the G4EmLivermorePhysics, including EPDL97 (Cullen et al., 1997), EEDL (Perkins et al., 1991) and EADL (Perkins et al., 1997), was used to simulate photons and electrons. A secondary production cut value for all the particles in all the media was set to a range of 1 μm for the precise simulation.

(116) Organ equivalent dose rate coefficients for monoenergetic photons and electrons (0.03–3 MeV) of some soil-contamination cases were calculated by directly using the phase-space source data as recorded on the coupling cylinder in the first step of calculation method (see 5.1). During the calculations, from the source data, a particle was randomly selected and its position and direction were rotated by an angle randomly selected between 0° and 360° on the z-axis (i.e. the centre axis of the coupling cylinder); this approach can avoid any undesirable direction bias at the given number of the particles in the source data, considering that the irradiation geometry is cylindrically symmetric.

(117) For photons, relative statistical uncertainties of the calculated organ equivalent doses were generally below 1% for larger organs and 4% for smaller organs. For electrons above 0.2 MeV, the uncertainties were generally below 2% for larger organs and 10% for smaller organs, while for lower energy electrons, most of the calculated organ equivalent doses had large statistical uncertainties, with the exceptions of the skin doses whose uncertainties were all below 0.1%.

6.5.2. MCNP6 (user PHE)

(118) The Monte Carlo N-Particle code system MCNP (Los Alamos National Laboratory (LANL), Los Alamos, NM) version 6.1 (Pelowitz, 2013a,b) has been used in Fortran 90 code form. The source code has been patched according to Michael Lorne Fensin publication on the MCNP-Forum at Monday 22 September 2014 to allow for convenient voxel sampling within a lattice. In addition, a Fortran 90 source routine has been inserted to allow for the reading of the source files describing the environmental field. This source routine reads the whole source file the first time and applies a source rotation over a sampled (random) angle during successive file reads. The Fortran 90 code has been compiled with the Intel Fortran compiler (Intel Corporation, Santa Clara, CA). For quality control, the executable was tested on the verification samples and differences have been verified, documented and forwarded to Los Alamos National Laboratory.

(119) The cross-section library used was the MCPLIB04 for photons and EL03 for electrons, both being the MCNP6 default. For all organs, except the active marrow and

endosteum, and photon exposures the organ equivalent doses are calculated without electron transport assuming electron equilibrium, except for air submersion, where for photon energies $\geq$ 1 MeV electron transport is performed. For all organs, the tally 6 track length heating number estimator, i.e. a track length estimator with an internally calculated fluence-to-dose function, is used to derive the absorbed dose; an exception is the calculation of active bone marrow and endosteum absorbed dose rate coefficients for photon exposures, where the dose enhancement factors are used to compensate for the lack of electron equilibrium and the tally 4 track length estimator is modified by a fluence-to-dose response function (see Annex A). The validation calculations performed were for air and water immersion, photon and electron sources and for all ICRP reference paediatric phantoms.

6.5.3. MCNPX (user KINS)

(120) The Monte Carlo particle transport code MCNPX 2.7.0 (Pelowitz, 2011) was used together with the cross section library MCNPLIB04 and El03 for calculating the absorbed doses to the organs of the ICRP adult and paediatric reference phantoms due to unit source intensity of specified energies of photons for air submersion and water immersion exposure situations. For the specified photon energies, 25 energy bins are used for the range of 0.01 to 10 MeV. Absorbed doses for organs and tissues were calculated by applying the F6 tally in MCNPX code. The transport calculations were performed for the source volume within the converging of distances (Yoo et al., 2013a,b), which are determined by a simplified calculation model.

(121) To resolve the poor statistics in small organs (e.g. the thymus and the lymph nodes), an approach, called equivalent dose ratio method (Yoo et al., 2013a), was applied by assuming that the energy spectrum of photons entering the body would not significantly change with the geometrical ranges beyond a few mean free paths. The ratios of the absorbed doses for small organs to those received by the muscle (reference organ) were calculated at 50 m radius (reference distance) and for each energy bin. After confirming that the deviations of the ratios are within 10% while the radius of the air volume varies, these ratios were used to obtain doses to small organs.

(122) The validation calculations performed were for air and water immersion, photon beams and for all ICRP reference paediatric phantoms.

6.5.4. MCNPX (user NCI)

(123) The Monte Carlo N-Particle eXtended (MCNPX) Version 2.7.0 (Pelowitz, 2011) was employed to the verification of the calculations of organ equivalent dose coefficients at the National Cancer Institute. The verification was focused on the soil contamination with the depth of 0.0 mfp (i.e. surface contamination) for 13 photon energy bins ranging from 0.01 to 5 MeV. The newborn and 15-year-old ICRP paediatric phantoms were included in the verification process. Organ equivalent dose rate coefficients were calculated for over 30 organs and tissues and delivered to JAEA for comparison with the data from PHITS code.

(124) Source data for soil contamination computed at JAEA by PHITS, called phase space data, was delivered to the NCI. Since MCNPX writes and reads external source definition through the Surface Source Write/Read (SSW/SSR) routines, the source data from PHITS were not directly compatible with MCNPX. The source data from PHITS in ASCII format were converted into the binary format using an in-house script according to the description of the SSW routine in MCNPX.

(125) The cross-section library, mcplib04 and el03, were adopted for photons and electrons, respectively, in the verification process. A total of 500 million particle histories were used to achieve acceptable statistical errors. Default energy cut off, 0.001 MeV, was used for both photon and electron transport. Absorbed dose to organs and tissues was calculated by using F8 energy deposition tally. The high-performance computing server installed at the NCI was utilized to facilitate the large amount of Monte Carlo calculations.

6.5.5. EGSnrc (user HMGU)

(126) For calculations of photon organ equivalent dose coefficients a code developed specifically for organ equivalent dose calculations (Schlattl et al., 2012) has been used, employing the electron-gamma-shower code system EGSnrc Version v4-2-3-1 (Kawrakow et al., 2009). EGSnrc is an extended and improved version of EGS4 (Nelson et al., 1985), maintained by the National Research Council of Canada (NRC). The transport of photons and electrons can be simulated for particle kinetic energies from a few keV up to several hundred GeV, although simulations performed in this study were made only for photons in the energy range of 0.01 to 8 MeV.

(127) For photon transport, bound Compton scattering and secondary photo-electrons from K, L, and M shells are considered for all energies. In both cases, resulting fluorescence or Auger and Coster-Kronig electrons are followed. The input data for photon cross sections agree with those of the XCOM database (Berger and Hubbell, 1987).

(128) For the calculations performed for this report, photon transport is terminated when the photon energy falls below 2 keV. Secondary electrons are followed until their kinetic energy drops below 20 keV.

(129) The number of histories followed varied between 450 million at 0.01 MeV to 100 million at 8 MeV, resulting in coefficients of variance for most organs below 1%, and only in exceptions reaches up to 4% (e.g. at low energies for gall bladder).

(130) By assuming rotational symmetry, the phase-space source data of the coupling cylinder was converted into a discrete probability density function ($\phi(E, h, \sin\vartheta)$) with E being the particle energy, h its source position on the cylinder and ϑ its direction relative to the horizontal plane. At the lids of the cylinder the probability density function was $\phi(E, \sin\vartheta)$.

(131) The source sampling in the EGSnrc user code was performed by the cumulative density function obtained from the probability density function and enforcing rotational symmetry.

(132) The validation calculations performed were for air submersion and ground contamination, photon beams and the ICRP adult reference phantoms.

6.5.6. Visible Monte Carlo (user IRD)

(133) Visible Monte Carlo (VMC) (Hunt et al., 2004) has been developed at the Instituto de Radioproteção e Dosimetria from 1994 to the present date. VMC transports photons, electrons, alpha particles and protons through voxel and general geometrical structures. Bremsstrahlung production and transport is not considered for low Z materials. The photon energy range considered for the spot check calculations was 0.03 to 3 MeV. VMC benefits from an extensive graphical interface that shows all aspects of the simulated geometry and also the photon interactions with the environment and the phantom.

(134) VMC version March 2016 was used for the spot-check calculations to validate organ equivalent dose coefficients for water contamination and the adult phantoms. The cross

section library used is the NIST XCOM database (Berger and Hubbell, 1987) and the size of the water sphere considered for each photon energy was based on the maximum distance travelled by the simulation of the transport of 10^8 photons in water. The photon transport is terminated when the photon suffers a photoelectric effect. The statistical uncertainties of the calculated organ equivalent doses were estimated to be below 1% for the larger organs and below 5% for smaller organs.

6.5.7. Comparison of dose rate coefficients calculated with different codes and comparisons with other work

(135) Fig. 6.14 shows the effective dose for monoenergetic photons, for the various age-phantoms and ground plane surface source (left) and air submersion (right), as estimated by different calculators and codes. As it can be seen, the agreement of computed dose rate coefficient by the different Monte Carlo codes is within 10% and in most cases below 4%. Also shown are values of effective dose, as given in Federal Guidance Report (FGR) of the USA (Bellamy et al., 2018). Note that the latter data have been obtained for environmental field data estimated by Bellamy et al using stylized hermaphroditic models of the ICRP reference individuals (Cristy and Eckerman, 1987; Han et al., 2006).

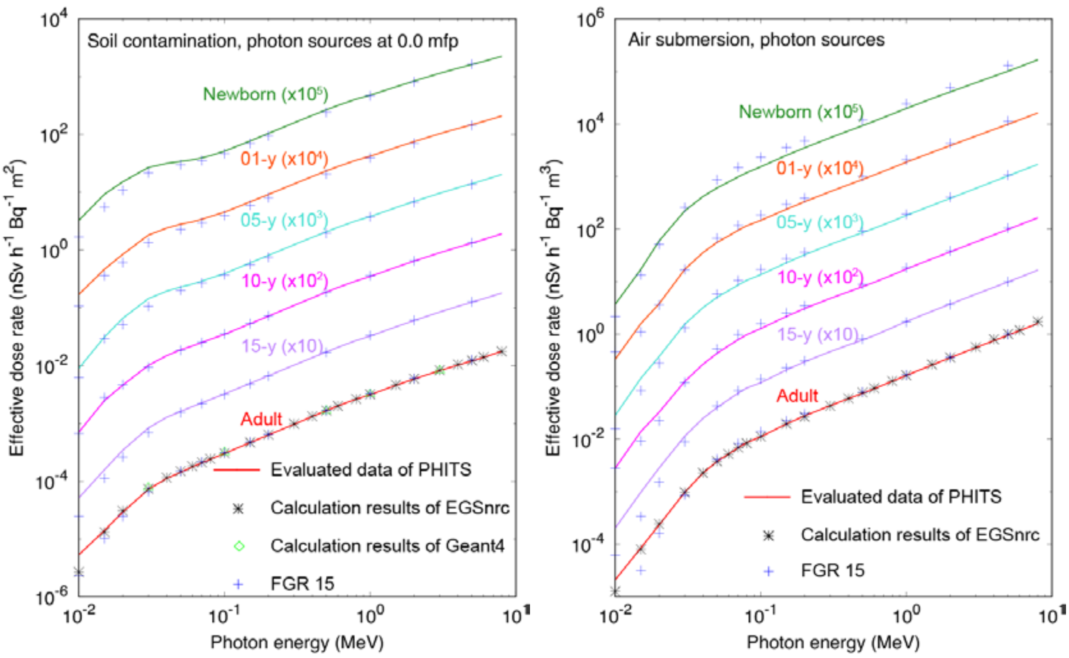

Fig. 6.14. Effective dose for photon ground plane surface source (left) and air submersion (right), as estimated by different calculators and codes. The PHITS data set shows the data after smoothing. For better visibility, the data were plotted multiplied by a factor of 10-10^5. FGR 15 indicates the Federal Guidance Report (Bellamy et al., 2018).

(136) Fig. 6.15 shows selected values of organ equivalent dose rates for a ground planar source emitting monoenergetic electrons, for the male adult phantom, as computed by PHITS and GEANT4. It can be seen, that, as mentioned in section 6.1, the values which contribute to the effective dose less than 1% are set to zero. Fig. 6.16 shows organ equivalent dose rates for the 15-year-old male phantom and photons, as computed by MCNPX and PHITS for ground planar source emitting monoenergetic photons. Similarly, Fig. 6.17 and Fig. 6.18

show organ equivalent dose rate coefficients for air submersion and water submersion, respectively, and photons.

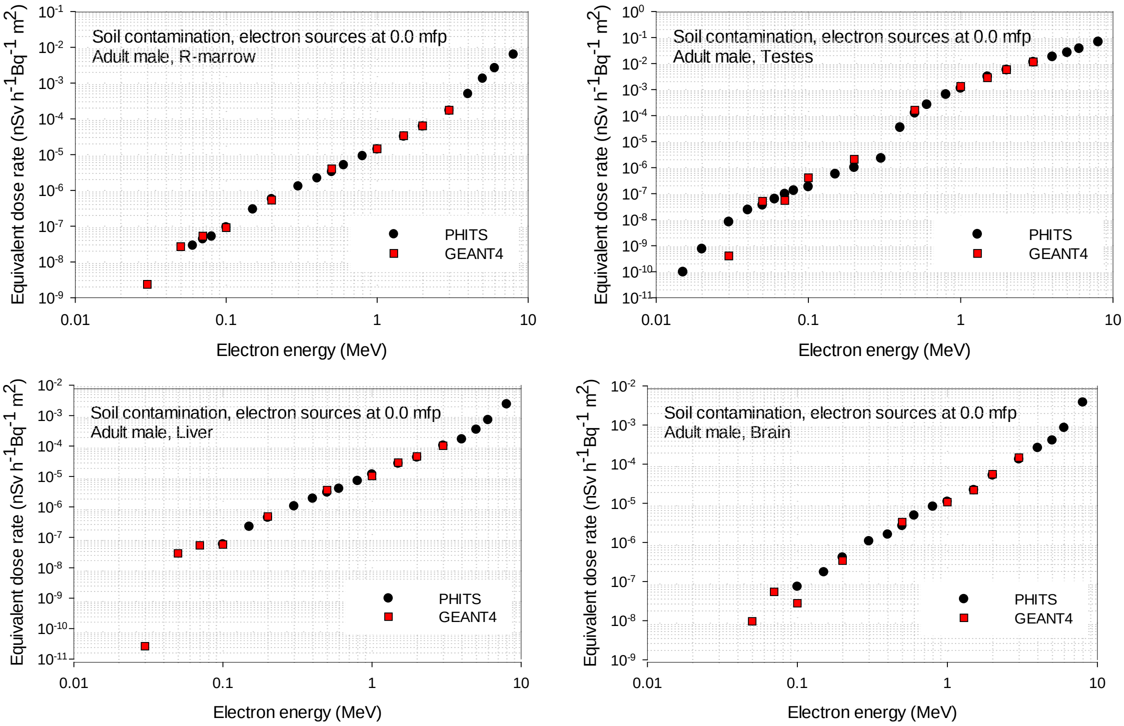

Fig. 6.15. Organ equivalent doses for red bone marrow, testes, liver and brain of the adult male phantom for a ground plane source emitting electrons, as calculated by PHITS and GEANT4.

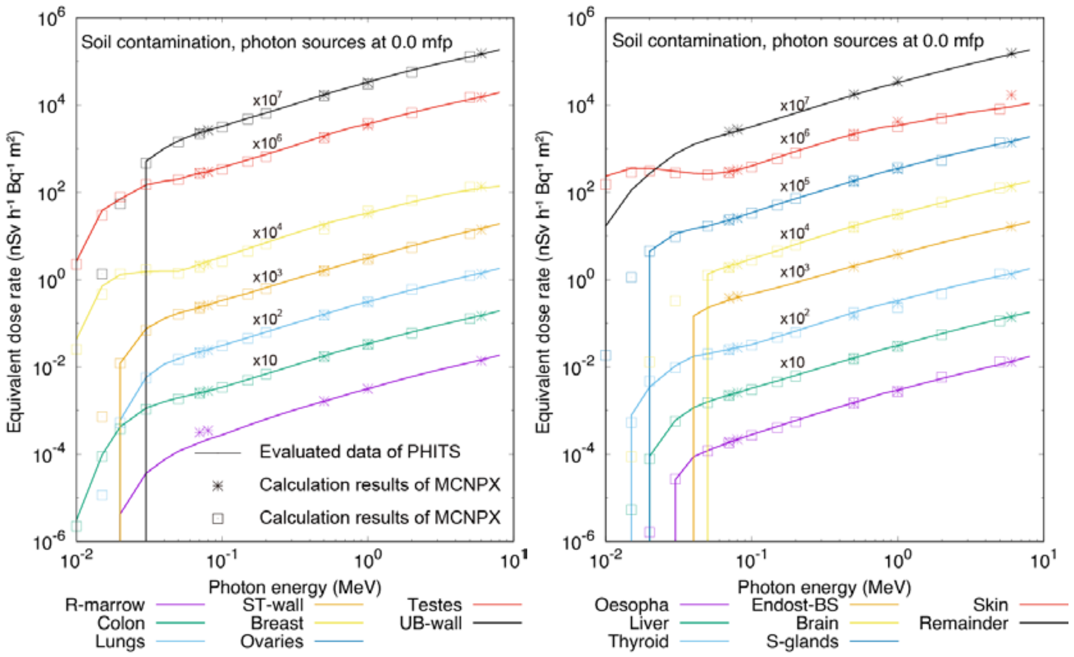

Fig. 6.16. Organ equivalent doses for the 15-year-old male phantom, as calculated by PHITS and MCNP, for ground contamination on the surface (photons). The asterisks and open squares indicate calculations made at the Korean Institute of Nuclear Safety and Public Health

England, respectively (Vertical lines indicate that data at lower energies have been set to zero).

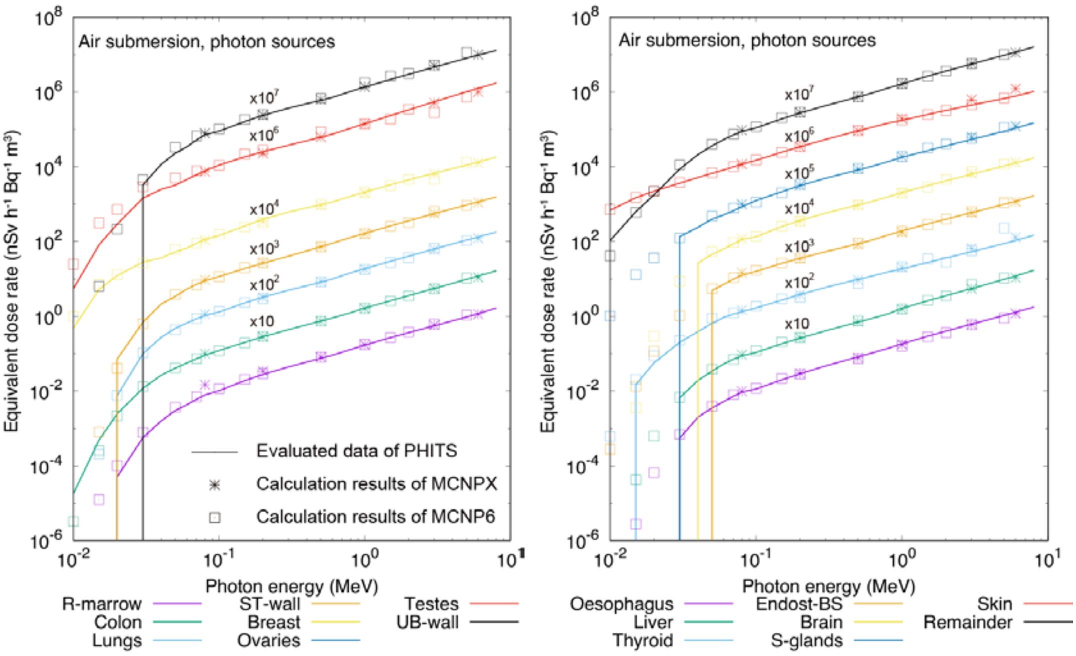

Fig. 6.17. Organ equivalent doses for the 15-year-old male phantom, as calculated by PHITS and MCNP, for submersion in contaminated air (photons). The asterisks and open squares indicate calculations made at the Korean Institute of Nuclear Safety and Public Health England, respectively (Vertical lines indicate that data at lower energies have been set to zero).

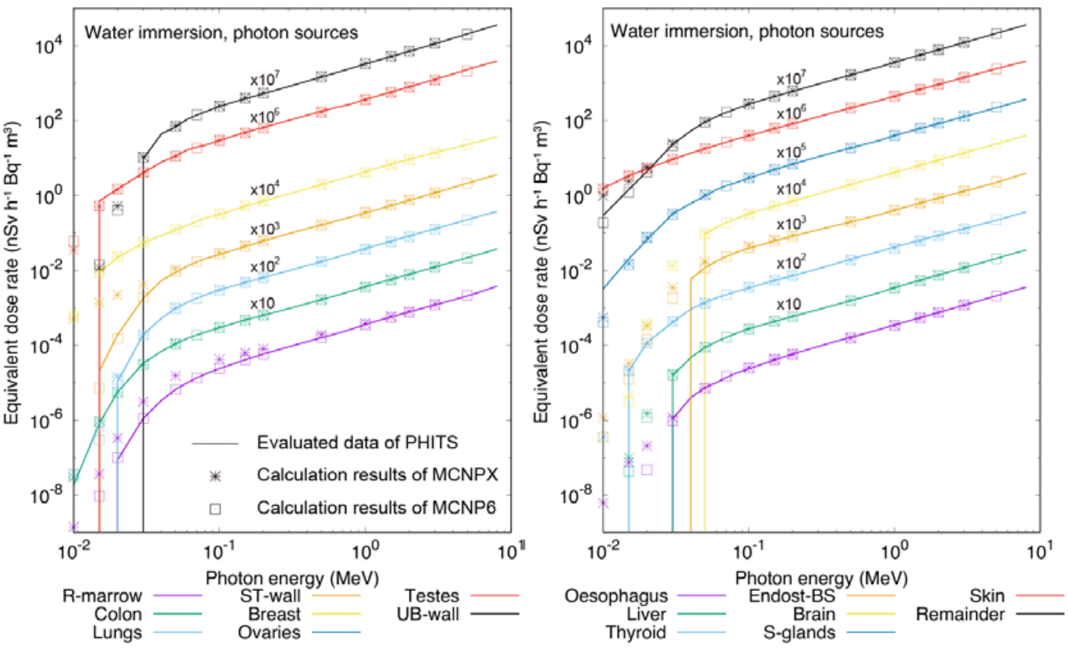

Fig. 6.18. Organ equivalent doses for the 15-year-old male phantom, as calculated by PHITS and MCNP, for submersion in contaminated water (photons). The asterisks and open squares indicate calculations made at the Korean Institute of Nuclear Safety and Public Health

England, respectively (Vertical lines indicate that data at lower energies have been set to zero).

6.6. Dose rate coefficients for monitoring - Air kerma and ambient dose equivalent rates

(137) The ambient dose equivalent rates were compared to the effective dose rates for reference adults and reference newborn, 1-year-old, 5-year-old, 10-year-old and 15-year-old phantoms (see Fig. 6.2 to Fig. 6.6 and Fig. 6.9), as well as to air kerma. It was shown that the ambient dose equivalent sufficiently overestimates effective doses, independent of age, for planar sources on and below the ground surface, in addition to immersion in a radioactive cloud. As previously mentioned, opposite trends are observed for ground contamination and for the newborn, 1-year-old, and 5-year-old phantoms at energy of 0.01 MeV where the effective dose rate coefficient is higher than the ambient dose equivalent rate, $\dot{h}^*(10)$. The difference between air kerma and effective dose was found to be smaller than the difference between ambient dose equivalent and effective dose. For example, the air kerma is a closer approximation to the effective dose for the environmental exposures examined.

(138) In a previous study, Saito and Petoussi-Henss (2014) presented dose coefficients relating ambient dose equivalent rates to radionuclide density for sources exponentially distributed in the ground. The authors compared the ratio of ambient dose equivalent to air kerma obtained by simulation to the ratios measured at hundreds of locations in Japan which have been contaminated with radioactive ^{137}Cs, ^{134}Cs, ^{131}I, ^{110m}Ag and ^{129m}Te after the Fukushima NPP accident in 2011. Good agreement was observed in all cases.

(139) Fig. 6.19 and Fig. 6.20 show the ambient dose equivalent rates and air kerma rates at 1 m above ground, respectively, for planar sources at different depths in soil. It can be seen that both quantities depend strongly on source soil depth and as the depth increases, both the ambient dose equivalent rates and air kerma rates decrease because of the shielding effect of the soil. The ambient dose equivalent rates at 0.2 mfp depth is about 40-70% of that at 0.0 mean free path for source energies higher than 0.015 MeV. For 1.0 mfp the reduction of the ambient dose equivalent rate coefficient is more pronounced, and the ambient dose equivalent is less than 80% of that on the surface. Fig. 6.21 shows the ambient dose (rate), which is a newly proposed operational quantity to substitute the ambient dose equivalent (see section 8.4 and ICRU Report xx (in preparation)). It can be seen that generally the values of ambient dose rate are lower than those of ambient dose equivalent rate, and differences are more pronounced at energies below 0.015 - 0.07 MeV. However, it was shown that ambient dose rate also is a good estimator of effective dose for this type of field.

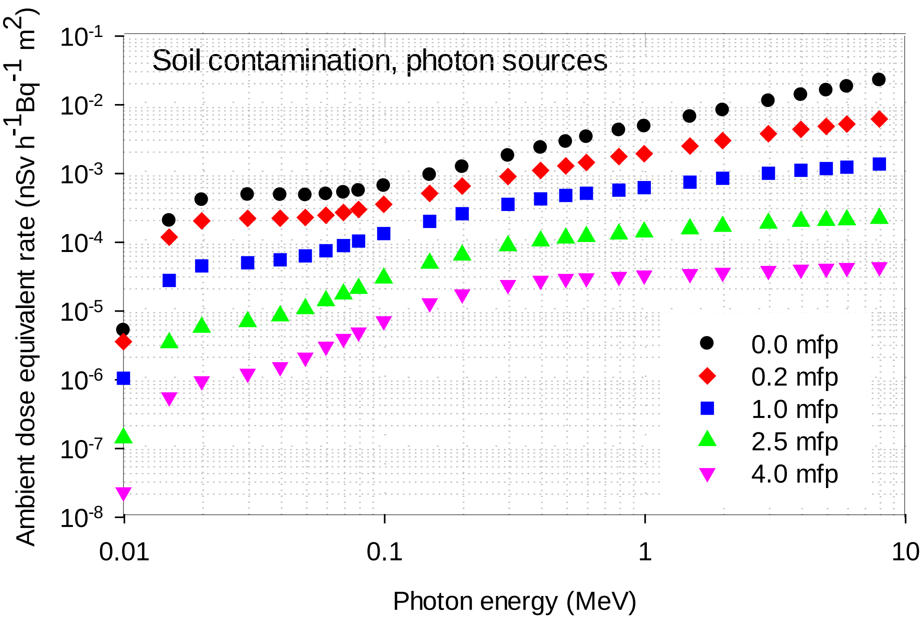

1815
1816 Fig. 6.19. Ambient dose equivalent rates for different depths in the soil expressed as mean
1817 free paths (mfp).
1818
1819

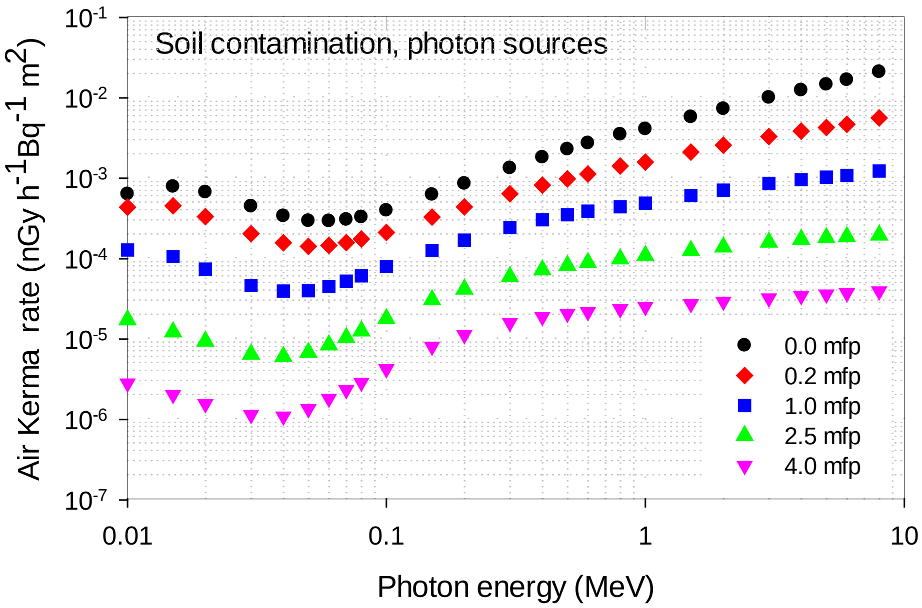

1820
1821
1822 Fig. 6.20. Air kerma rate at 1 m above ground, for different depths in the soil expressed as
1823 mean free paths (mfp).
1824
1825
1826
1827

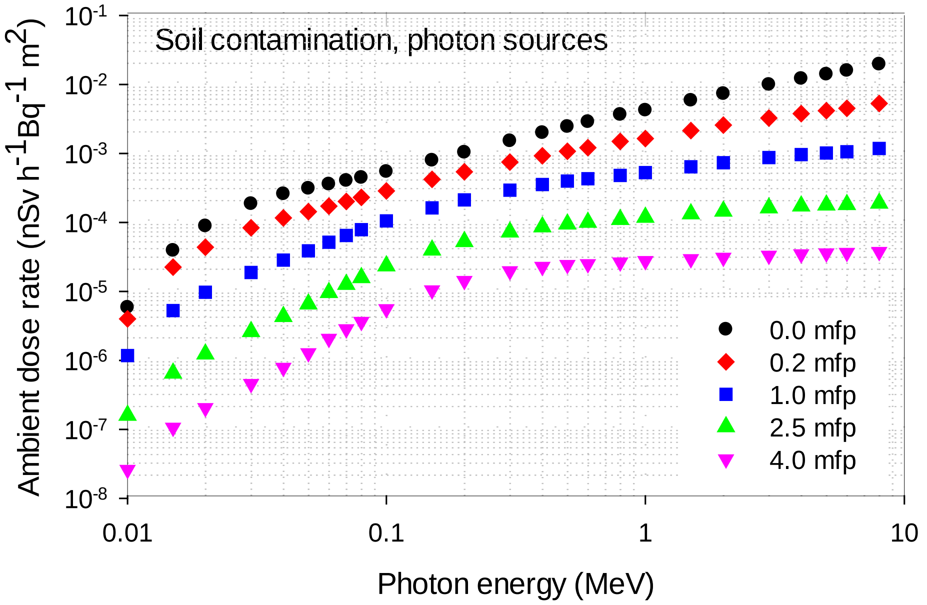

Fig. 6.21. Ambient dose rate, a quantity newly proposed by ICRU (ICRU, in preparation)–see section 8.4 - for different depths in the soil expressed as mean free paths (mfp).

7. EQUIVALENT AND EFFECTIVE DOSE RATE COEFFICIENTS FOR RADIONUCLIDES (STEP3)

7.1. Coefficients for equivalent dose rate to organs and tissues

(140) Radionuclide specific equivalent dose rate coefficients, $\dot{h}_T^{S,N}$ for tissue *T*, exposure mode, *S*, and radionuclide, *N*, were computed on the basis of the evaluated organ absorbed dose rate coefficients for monoenergetic photons and electrons and the nuclear decay data contained in *Publication 107* (ICRP, 2008) using the following expression:

$$\dot{h}_T^{S,N} = \sum_R w_R \left[\sum_i Y_{R,i}(E_i) \cdot \dot{d}_{T,R}^{S}(E_i) + \int_0^\infty Y_R(E) \cdot \dot{d}_{T,R}^{S}(E) dE \right] \quad (7.1)$$

where *R* indicates the radiation type, and w_R the radiation weighting factor of the radiation type *R*. The summation outside a major bracket means an extension over the radiations (i.e. photons and electrons) emitted from a radionuclide *N*. $Y_{R,i}$ is the yield of *i*-th radiation of type *R* having discrete energy E_i emitted by a nuclear decay of the radionuclide and $\dot{d}_{T,R}^{S}(E_i)$ is the organ absorbed dose rate coefficient at the energy E_i for tissue, *T*, radiation type, *R*, and exposure mode, *S*, as provided in Section 5. The first term within the major bracket sums over all radiations emitted with discrete energies by the nuclear decay. $Y_R(E)$ and $\dot{d}_{T,R}^{S}(E)$ in the integration of the second term is the yield and absorbed dose rate coefficient, respectively, at the energy *E* within a continuous energy spectra of beta emission.

(141) Interpolations of absorbed dose were carried out in a log-linear space. As the coefficients for monoenergetic radiations obtained by Monte Carlo calculations addressed only photons and electrons of 0.01 MeV and higher energy, the values at energies less than 0.01 MeV are set to zero.

(142) Radionuclide specific organ equivalent dose rate coefficients were evaluated for 1252 radionuclides of 97 elements compiled in *Publication 107* (ICRP, 2008) distributed in soil, air, and water, and are given in tabular form in the electronic supplement accompanying this report. In the electronic supplement a summary information, on the nuclear transformation of radionuclides can be also found (ICRP, 2008).

7.2. Coefficients for effective dose rates

(143) As per definition of effective dose in *Publication 103* (ICRP, 2007), the organ equivalent doses of both male and female phantoms were used for its computation. Radionuclide specific effective dose rate coefficients were derived from the radionuclide specific organ equivalent dose rate coefficients discussed above. The effective dose rate coefficient ($\dot{e}^{S,N}$) for exposure mode (*S*) and radionuclide (*N*) was computed as follows:

$$\dot{e}^{S,N} = \sum_T w_T \left[\frac{\dot{h}_T^{S,N,M} + \dot{h}_T^{S,N,F}}{2} \right] (7.2)$$

where w_T represents the tissue weighting factor, $\dot{h}_T^{S,N,M}$ and $\dot{h}_T^{S,N,F}$ are the equivalent dose rate coefficients to the tissue (*T*) of male and female, respectively, for radionuclide (*N*) in exposure mode (*S*).

(144) The radionuclide specific effective dose rate coefficients are given in tabular form in folders ‘Soil contamination’, ‘Air submersion’ and ‘Water immersion’ of the electronic supplement accompanying this report.

7.3. Coefficients for air kerma and ambient dose equivalent rate

(145) Radionuclide specific coefficients of air kerma rate ($\dot{k}_a^{S,N}$) and ambient dose equivalent rate ($\dot{h}^*(10)^{S,N}$) were evaluated for photon sources in the soil contamination and air submersion geometries using the monoenergetic data and nuclear decay data as follows:

$$\dot{k}_a^{S,N} = \sum_i Y_{\mathrm{photon},i}\,(E_i) \cdot \dot{k}_a^S(E_i) \qquad (7.3)$$

$$\dot{h}^*(10)^{S,N} = \sum_i Y_{\mathrm{photon},i}(E_i) \cdot \dot{h}^*(10)^S(E_i) \qquad (7.4)$$

where $Y_{\mathrm{photon},i}$ is the yield of *i*-th photon emitted from nuclear decay of a nuclide (*N*) with energy (E_i), and $\dot{k}_a^S$ and $\dot{h}^*(10)^S$ indicate the air kerma and ambient dose equivalent rate coefficients, respectively, at the energy of E_i.

(146) The values of $\dot{k}_a^S(E_i)$ and $h^{\cdot} * (10)^S(E_i)$ were determined from the data of monoenergetic photon sources by log-log interpolation.

(147) The radionuclide specific air kerma and ambient dose equivalent rate coefficients for soil contamination and air submersion are listed under folders ‘Soil contamination’ and ‘Air submersion’ of the electronic supplement of this publication, together with the data for radionuclide specific effective dose rates. Similarly to the radionuclide-specific organ equivalent dose rate coefficients, these air kerma and ambient dose equivalent rates for radionuclides were estimated by using the ICRP *Publication 107* decay data (ICRP, 2008) summerised in the electronic supplement of this publication.

8. APPLICATION OF DOSE RATE COEFFICIENTS

8.1. Application of dose rate coefficients to various depth profiles of radionuclides in soil

8.1.1. Planar sources in specific depths

(148) As described in Section 5.1, the dose rate coefficients for soil contamination were evaluated for planar sources at five source depths expressed in mean free path (mfp) of the photons in soil (i.e. 0.0, 0.2, 1.0, 2.5, and 4.0 mfp). The source depth can be expressed as mass per unit area in units of g cm^{-2}, which is independent of the soil density since absorption is depending only on the mass thickness. The mean free path of photons depends on photon energy. For instance, a specific source depth of 3.0 g cm^{-2} corresponds to 72.3, 0.54, and 0.14 mfp of 0.01, 0.1, and 2.0 MeV photons in the soil, respectively. Dose rate coefficients for monoenergetic photons emitted from a planar source at a specific depth (in g cm^{-2}) can be reconstructed from the data at corresponding mean free path using a log-log interpolation. Tables 8.1 to 8.3 tabulate the effective dose rate coefficients for planar sources at specific depths of 0.5, 3.0, and 10.0 g cm^{-2} for monoenergetic photons. The depth of 0.5 g cm^{-2} approximates well the ground roughness, whereas 3.0 g cm^{-2} is the typical deposition depth for radiocaesium and 10.0 g cm^{-2} is roughly the maximum depth where caesium has been observed.

8.1.2. Volumetric sources

(149) Measurements around the Fukushima area (Matsuda et al., 2015) revealed that the depth profile of radionuclides in soil changes over time due to terrestrial ecosystems. Calculating dose rate coefficients for each depth profile is not practical, therefore a method to obtain dose rate coefficients for volumetric sources having arbitrary depth profiles is proposed. Note that the depth profile of volumetric sources indicates the vertical distribution of the activity concentration along the depth in the soil, whereas the horizontal distribution is assumed to be uniform.

(150) Dose rate coefficients for volumetric sources having any arbitrary depth profile can be obtained using the data for planar sources in depths given in unit of g cm^{-2}, and a weighted-integral method as described by Satoh et al (Satoh et al., 2015, 2017). The weighted-integral method describes a depth profile in the soil with weights, $w(\zeta)$, regarding a radioactivity concentration distributed along a depth, ζ, described in g cm^{-2} and it is applicable to any depth profile e.g. exponential, Gaussian or uniform. Note that $w(\zeta)$ expresses the depth profile of the radioactivity concentration as a relative value to those activities at other depths without providing the absolute values.

(151) The coefficients for a volumetric source, $\dot{h}_{\mathrm{v}}$, are derived as follows:

$$\dot{h}_{\mathrm{v}} = \frac{1}{W}\int_{\zeta_1}^{\zeta_2} \dot{h}_{\mathrm{p}}(\zeta)\cdot w(\zeta)\,d\zeta$$

$$W = \int_{\zeta_1}^{\zeta_2} w(\zeta)\,d\zeta \qquad (8.1)$$

where $\dot{h}_{\mathrm{p}}(\zeta)$ is the dose rate coefficient for a planar source located at a depth ζ, ζ_1 and ζ_2 are the minimum and maximum depths of the volumetric source in the soil, respectively and W is the total weight in that depth profile.

(152) Matsuda et al. (2015) reported that the depth profiles of radioactive caesium in soil observed in the Fukushima area after the accident in 2011 are fitted with an exponential function using the equation of weight $w(\zeta)$ as follows:

$$w(\zeta) = \alpha \cdot \exp(-\frac{\zeta}{\beta}) \qquad (8.2)$$

where the factor α indicates the weight at the surface of the ground, and the parameter β is the relaxation mass per unit area. The magnitude of β is an indication of the radionuclide penetration in the soil with large values of β indicating a deeper penetration. The unit of relaxation mass per unit area is g cm^{-2}.

(153) To examine the validity of the weighted-integral method, Satoh et al (2015) incorporated an exponentially distributed volumetric source of ^{137}Cs with β=1.0 into the PHITS code and directly calculated the energy spectrum and the effective dose rate. It was found that the reconstructed volumetric source was a good approximation of the source directly calculated via Monte Carlo methods.

(154) Tables 8.4 to 8.7 list the effective dose rate coefficients evaluated for each age, for monoenergetic photon sources and volumetric sources distributed with exponential profiles with β= 0.5, 1.0, 2.5, and 5.0 g cm^{-2}, respectively. Nuclide-specific organ equivalent and effective dose coefficients for these volumetric sources can be found in the electronic supplement.

Table 8.1. Effective dose rate, ambient dose equivalent rate and air kerma rate coefficients for monoenergetic photon sources distributed at a depth of 0.5 g cm^{-2} in the soil. Ambient dose equivalent rate and air kerma rate coefficients were estimated at 1 m above ground.

Energy	Effective dose rate coefficient						$\dot{h}^*(10)$	$\dot{k}_a$
(MeV)	(nSv h^{-1} Bq^{-1} m^2)							(nGy h^{-1} Bq^{-1} m^2)
	Adult	15 yr	10 yr	5 yr	1 yr	Newborn		
0.010	1.10E-12	1.01E-12	1.29E-12	1.51E-12	1.49E-12	2.04E-12	1.35E-12	1.64E-10
0.015	3.49E-08	3.77E-08	6.08E-08	5.99E-08	8.30E-08	1.22E-07	6.93E-07	2.52E-06
0.020	1.02E-06	1.19E-06	1.60E-06	1.86E-06	2.24E-06	3.23E-06	1.73E-05	2.82E-05
0.030	1.43E-05	1.62E-05	1.95E-05	2.51E-05	2.85E-05	3.98E-05	1.10E-04	1.01E-04
0.040	3.95E-05	4.44E-05	5.14E-05	6.36E-05	7.05E-05	8.61E-05	1.89E-04	1.34E-04
0.050	6.60E-05	7.36E-05	8.27E-05	9.90E-05	1.11E-04	1.28E-04	2.35E-04	1.46E-04
0.060	1.01E-04	1.10E-04	1.23E-04	1.42E-04	1.60E-04	1.80E-04	2.98E-04	1.76E-04
0.070	1.32E-04	1.43E-04	1.58E-04	1.79E-04	2.01E-04	2.23E-04	3.51E-04	2.04E-04
0.080	1.64E-04	1.77E-04	1.93E-04	2.16E-04	2.43E-04	2.67E-04	4.03E-04	2.36E-04
0.100	2.20E-04	2.36E-04	2.52E-04	2.80E-04	3.12E-04	3.45E-04	5.02E-04	3.00E-04
0.150	3.62E-04	3.81E-04	4.09E-04	4.56E-04	5.08E-04	5.61E-04	7.64E-04	4.96E-04
0.200	4.97E-04	5.27E-04	5.66E-04	6.32E-04	7.01E-04	7.82E-04	1.02E-03	6.94E-04
0.300	7.78E-04	8.21E-04	8.83E-04	9.84E-04	1.09E-03	1.22E-03	1.50E-03	1.10E-03
0.400	1.07E-03	1.12E-03	1.20E-03	1.34E-03	1.48E-03	1.67E-03	1.97E-03	1.50E-03
0.500	1.37E-03	1.41E-03	1.53E-03	1.68E-03	1.87E-03	2.11E-03	2.43E-03	1.90E-03
0.600	1.66E-03	1.71E-03	1.84E-03	2.02E-03	2.25E-03	2.54E-03	2.86E-03	2.29E-03
0.800	2.21E-03	2.29E-03	2.45E-03	2.67E-03	2.96E-03	3.34E-03	3.65E-03	2.99E-03
1.000	2.66E-03	2.76E-03	2.95E-03	3.20E-03	3.51E-03	3.95E-03	4.19E-03	3.52E-03
1.500	3.97E-03	4.07E-03	4.35E-03	4.69E-03	5.10E-03	5.69E-03	5.88E-03	5.06E-03
2.000	5.18E-03	5.31E-03	5.66E-03	6.08E-03	6.57E-03	7.30E-03	7.45E-03	6.50E-03
3.000	7.35E-03	7.57E-03	8.03E-03	8.60E-03	9.18E-03	1.01E-02	1.03E-02	9.08E-03
4.000	9.26E-03	9.59E-03	1.01E-02	1.08E-02	1.14E-02	1.26E-02	1.27E-02	1.14E-02
5.000	1.10E-02	1.14E-02	1.20E-02	1.28E-02	1.34E-02	1.47E-02	1.49E-02	1.34E-02
6.000	1.27E-02	1.32E-02	1.38E-02	1.47E-02	1.53E-02	1.66E-02	1.69E-02	1.53E-02
8.000	1.63E-02	1.66E-02	1.75E-02	1.86E-02	1.92E-02	2.07E-02	2.10E-02	1.94E-02

Table 8.2. Effective dose rate, ambient dose equivalent rate and air kerma rate coefficients for monoenergetic photon sources distributed at a depth of 3.0 g cm^{-2} in the soil. Ambient dose equivalent rate and air kerma rate coefficients were estimated at 1 m above ground.

Energy	Effective dose rate coefficient						$\dot{h}^*(10)$	$\dot{k}_a$
(MeV)	($nSv\ h^{-1}\ Bq^{-1}\ m^2$)							($nGy\ h^{-1}\ Bq^{-1}\ m^2$)
	Adult	15 yr	10 yr	5 yr	1 yr	Newborn		
0.010	0.00E+00	0.00E+00	0.00E+00	0.00E+00	0.00E+00	0.00E+00	0.00E+00	0.00E+00
0.015	0.00E+00	0.00E+00	0.00E+00	0.00E+00	0.00E+00	0.00E+00	0.00E+00	0.00E+00
0.020	2.37E-11	2.53E-11	3.42E-11	4.18E-11	4.20E-11	6.70E-11	5.48E-10	8.98E-10
0.030	2.31E-07	2.65E-07	3.00E-07	3.94E-07	4.61E-07	6.23E-07	2.29E-06	2.12E-06
0.040	3.81E-06	4.19E-06	4.69E-06	5.84E-06	6.66E-06	8.32E-06	2.11E-05	1.51E-05
0.050	1.31E-05	1.44E-05	1.59E-05	1.88E-05	2.14E-05	2.51E-05	5.26E-05	3.32E-05
0.060	2.70E-05	2.97E-05	3.28E-05	3.78E-05	4.09E-05	4.67E-05	9.04E-05	5.41E-05
0.070	4.32E-05	4.71E-05	5.17E-05	5.83E-05	6.29E-05	6.92E-05	1.28E-04	7.54E-05
0.080	6.14E-05	6.64E-05	7.22E-05	8.02E-05	8.69E-05	9.34E-05	1.68E-04	9.89E-05
0.100	9.44E-05	1.01E-04	1.07E-04	1.19E-04	1.27E-04	1.35E-04	2.35E-04	1.40E-04
0.150	1.72E-04	1.80E-04	1.92E-04	2.10E-04	2.24E-04	2.38E-04	3.90E-04	2.49E-04
0.200	2.39E-04	2.54E-04	2.71E-04	2.97E-04	3.14E-04	3.37E-04	5.30E-04	3.53E-04
0.300	3.71E-04	3.92E-04	4.20E-04	4.58E-04	4.82E-04	5.21E-04	7.78E-04	5.51E-04
0.400	5.01E-04	5.22E-04	5.57E-04	6.07E-04	6.36E-04	6.89E-04	9.93E-04	7.33E-04
0.500	6.27E-04	6.44E-04	6.85E-04	7.46E-04	7.81E-04	8.45E-04	1.18E-03	9.02E-04
0.600	7.49E-04	7.64E-04	8.10E-04	8.79E-04	9.20E-04	9.96E-04	1.36E-03	1.06E-03
0.800	9.73E-04	1.01E-03	1.07E-03	1.15E-03	1.21E-03	1.31E-03	1.73E-03	1.39E-03
1.000	1.18E-03	1.23E-03	1.29E-03	1.38E-03	1.45E-03	1.57E-03	1.99E-03	1.64E-03
1.500	1.97E-03	2.03E-03	2.14E-03	2.27E-03	2.40E-03	2.61E-03	3.09E-03	2.62E-03
2.000	2.77E-03	2.84E-03	3.00E-03	3.18E-03	3.37E-03	3.66E-03	4.17E-03	3.59E-03
3.000	4.30E-03	4.42E-03	4.64E-03	4.93E-03	5.19E-03	5.63E-03	6.19E-03	5.44E-03
4.000	5.70E-03	5.87E-03	6.14E-03	6.51E-03	6.81E-03	7.38E-03	7.98E-03	7.09E-03
5.000	6.99E-03	7.21E-03	7.52E-03	7.96E-03	8.26E-03	8.92E-03	9.59E-03	8.58E-03
6.000	8.23E-03	8.48E-03	8.82E-03	9.33E-03	9.62E-03	1.03E-02	1.11E-02	1.00E-02
8.000	1.09E-02	1.11E-02	1.15E-02	1.22E-02	1.25E-02	1.33E-02	1.41E-02	1.30E-02

Table 8.3 Effective dose rate, ambient dose equivalent rate and air kerma rate coefficients for monoenergetic photon sources distributed at a depth of 10.0 g cm^{-2} in the soil. Ambient dose equivalent rate and air kerma rate coefficients were estimated at 1 m above ground.

Energy	Effective dose rate coefficient						$\dot{h}^{*}(10)$	$\dot{k}_a$
(MeV)	(nSv h^{-1} Bq^{-1} m^{2})							(nGy h^{-1} Bq^{-1} m^{2})
	Adult	15 yr	10 yr	5 yr	1 yr	Newborn		
0.010	0.00E+00	0.00E+00	0.00E+00	0.00E+00	0.00E+00	0.00E+00	0.00E+00	0.00E+00
0.015	0.00E+00	0.00E+00	0.00E+00	0.00E+00	0.00E+00	0.00E+00	0.00E+00	0.00E+00
0.020	0.00E+00	0.00E+00	0.00E+00	0.00E+00	0.00E+00	0.00E+00	0.00E+00	0.00E+00
0.030	1.36E-11	1.75E-11	1.80E-11	2.10E-11	2.48E-11	3.29E-11	1.94E-10	1.81E-10
0.040	2.48E-08	3.02E-08	3.14E-08	3.88E-08	4.90E-08	5.65E-08	1.74E-07	1.23E-07
0.050	5.19E-07	5.84E-07	6.45E-07	7.71E-07	8.77E-07	1.03E-06	2.47E-06	1.58E-06
0.060	2.43E-06	2.66E-06	2.91E-06	3.42E-06	3.73E-06	4.26E-06	9.18E-06	5.51E-06
0.070	5.59E-06	6.05E-06	6.59E-06	7.59E-06	8.12E-06	9.15E-06	1.84E-05	1.09E-05
0.080	1.06E-05	1.15E-05	1.24E-05	1.41E-05	1.50E-05	1.65E-05	3.18E-05	1.88E-05
0.100	2.22E-05	2.38E-05	2.55E-05	2.86E-05	3.04E-05	3.26E-05	6.10E-05	3.62E-05
0.150	5.31E-05	5.65E-05	6.00E-05	6.61E-05	7.06E-05	7.45E-05	1.32E-04	8.30E-05
0.200	8.35E-05	8.85E-05	9.40E-05	1.03E-04	1.09E-04	1.16E-04	2.00E-04	1.30E-04
0.300	1.44E-04	1.51E-04	1.61E-04	1.76E-04	1.84E-04	1.96E-04	3.26E-04	2.23E-04
0.400	2.03E-04	2.12E-04	2.26E-04	2.46E-04	2.56E-04	2.75E-04	4.40E-04	3.14E-04
0.500	2.65E-04	2.75E-04	2.93E-04	3.18E-04	3.31E-04	3.57E-04	5.50E-04	4.06E-04
0.600	3.26E-04	3.37E-04	3.59E-04	3.89E-04	4.05E-04	4.38E-04	6.51E-04	4.95E-04
0.800	4.47E-04	4.65E-04	4.93E-04	5.30E-04	5.56E-04	6.01E-04	8.49E-04	6.66E-04
1.000	5.70E-04	5.92E-04	6.24E-04	6.70E-04	7.02E-04	7.56E-04	1.03E-03	8.25E-04
1.500	9.20E-04	9.50E-04	9.97E-04	1.06E-03	1.11E-03	1.20E-03	1.53E-03	1.28E-03
2.000	1.27E-03	1.30E-03	1.36E-03	1.45E-03	1.51E-03	1.62E-03	2.01E-03	1.71E-03
3.000	1.90E-03	1.95E-03	2.03E-03	2.14E-03	2.23E-03	2.38E-03	2.87E-03	2.49E-03
4.000	2.44E-03	2.51E-03	2.59E-03	2.73E-03	2.82E-03	2.99E-03	3.56E-03	3.13E-03
5.000	2.91E-03	2.98E-03	3.07E-03	3.22E-03	3.30E-03	3.49E-03	4.12E-03	3.65E-03
6.000	3.34E-03	3.42E-03	3.50E-03	3.67E-03	3.74E-03	3.93E-03	4.62E-03	4.12E-03
8.000	4.29E-03	4.39E-03	4.45E-03	4.67E-03	4.68E-03	4.91E-03	5.70E-03	5.17E-03

Table 8.4. Effective dose rate, ambient dose equivalent rate and air kerma rate coefficients for monoenergetic photon sources distributed exponentially from the ground surface to 100.0 g cm^{-2} with β=0.5 g cm^{-2} in the soil. Ambient dose equivalent rate and air kerma rate coefficients were estimated at 1 m above ground.

Energy	Effective dose rate coefficient						$\dot{h}^*(10)$	$\dot{k}_a$
(MeV)	(nSv h^{-1} Bq^{-1} m^2)							(nGy h^{-1} Bq^{-1} m^2)
	Adult	15 yr	10 yr	5 yr	1 yr	Newborn		
0.010	1.00E-06	9.67E-07	1.32E-06	1.68E-06	3.18E-06	6.06E-06	9.88E-07	1.20E-04
0.015	3.37E-06	3.78E-06	5.97E-06	7.37E-06	1.09E-05	2.13E-05	5.06E-05	1.93E-04
0.020	9.01E-06	1.06E-05	1.43E-05	1.98E-05	2.50E-05	4.36E-05	1.33E-04	2.16E-04
0.030	3.26E-05	3.73E-05	4.51E-05	6.25E-05	7.65E-05	1.12E-04	2.31E-04	2.11E-04
0.040	6.24E-05	7.07E-05	8.19E-05	1.06E-04	1.25E-04	1.61E-04	2.84E-04	1.99E-04
0.050	9.06E-05	1.02E-04	1.17E-04	1.41E-04	1.67E-04	1.99E-04	3.15E-04	1.94E-04
0.060	1.23E-04	1.35E-04	1.51E-04	1.76E-04	2.05E-04	2.37E-04	3.58E-04	2.11E-04
0.070	1.53E-04	1.66E-04	1.83E-04	2.10E-04	2.41E-04	2.72E-04	3.98E-04	2.32E-04
0.080	1.82E-04	1.97E-04	2.16E-04	2.44E-04	2.78E-04	3.09E-04	4.42E-04	2.59E-04
0.100	2.39E-04	2.56E-04	2.74E-04	3.06E-04	3.46E-04	3.86E-04	5.38E-04	3.22E-04
0.150	3.84E-04	4.04E-04	4.35E-04	4.86E-04	5.46E-04	6.07E-04	8.03E-04	5.22E-04
0.200	5.23E-04	5.55E-04	5.95E-04	6.68E-04	7.45E-04	8.36E-04	1.06E-03	7.26E-04
0.300	8.13E-04	8.57E-04	9.22E-04	1.03E-03	1.15E-03	1.30E-03	1.56E-03	1.14E-03
0.400	1.11E-03	1.16E-03	1.25E-03	1.39E-03	1.55E-03	1.76E-03	2.04E-03	1.55E-03
0.500	1.42E-03	1.47E-03	1.59E-03	1.75E-03	1.95E-03	2.21E-03	2.51E-03	1.96E-03
0.600	1.72E-03	1.77E-03	1.91E-03	2.10E-03	2.34E-03	2.65E-03	2.95E-03	2.36E-03
0.800	2.28E-03	2.36E-03	2.52E-03	2.76E-03	3.06E-03	3.47E-03	3.75E-03	3.08E-03
1.000	2.73E-03	2.84E-03	3.04E-03	3.29E-03	3.63E-03	4.08E-03	4.30E-03	3.61E-03
1.500	4.06E-03	4.16E-03	4.45E-03	4.80E-03	5.23E-03	5.84E-03	6.00E-03	5.16E-03
2.000	5.28E-03	5.41E-03	5.78E-03	6.21E-03	6.71E-03	7.46E-03	7.58E-03	6.61E-03
3.000	7.46E-03	7.69E-03	8.17E-03	8.74E-03	9.33E-03	1.03E-02	1.04E-02	9.22E-03
4.000	9.39E-03	9.72E-03	1.03E-02	1.10E-02	1.16E-02	1.28E-02	1.29E-02	1.15E-02
5.000	1.12E-02	1.16E-02	1.22E-02	1.30E-02	1.36E-02	1.49E-02	1.51E-02	1.36E-02
6.000	1.28E-02	1.33E-02	1.40E-02	1.49E-02	1.55E-02	1.69E-02	1.71E-02	1.55E-02
8.000	1.64E-02	1.68E-02	1.77E-02	1.89E-02	1.94E-02	2.09E-02	2.12E-02	1.96E-02

Table 8.5. Effective dose rate, ambient dose equivalent rate and air kerma rate coefficients for monoenergetic photon sources distributed exponentially from the ground surface to 100.0 g cm^{-2} with β=1.0 g cm^{-2} in the soil. Ambient dose equivalent rate and air kerma rate coefficients were estimated at 1 m above ground.

Energy	Effective dose rate coefficient						$\dot{h}^{*}(10)$	$\dot{k}_{a}$
(MeV)	(nSv h^{-1} Bq^{-1} m^{2})							(nGy h^{-1} Bq^{-1} m^{2})
	Adult	15 yr	10 yr	5 yr	1 yr	Newborn		
0.010	5.27E-07	5.10E-07	6.96E-07	8.86E-07	1.67E-06	3.19E-06	5.21E-07	6.33E-05
0.015	1.83E-06	2.05E-06	3.25E-06	3.99E-06	5.91E-06	1.15E-05	2.76E-05	1.05E-04
0.020	5.13E-06	6.06E-06	8.12E-06	1.12E-05	1.41E-05	2.45E-05	7.61E-05	1.24E-04
0.030	2.07E-05	2.36E-05	2.85E-05	3.92E-05	4.77E-05	6.95E-05	1.49E-04	1.36E-04
0.040	4.37E-05	4.94E-05	5.71E-05	7.31E-05	8.59E-05	1.10E-04	2.02E-04	1.42E-04
0.050	6.81E-05	7.64E-05	8.70E-05	1.05E-04	1.23E-04	1.45E-04	2.40E-04	1.48E-04
0.060	9.66E-05	1.06E-04	1.18E-04	1.38E-04	1.58E-04	1.81E-04	2.86E-04	1.68E-04
0.070	1.23E-04	1.34E-04	1.48E-04	1.68E-04	1.91E-04	2.13E-04	3.27E-04	1.90E-04
0.080	1.50E-04	1.62E-04	1.77E-04	1.99E-04	2.24E-04	2.47E-04	3.70E-04	2.17E-04
0.100	2.01E-04	2.14E-04	2.29E-04	2.55E-04	2.85E-04	3.15E-04	4.59E-04	2.74E-04
0.150	3.30E-04	3.47E-04	3.72E-04	4.15E-04	4.60E-04	5.08E-04	6.99E-04	4.53E-04
0.200	4.51E-04	4.79E-04	5.13E-04	5.73E-04	6.33E-04	7.05E-04	9.28E-04	6.33E-04
0.300	7.03E-04	7.41E-04	7.97E-04	8.87E-04	9.78E-04	1.10E-03	1.37E-03	9.94E-04
0.400	9.64E-04	1.00E-03	1.08E-03	1.20E-03	1.32E-03	1.49E-03	1.79E-03	1.35E-03
0.500	1.23E-03	1.27E-03	1.37E-03	1.51E-03	1.67E-03	1.88E-03	2.20E-03	1.71E-03
0.600	1.50E-03	1.54E-03	1.66E-03	1.82E-03	2.01E-03	2.26E-03	2.59E-03	2.07E-03
0.800	1.99E-03	2.06E-03	2.21E-03	2.41E-03	2.65E-03	2.99E-03	3.31E-03	2.71E-03
1.000	2.40E-03	2.50E-03	2.67E-03	2.89E-03	3.16E-03	3.55E-03	3.82E-03	3.20E-03
1.500	3.63E-03	3.72E-03	3.97E-03	4.27E-03	4.63E-03	5.16E-03	5.40E-03	4.63E-03
2.000	4.76E-03	4.88E-03	5.20E-03	5.57E-03	6.01E-03	6.67E-03	6.87E-03	5.99E-03
3.000	6.81E-03	7.01E-03	7.43E-03	7.95E-03	8.47E-03	9.34E-03	9.54E-03	8.44E-03
4.000	8.63E-03	8.93E-03	9.42E-03	1.00E-02	1.06E-02	1.16E-02	1.19E-02	1.06E-02
5.000	1.03E-02	1.07E-02	1.12E-02	1.20E-02	1.25E-02	1.37E-02	1.39E-02	1.25E-02
6.000	1.19E-02	1.23E-02	1.29E-02	1.38E-02	1.43E-02	1.55E-02	1.59E-02	1.44E-02
8.000	1.53E-02	1.56E-02	1.65E-02	1.75E-02	1.80E-02	1.94E-02	1.98E-02	1.82E-02

Table 8.6. Effective dose rate, ambient dose equivalent rate and air kerma rate coefficients for monoenergetic photon sources distributed exponentially from the ground surface to 100.0 g cm^{-2} with β=2.5 g cm^{-2} in the soil. Ambient dose equivalent rate and air kerma rate coefficients were estimated at 1 m above ground.

Energy	Effective dose rate coefficient						$\dot{h}^{*}(10)$	$\dot{k}_a$
(MeV)	(nSv h^{-1} Bq^{-1} m^{2})							(nGy h^{-1} Bq^{-1} m^{2})
	Adult	15 yr	10 yr	5 yr	1 yr	Newborn		
0.010	2.18E-07	2.11E-07	2.88E-07	3.66E-07	6.91E-07	1.32E-06	2.15E-07	2.62E-05
0.015	7.73E-07	8.66E-07	1.37E-06	1.68E-06	2.49E-06	4.84E-06	1.17E-05	4.44E-05
0.020	2.24E-06	2.64E-06	3.54E-06	4.88E-06	6.13E-06	1.06E-05	3.34E-05	5.43E-05
0.030	9.96E-06	1.14E-05	1.37E-05	1.87E-05	2.27E-05	3.28E-05	7.26E-05	6.66E-05
0.040	2.37E-05	2.67E-05	3.08E-05	3.92E-05	4.57E-05	5.79E-05	1.12E-04	7.86E-05
0.050	4.08E-05	4.56E-05	5.16E-05	6.21E-05	7.19E-05	8.48E-05	1.47E-04	9.09E-05
0.060	6.17E-05	6.77E-05	7.53E-05	8.75E-05	9.90E-05	1.13E-04	1.87E-04	1.10E-04
0.070	8.22E-05	8.92E-05	9.82E-05	1.11E-04	1.25E-04	1.39E-04	2.23E-04	1.30E-04
0.080	1.03E-04	1.12E-04	1.22E-04	1.36E-04	1.52E-04	1.66E-04	2.62E-04	1.54E-04
0.100	1.44E-04	1.54E-04	1.64E-04	1.82E-04	2.01E-04	2.19E-04	3.38E-04	2.02E-04
0.150	2.45E-04	2.58E-04	2.76E-04	3.06E-04	3.35E-04	3.66E-04	5.32E-04	3.43E-04
0.200	3.39E-04	3.59E-04	3.85E-04	4.27E-04	4.66E-04	5.12E-04	7.14E-04	4.83E-04
0.300	5.30E-04	5.59E-04	6.00E-04	6.64E-04	7.23E-04	8.01E-04	1.06E-03	7.61E-04
0.400	7.27E-04	7.58E-04	8.14E-04	8.97E-04	9.76E-04	1.09E-03	1.38E-03	1.04E-03
0.500	9.30E-04	9.60E-04	1.03E-03	1.13E-03	1.23E-03	1.37E-03	1.69E-03	1.31E-03
0.600	1.13E-03	1.16E-03	1.25E-03	1.36E-03	1.49E-03	1.66E-03	1.99E-03	1.58E-03
0.800	1.51E-03	1.57E-03	1.67E-03	1.81E-03	1.98E-03	2.21E-03	2.56E-03	2.08E-03
1.000	1.84E-03	1.91E-03	2.03E-03	2.19E-03	2.37E-03	2.64E-03	2.97E-03	2.47E-03
1.500	2.82E-03	2.89E-03	3.07E-03	3.30E-03	3.55E-03	3.93E-03	4.26E-03	3.64E-03
2.000	3.74E-03	3.84E-03	4.07E-03	4.36E-03	4.67E-03	5.15E-03	5.48E-03	4.76E-03
3.000	5.45E-03	5.61E-03	5.93E-03	6.32E-03	6.71E-03	7.36E-03	7.71E-03	6.80E-03
4.000	7.00E-03	7.23E-03	7.60E-03	8.09E-03	8.51E-03	9.30E-03	9.69E-03	8.63E-03
5.000	8.42E-03	8.71E-03	9.13E-03	9.70E-03	1.01E-02	1.10E-02	1.15E-02	1.03E-02
6.000	9.78E-03	1.01E-02	1.06E-02	1.12E-02	1.16E-02	1.26E-02	1.31E-02	1.19E-02
8.000	1.27E-02	1.30E-02	1.36E-02	1.44E-02	1.48E-02	1.59E-02	1.65E-02	1.52E-02

Table 8.7. Effective dose rate, ambient dose equivalent rate and air kerma rate coefficients for monoenergetic photon sources distributed exponentially from the ground surface to 100.0 g cm^{-2} with β=5.0 g cm^{-2} in the soil. Ambient dose equivalent rate and air kerma rate coefficients were estimated at 1 m above ground.

Energy (MeV)	Effective dose rate coefficient (nSv h^{-1} Bq^{-1} m^{2})						$\dot{h}^{*}(10)$	$\dot{k}_{a}$ (nGy h^{-1} Bq^{-1} m^{2})
	Adult	15 yr	10 yr	5 yr	1 yr	Newborn		
0.010	1.10E-07	1.06E-07	1.45E-07	1.85E-07	3.49E-07	6.66E-07	1.09E-07	1.32E-05
0.015	3.94E-07	4.41E-07	6.97E-07	8.56E-07	1.27E-06	2.46E-06	5.95E-06	2.26E-05
0.020	1.16E-06	1.36E-06	1.83E-06	2.51E-06	3.16E-06	5.44E-06	1.72E-05	2.81E-05
0.030	5.36E-06	6.12E-06	7.37E-06	1.01E-05	1.21E-05	1.76E-05	3.94E-05	3.61E-05
0.040	1.36E-05	1.53E-05	1.76E-05	2.24E-05	2.60E-05	3.29E-05	6.49E-05	4.57E-05
0.050	2.49E-05	2.78E-05	3.14E-05	3.77E-05	4.35E-05	5.12E-05	9.09E-05	5.64E-05
0.060	3.95E-05	4.33E-05	4.82E-05	5.59E-05	6.28E-05	7.14E-05	1.22E-04	7.20E-05
0.070	5.44E-05	5.91E-05	6.50E-05	7.36E-05	8.20E-05	9.08E-05	1.51E-04	8.81E-05
0.080	7.04E-05	7.61E-05	8.29E-05	9.25E-05	1.03E-04	1.12E-04	1.82E-04	1.07E-04
0.100	1.02E-04	1.08E-04	1.16E-04	1.29E-04	1.41E-04	1.53E-04	2.43E-04	1.45E-04
0.150	1.79E-04	1.89E-04	2.02E-04	2.23E-04	2.43E-04	2.63E-04	3.96E-04	2.54E-04
0.200	2.51E-04	2.66E-04	2.85E-04	3.15E-04	3.41E-04	3.72E-04	5.40E-04	3.63E-04
0.300	3.97E-04	4.19E-04	4.49E-04	4.95E-04	5.34E-04	5.87E-04	8.08E-04	5.77E-04
0.400	5.46E-04	5.69E-04	6.10E-04	6.71E-04	7.23E-04	7.98E-04	1.06E-03	7.87E-04
0.500	6.99E-04	7.21E-04	7.73E-04	8.46E-04	9.12E-04	1.01E-03	1.30E-03	9.96E-04
0.600	8.50E-04	8.72E-04	9.34E-04	1.02E-03	1.10E-03	1.22E-03	1.52E-03	1.20E-03
0.800	1.14E-03	1.18E-03	1.26E-03	1.36E-03	1.47E-03	1.63E-03	1.96E-03	1.59E-03
1.000	1.39E-03	1.44E-03	1.53E-03	1.65E-03	1.77E-03	1.96E-03	2.28E-03	1.89E-03
1.500	2.15E-03	2.21E-03	2.34E-03	2.51E-03	2.69E-03	2.95E-03	3.30E-03	2.81E-03
2.000	2.87E-03	2.95E-03	3.12E-03	3.34E-03	3.56E-03	3.90E-03	4.27E-03	3.70E-03
3.000	4.24E-03	4.36E-03	4.59E-03	4.88E-03	5.17E-03	5.64E-03	6.06E-03	5.33E-03
4.000	5.48E-03	5.65E-03	5.93E-03	6.29E-03	6.60E-03	7.18E-03	7.65E-03	6.80E-03
5.000	6.62E-03	6.83E-03	7.14E-03	7.57E-03	7.88E-03	8.52E-03	9.06E-03	8.12E-03
6.000	7.70E-03	7.95E-03	8.29E-03	8.77E-03	9.06E-03	9.77E-03	1.04E-02	9.36E-03
8.000	1.01E-02	1.03E-02	1.07E-02	1.14E-02	1.16E-02	1.24E-02	1.31E-02	1.20E-02

8.2. Radionuclide decay chain

(155) In this *publication*, external dose rate coefficients are evaluated for 1252 radionuclides of 97 elements compiled in *Publication 107* (ICRP, 2008). Table XX (see electronic supplement of this publication) summarises nuclear decay characteristics of each radionuclide. The nuclide-specific dose rate coefficients appearing on the electronic supplement are based on the radiations emitted by the indicated radionuclide and do not include consideration of the radiations emitted by radioactive decay products. For each radionuclide, the radioactive decay products, if formed, are identified in Table 1 of the Electronic Supplement.

(156) Dose rate coefficients for a radionuclide and its decay products should be combined after consideration of the equations describing production and decay of daughter radionuclides over time, and differences in environmental behaviour of the parent and daughter nuclides. Such consideration is required for evaluation of the effective dose rate at a specified time and the effective dose integrated over a specified period.

(157) The serial transformation by radioactive decay of each member of a radioactive series is described by the Bateman equations (Bateman, 1910; ICRP, 1959; Skrable et al., 1974) and the following equations developed by Eckerman and Ryman (1993). Assume that at time zero, the concentration of the parent nuclide on the surface of the ground is A_1^0 (Bq m^{-2}) and that the effective dose, E for an exposure period of one year is to be estimated. The contribution to effective dose from nuclear transformation of the parent nuclide is given by

$$E = \dot{e}_{E,1}^{gs} \frac{A_1^0}{\lambda_1}\left(1 - e^{-\lambda_1 T}\right), \tag{8.3}$$

where $\dot{e}_{E,1}^{gs}$ denotes the effective dose rate coefficient from ground surface exposure for nuclide 1 (Sv s^{-1} Bq^{-1} m^{2}), λ_1 is the decay constant, in inverse seconds, for nuclide 1 (λ = 0.6931 .../$T_{1/2}$), and T is the exposure period of one year or 3.15×10^7 s.

(158) Using the Bateman equations, the activity at time t of chain members i, i = 1, 2, ..., can be expressed as

$$A_i(t) = A_1^0 \prod_{j=1}^{i-1} f_{j,j+1}\,\lambda_j \sum_{j=1}^{i} \frac{e^{-\lambda_j t}}{\prod_{\substack{k=1 \\ k\neq j}}^{i}(\lambda_k - \lambda_j)} \quad , \tag{8.4}$$

where

$$\prod_{i=1}^{n} a_i = \begin{cases} a_1 \times a_2 \cdots a_n, & \text{if } n \geq 1 \\ 1, & \text{if } n = 0 \end{cases} \quad ,$$

and $f_{j,j+1}$ denotes the fraction of the nuclear transformations of chain member (j) forming member ($j+1$).

(159) The effective dose associated with an exposure period of duration (T), following a contamination event at t = 0 that results in a ground surface concentration of A_1^0, is

$$E = A_1^0 \sum_{i=1}^{n} \dot{e}_{E,i}^{gs} \prod_{j=1}^{i-1} f_{j,j+1}\, \lambda_j \sum_{j=1}^{i} \frac{e^{-\lambda_j T}}{\prod_{\substack{k=1\\k\neq j}}^{i} (\lambda_k - \lambda_j)} \quad , \tag{8.5}$$

where $\dot{e}_{E,i}^{gs}$ denotes the effective dose rate coefficient for ground surface exposure to nuclide (i), and all other factors are as defined above. If the parent radionuclide is long-lived relative to the decay products, then at times T such that $\lambda_i T > 5$, i = 2 to n, E can be estimated as

$$E = A_1^0 \frac{1 - e^{-\lambda_1 T}}{\lambda_1} \sum_{i=1}^{n} \dot{e}_{E,i}^{gs} \prod_{j=1}^{i-1} f_{j,j+1} \quad , \tag{8.6}$$

(160) Under these conditions the activity of the decay products is in secular equilibrium with the parent's activity. For example, application of Eq. (8.6) to ^{137}Cs and its ^{137m}Ba decay product would yield

$$E = A_{\mathrm{Cs-137}}^0 \frac{1 - e^{-\lambda_{\mathrm{Cs-137}} t}}{\lambda_{\mathrm{Cs-137}}} \left(\dot{e}_{E,\mathrm{Cs-137}}^{gs} + 0.944\, \dot{e}_{E,\mathrm{Ba-137m}}^{gs} \right) \quad , \tag{8.7}$$

where 0.944 is the fraction of the ^{137}Cs nuclear transformations forming ^{137m}Ba. If the decay products are not short-lived relative to the parent, then it is necessary to evaluate Eq. (8.5).

(161) In many instances, the mathematical models describing the fate of radionuclides in the environment (e.g. their dispersion of following release to the atmosphere) include an evaluation of the ingrowth of each radioactive decay product. The information of Table 1 (Electronic Supplement) should be useful to those implementing such models.

8.3. Relationship between radioactivity in soil, effective dose, ambient dose equivalent and personal dose equivalent

(162) Operational quantities were originally developed for the protection of occupationally exposed workers. The use of the operational quantities has been extended to monitoring of radiation exposure of the public from natural and artificial environmental sources of radiation. One of the applications is radiation monitoring in contaminated environment by radionuclides released from nuclear facilities by an accident.

(163) After the Fukushima Daiichi Nuclear Power Plant accident in 2011, a large-scale national environmental monitoring program was carried out, and comprehensive data including radioactivity in soil and ambient dose equivalent rate, $\dot{H}^*(10)$, were collected (NRA, 2012). In addition, many municipalities in Fukushima prefecture started individual external dose monitoring for residents living in contaminated areas. The individual monitoring of external exposure is performed using a personal dosimeter worn on the body.

(164) The personal dosimeters indicate personal dose equivalent, $H_\mathrm{p}(10)$. The relationship between effective dose, E, ambient dose equivalent, $H^*(10)$ and $H_\mathrm{p}(10)$ has been studied for workers in *Publication 74* (ICRP, 1996b) and *Publication 116* (ICRP, 2010) for idealised exposure conditions. In routine calibrations, personal dosimeters on a phantom are exposed in the reference direction, i.e. at 0°. The condition simulates antero-posterior (AP) geometry where workers face to radiation sources and are exposed to radiations from

front to back. In the AP geometry, $H_{\mathrm{p}}(10)$ provides a conservative estimate regarding E for photon energies up to 10 MeV. However, the radiation fields originated by large-scale environmental contamination are multidirectional photon fields and their characteristics are different from those in the AP geometry. Determining whether E can be properly assessed using the personal dosimeters, which have been calibrated for the reference direction, in the radiation field of the contaminated environment is a matter of great concern to ensure proper protection of the public.

(165) Satoh et al. (2017) investigated the relation of E, $H^*(10)$ and $H_{\mathrm{p}}(10)$ in radiation fields originated from ^{134}Cs and ^{137}Cs in soil. In this study, E and $H_{\mathrm{p}}(10)$ monitored by a personal dosemeter worn on the body, have been calculated using the paediatric (newborns; 1-year-old, 5-year-old, 10-year-old, and 15-year-old children) and adult phantoms by radiation transport techniques for planar sources of ^{134}Cs and ^{137}Cs distributed uniformly in various depths in soil. The study indicates the quantity $H_{\mathrm{p}}(10)$ provides a good estimate for E in a contaminated environment and does not exceed $H^*(10)$ values at a height of 1 m above the ground.

8.4. Comparison with new operational quantities for external radiation proposed by ICRU

(166) The operational quantities for external exposure in use at the time of compilation of this report, were defined in the 1980s and have been implemented into legal metrology worldwide since. Nevertheless, the existing system has some limitations (Bartlett and Dietze, 2010; Endo, 2016), ICRU xx (in preparation) and informs on further improvements to consider changes in the fields of application, including the extension of radiation type and energy range (ICRP, 2007, 2010, 2016a; ICRU, 2010). Ideally, the determination of an operational quantity should give a value that is a close estimate of the value of the protection quantity.

(167) The ICRU Report Committee 26 [ICRU Report xx (in preparation)] has examined the rationale for the operational quantities, considering updated definitions of protection quantities by ICRP (ICRP, 2007, 2010). They subsequently investigated a set of alternative definitions for operational quantities. ICRU recommends a redefinition of the operational quantities using coefficients that are based on protection quantities (Endo, 2016). Thus, consideration was given to define new quantities by the value of particle fluence (a radiometric quantity) at the point of interest, multiplied by values of the conversion coefficients to the protection quantities. This approach is justified because the reference values of the conversion coefficients for the protection quantities are available (ICRP, 2010). This change would avoid the use of different phantoms (anthropomorphic phantoms vs. ICRU sphere or slab) and different forms of dose weighting for radiation quality (radiation weighting factor vs quality factor) between the protection quantities and the operational quantities.

(168) In the proposed definitions, the ambient dose H^*, at a point in a radiation field, is defined as the product of the particle energy fluence, Φ, at that point and a conversion coefficient, h, relating the particle energy fluence to the maximum value of the effective dose, E_{max}. The conversion coefficients are calculated for exposures of the whole-body of the ICRP adult reference phantoms (ICRP, 2009a) for broad idealised parallel beams of the radiation field incident in irradiation geometries along the antero-posterior (AP), postero-anterior (PA), left lateral (LLAT), right lateral (RLAT) axes, for 360° rotational (ROT) directions, fully

isotropic irradiation (ISO), superior hemisphere semi-isotropic irradiation (SS-ISO), and inferior hemisphere semi-isotropic irradiation (IS-ISO) fields.

(169) The ambient dose coefficients are given by $h_{E_{\max,i}}(\varepsilon) = E_{\max,i}(\varepsilon)/\Phi(\varepsilon)$, where the fluence values are those for the particle type, i, at the point of interest, at each energy, ε. For particles of type i:

$$H_i^* = \int h_{E_{\max,i}}(\varepsilon) \frac{\mathrm{d}\Phi_i(\varepsilon)}{\mathrm{d}\varepsilon}\, \mathrm{d}\varepsilon$$

where $\mathrm{d}\Phi_i(\varepsilon)/\mathrm{d}\varepsilon$ is the fluence of particles at that point with kinetic energies in the interval $\mathrm{d}\varepsilon$ around ε. The sum over all contributing particle types, i, is the quantity H^*:

$$H^* = \sum H_i^*$$

The unit of ambient dose is J kg^{-1}. The special name for the unit of ambient dose is sievert (Sv).

8.5. Application of dose rate coefficients for remediation planning

(170) The present *publication* provides radionuclide-specific dose rate coefficients for members of the public resulting from environmental external exposures. These dose rate coefficients could be utilised for planning of remediation from radioactive contamination of the environment. Remediation activities, including decontamination, reduce exposure of the public living in a contaminated area. A software has been developed to support decision-making and planning of remediation activities by optimisation of counter measures (Ulanovsky et al., 2011). The software addresses the annual effective dose of the population, and the dose rate coefficients given in this *Publication* are useful for this purpose.

(171) Estimation of dose reduction by decontamination for a specific situation requires among other factors, consideration of source size, inhomogeneity of source distribution, and decontamination factor. For that purpose, Satoh et al (2014) have developed a methodology and software to estimate the effects of decontamination and the dose reduction effect resulting from a decontamination scenario. To estimate the dose reduction for a specific contaminated site after decontamination measures, it is necessary to consider the inhomogeneity of the source distribution as well as the size of the source. This estimation requires a different approach than the one describes in this report and it is proposed by Satoh et al (2014).

(172) It is beyond the Task Group’s scope to address decontamination.

9. CONCLUSIONS

(173) This report provides age-dependent data sets of nuclide-specific reference effective and organ equivalent dose rate coefficients to be used for the assessment of external dose from environmental exposure to the public for selected idealized environmental conditions which are considered to be typical. These are exposure to contamination on or below the ground surface and at different depths (soil contamination); submersion in a contaminated atmospheric cloud (air submersion); and immersion in contaminated water (water immersion). In the first two scenarios, air-over-ground geometry and a human body standing up-right above the ground were assumed.

(174) ICRP establishes for the first time reference dose rate coefficients for exposure to environmental radionuclides. These were computed for the ICRP voxel-based adult male and female reference computational phantoms (ICRP, 2009a) as well as for the 10 ICRP reference paediatric phantoms representing the newborn, 1-year-old, 5-year-old, 10-year-old and 15-year-old reference male and female reference individuals (ICRP 2018, in preparation). Radiations considered include primary photons and electrons from environmentally dispersed radionuclides, scattered photons and electrons emitted within the environment, and bremsstrahlung photons produced via electron deceleration. The emitted electrons include those of beta decay (negatrons and positrons) and ejected orbital electrons due to internal conversion and Auger processes in the electron shell of the newly formed atom.

(175) Organ equivalent dose rates increase with decreasing age because of the reduced shielding effect of the smaller body and the closer vicinity of the source for ground contamination. It was found that the effective dose varies relatively largely between the newborn and a 1-year-old child. Effective dose rates for the reference 15-year adolescents are close to those computed for the reference adults.

(176) The ambient dose equivalent rates and air kerma rates have been computed and are given for both soil contamination and air submersion for the environmental geometries considered. These data enable interpretation of monitoring data relating effective doses rates to ambient dose equivalent rates or to air kerma rates. Ambient dose equivalent and air kerma rates were found to provide conservative estimates of effective dose rates for both the adult and the newborn (and thus for all ages).

(177) The expected applications of the dose rate coefficients are: (a) pre-accidental evaluations in order to predict the possible impacts to the public by postulated radiological accidents, (b) post-accidental evaluations to estimate doses in order to develop a radiological protection strategy for the exposed populace, (c) evaluations following discharge of radionuclides from nuclear and radioisotope facilities during routine operations, and (d) evaluations of naturally occurring radionuclides in the environment. The pre/post-accident analyses are performed typically by software packages (e.g. codes for severe accidents). The software predicts the dispersion, migration, and distribution of radionuclides in the environment. The dose rate coefficients of the present publication could thus be implemented within these codes.

(178) It should be noted that dose rate coefficients are calculated for idealised and hypothetical source geometries such as semi-infinite and uniform distributions, for reference phantoms wearing no clothing, and for an idealised, upright postures, even for the exposed newborn. As a result, they do not fully reflect actual exposures for any particular situation or exposed individual.

(179) External doses can be significantly lower indoors than outdoors due to the shielding effects of the building. This is taken into account through the use of a so-called location factor of 0.4-0.6 which accounts for structural shielding by building type (according to the country,

building material) and an assumed occupancy factor of 0.6 (i.e. approximately two thirds of the time per day spent indoors) which represents the fraction of time spent inside a house (IAEA, 2000a). This obviously can vary considerably according to the geographical distribution, profession and population habits. The present report presents dose coefficients rates for situations outside houses and does not attempt to address issues of shielding or population behaviour. The selection and application of suitable location and occupancy factors is left to the user (i.e. the legislative authority or the developer of emergency programs).

REFERENCES

Adams, K., 2000. Electron upgrade for MCNP4B. Report X-5-RN(U)-00-14, Los Alamos National Laboratory, Los Alamos, NM.

Agostinelli, S., Allison, J., Amako, K., et al., 2003. Geant4—a simulation toolkit. Nuclear Instruments and Methods in Physics Research Section A: Accelerators, Spectrometers, Detectors and Associated Equipment 506(3), 250-303.

Allison, J., Amako, K., Apostolakis, J., et al., 2016. Recent developments in Geant4. Nuclear Instruments and Methods in Physics Research Section A: Accelerators, Spectrometers, Detectors and Associated Equipment 835, 186-225.

Bartlett, D.T., Dietze, G., 2010. ICRU operational quantities. Radiat Prot Dosimetry 139(4), 475-6.

Bateman, H., 1910. The Transformation of the Electrodynamical Equations. Proceedings of the London Mathematical Society s2-8(1), 223-264.

Bellamy, M.B., Veinot, K.G., Hiller, M.M., et al., 2016. Effective Dose Rate Coefficients for Immersions in Radioactive Air and Water. Radiat. Prot. Dosim. 174(2), 275-276.

Bellamy, M.B., Dewji, S.A., Leggett, R.W., et al., 2018. External exposure to radionuclides in soil, air, water: external dose coefficients for general application. Federal Guidance Report 15, Oak Ridge National Laboratory, Oak Ridge, Tennessee 37831, United States Environmental Protection Agency, Washington DC 20460.

Berger, M., Coursey, J., Zucker, M., et al., 2005. ESTAR, PSTAR, and ASTAR: Computer Programs for Calculating Stopping-Power and Range Tables for Electrons, Protons, and Helium Ions (version 1.2.3). NIST Report U.S., National Institute of Standards and Technology, Gaithersburg, MD.

Berger, M.J., Hubbell, J.H., 1987. XCOM: photon cross sections on a personal computer. NBSIR 87-3597, National Bureau of Standards (former name of NIST), Gaithersburg, MD.

Bolch, W.E., Petoussi-Henss, N., Paquet, F., et al., 2016. ICRP dose coefficients: computational development and current status. Ann. ICRP 45(1_suppl), 156-177.

Bolch, W.E., …, in preparation.

Buesseler, K., Dai, M., Aoyama, M., et al., 2017. Fukushima Daiichi–Derived Radionuclides in the Ocean: Transport, Fate, and Impacts. Annual Review of Marine Science 9(1), 173-203.

Burson, Z.G., Profio, A.E., 1977. Structure shielding in reactor accidents. Health Phys. 33(4), 287-99.

Cassola, V.F., Milian, F.M., Kramer, R., et al., 2011. Standing adult human phantoms based on 10th, 50th and 90th mass and height percentiles of male and female Caucasian populations. Phys. Med. Biol. 56(13), 3749.

Chang, L.A., Simon, S.L., Jorgensen, T.J., et al., 2017. Dose coefficients for ICRP reference pediatric phantoms exposed to idealised external gamma fields. J. Radiol. Prot. 37(1), 127-146.

Cristy, M., Eckerman, K.F., 1987. Specific absorbed fractions of energy at various ages from internal photon sources, Part I-VII. ORNL Report TM-8381/V1-TM-8381/V7, Oak Ridge National Laboratory, Oak Ridge, TN.

Cullen, D., H. Hubbell, J., Kissel, L., 1997. EPDL97: the evaluated photo data library `97 version.

Dillman, L.T., 1974. Absorbed gamma dose rate for immersion in a semi-infinite radioactive cloud. Health Phys. 27(6), 543-588.

DOE, 1988. External dose-rate conversion factors for calculation of dose to the public. DOE/EH-0070, US Department of Energy, Washington D. C.

Eckerman, K.F., Ryman, C., 1993. External exposure to radionuclides in air, water, and soil. Federal Guidance Report 12, Oak Ridge National Laboratory, Oak Ridge, Tennessee 37831, United States Environmental Protection Agency, Washington DC 20460.

Endo, A., 2016. Operational quantities and new approach by ICRU. Ann. ICRP 45(1_suppl), 178-187.

European Commission Joint Research Centre, 2017. EURDEP (European Radiological Data Exchange Platform) http://eurdep.jrc.ec.europa.eu/Basic/Pages/Public/Home/Default.aspx.

Fritsch, F.N., Carlson, R.E., 1980. Monotone Piecewise Cubic Interpolation. SIAM Journal on Numerical Analysis 17(2), 238-246.

Han, E.Y., Bolch, W.E., Eckerman, K.F., 2006. Revisions to the ORNL series of adult and pediatric computational phantoms for use with the MIRD schema. Health Phys. 90(4), 337-356.

Hough, M., Johnson, P., Rajon, D., et al., 2011. An image-based skeletal dosimetry model for the ICRP reference adult male—internal electron sources. Phys. Med. Biol. 56(8), 2309-2346.

Hunt, J.G., da Silva, F.C., Mauricio, C.L., et al., 2004. The validation of organ dose calculations using voxel phantoms and Monte Carlo methods applied to point and water immersion sources. Radiat Prot Dosimetry 108(1), 85-89.

IAEA, 2000a. Calibration of Radiation Protection Monitoring Instruments. International Atomic Energy Agency, Vienna, Austria.

IAEA, 2000b. Generic procedures for assessment and response during a radiological emergency International Atomic Energy Agency, Vienna, Austria.

ICRP, 1959. Report of Committee II on Permissible Dose for Internal Radiation. ICRP Publication 2, Pergamon Press, Oxford, UK.

ICRP, 1990. Age-dependant Doses to Members of the Public from Intake of Radionuclides: Part 1. ICRP Publication 56, Pergamon Press, Oxford, UK. Ann. ICRP 20 (2).

ICRP, 1991. 1990 Recommendations of the International Commission on Radiological Protection. ICRP Publication 60, Pergamon Press, Oxford, UK. Ann. ICRP 21 (1-3).

ICRP, 1993. Age-dependent Doses to Members of the Public from Intake of Radionuclides: Part 2: Ingestion Dose Coefficients. ICRP Publication 67, Pergamon Press, Oxford, UK. Ann. ICRP 23(3-4).

ICRP, 1995a. Age-dependent Doses to Members of the Public from Intake of Radionuclides: Part 3: Ingestion Dose Coefficients. ICRP Publication 69, Pergamon Press, Oxford, UK. Ann. ICRP 25 (1).

ICRP, 1995b. Basic Anatomical and Physiological Data for use in Radiological Protection: The Skeleton. ICRP Publication 70, Pergamon Press, Oxford, UK. Ann. ICRP 25 (2).

ICRP, 1995c. Age-dependent Doses to Members of the Public from Intake of Radionuclides: Part 4: Inhalation Dose Coefficients. ICRP Publication 71, Pergamon Press, Oxford, UK. Ann. ICRP 25 (3-4).

ICRP, 1996a. Age-dependent Doses to Members of the Public from Intake of Radionuclides. Part 5: Compilation of Ingestion and Inhalation Dose Coefficients. ICRP Publication 72, Pergamon Press, Oxford, UK. Ann. ICRP 26 (1).

ICRP, 1996b. Conversion Coefficients for use in Radiological Protection against External Radiation. ICRP Publication 74, Pergamon Press, Oxford, UK. Ann. ICRP 26 (3/4).

ICRP, 2001. Doses to the Embryo and Fetus from Intakes of Radionuclides by the Mother. ICRP Publication 88, Pergamon Press, Oxford, UK. Ann. ICRP 31 (1-3).

ICRP, 2002. Basic Anatomical and Physiological Data for Use in Radiological Protection: Reference Values. ICRP Publication 89, Pergamon Press, Oxford, UK. Ann. ICRP 32 (3-4).

ICRP, 2004. Doses to Infants from Ingestion of Radionuclides in Mothers' Milk. ICPR Publication 95, Pergamon Press, Oxford, UK. Ann. ICRP 34 (3-4).

ICRP, 2006. Assessing Dose of the Representative Person for the Purpose of Radiation Protection of the Public and The Optimisation of Radiological Protection: Broading the Process. ICRP Publication 101, Elsevier, Oxford, UK. Ann. ICRP 36 (3).

ICRP, 2007. The 2007 Recommendations of the International Commission on Radiological Protection. ICRP Publication 103, Elsevier, Oxford, UK. Ann. ICRP 37 (2-4).

ICRP, 2008. Nuclear Decay Data for Dosimetric Calculations. ICRP Publication 107, International Commission on Radiological Protection, Oxford, UK. Ann. ICRP 38 (3).

ICRP, 2009a. Adult Reference Computational Phantoms. ICRP Publication 110, International Commission on Radiological Protection, Oxford, UK. Ann. ICRP 39 (2).

ICRP, 2009b. Application of the Commission's Recommendations to the Protection of People Living in Long-term Contaminated Areas After a Nuclear Accident or a Radiation Emergency. ICRP Publication 111, International Commission on Radiological Protection, Oxford, UK. Ann. ICRP 39 (3).

ICRP, 2010. Conversion Coefficients for Radiological Protection Quantities for External Radiation Exposures. ICRP Publication 116, International Commission on Radiological Protection, Oxford, UK. Ann. ICRP 40 (2-5).

ICRP, 2015. Occupational Intakes of Radionuclides: Part 1. ICRP Publication 130, International Commission on Radiological Protection. Ann. ICRP 44 (2).

ICRP, 2016a. The ICRP Computational Framework for Internal Dose Assessment for Reference Adults: Specific Absorbed Fractions. ICRP Publication 133, International Commission on Radiological Protection, Oxford, UK. Ann. ICRP 45 (2).

ICRP, 2016b. Occupational Intakes of Radionuclides: Part 2. ICRP Publication 134, International Commission on Radiological Protection, Ann. ICRP 45 (3/4).

ICRP, 2017. Occupational Intakes of Radionuclides: Part 3. ICRP Publication 137, International Commission on Radiological Protection, Ann. ICRP 46 (3/4).

ICRP, in preparation.

ICRU, 1985. Determination of dose equivalents resulting from external radiation sources. ICRU Report 39, International Commission on Radiation Units and Measurements, Bethesda, MD.

ICRU, 1988. Determination of dose equivalents from external radiation sources, Part 2. ICRU Report 43, International Commission on Radiation Units and Measurements, Bethesda, MD.

ICRU, 1992. Photon, electron, proton and neutron interaction data for body tissues. ICRU Report 46, International Commission on Radiation Units and Measurements, Bethesda, MD.

ICRU, 1993. Quantities and units in radiation protection dosimetry. ICRU Report 51, International Commission on Radiation Units and Measurements, Bethesda, MD.

ICRU, 1994. Gamma-ray spectrometry in the environment. ICRU Report 53, International Commission on Radiation Units and Measurements, Bethesda, MD.

ICRU, 2010. Reference Data for the Validation of Doses from Cosmic-Radiation Exposure of Aircraft Crew. ICRU Report 84 (prepared jointly with ICRP).

ICRU, 2014. Key Data For Ionizing-Radiation Dosimetry: Measurement Standards And Applications. ICRU Report. 90, Bethesda, MD.

ICRU, in preparation.

Jacob, P., Paretzke, H.G., 1986. Gamma-Ray Exposure from Contaminated Soil. Nuclear Science and Engineering 93(3), 248-261.

Jacob, P., Rosenbaum, H., Petoussi, N., et al., 1990. Calculation of organ doses from environmental gamma rays using human phantoms and Monte Carlo methods, Part II:

Radionuclides distributed in the air or deposited on the ground. GSF-Report 12/90, GSF - National Research Center for Environment and Health, Neuherberg, Germany.

Johnson, P., Lee, C., Johnson, K., et al., 2009. The influence of patient size on dose conversion coefficients: a hybrid phantom study for adult cardiac catheterization. Phys. Med. Biol. 54(12), 3613-3629.

Johnson, P.B., Bahadori, A.A., Eckerman, K.F., et al., 2011. Response functions for computing absorbed dose to skeletal tissues from photon irradiation - an update. Phys. Med. Biol. 56(8), 2347–2365.

Kawrakow, I., Mainegra-Hing, E., Rogers, D.W.O., et al., 2009. The EGSnrc code system: Monte Carlo simulation of electron and photon transport. PIRS Report 701, National Research Council of Canada (NRCC), Ottawa.

Kocher, D.C., Sjoreen, A.L., 1985. Dose-rate conversion factors for external exposure to photon emitters in soil. Health Phys. 48(2), 193-205.

Lee, C., Lodwick, D., Hurtado, J., et al., 2010. The UF family of reference hybrid phantoms for computational radiation dosimetry. Phys. Med. Biol. 55(2), 339-363.

Lee, C., Lamart, S., Moroz, B.E., 2013. Computational lymphatic node models in pediatric and adult hybrid phantoms for radiation dosimetry. Phys. Med. Biol. 58(5), N59-N82.

Lemercier, M., Gurriaran, R., Bouisset, P., et al., 2008. Specific activity to H*(10) conversion coefficients for in situ gamma spectrometry. Radiat. Prot. Dosim. 128(1), 83-89.

Lv, W., Hei, H., Liu, Q., 2017. The influence of physique on dose conversion coefficients for idealised external photon exposures: a comparison of doses for Chinese male phantoms with 10th, 50th and 90th percentile anthropometric parameters. J. Radiat. Res. (Tokyo). 1-8, 1.

Malins, A., Kurikami, H., Nakama, S., et al., 2016. Evaluation of ambient dose equivalent rates influenced by vertical and horizontal distribution of radioactive cesium in soil in Fukushima Prefecture. J. Environ. Radioact. 151(Part 1), 38-49.

Matsuda, N., Mikami, S., Shimoura, S., et al., 2015. Depth profiles of radioactive cesium in soil using a scraper plate over a wide area surrounding the Fukushima Dai-ichi Nuclear Power Plant, Japan. J. Environ. Radioact. 139, 427-434.

MCNP, X., 2003. Monte Carlo Team, MCNP—a general purpose Monte Carlo N-particle transport code, version 5. LA-UR-03-1987, Los Alamos National Laboratory, Los alamos, NM,

Mikami, S., Maeyama, T., Hoshide, Y., et al., 2015. Spatial distributions of radionuclides deposited onto ground soil around the Fukushima Dai-ichi Nuclear Power Plant and their temporal change until December 2012. J. Environ. Radioact. 139(Supplement C), 320-343.

Nelson, W.R., Hirayama, H., Rogers, D.W.O., 1985. The EGS4 code system. SLAC Report 265, Stanford Linear Accelerator Center, Stanford, CA.

Niita, K., Matsuda, N., Iwamoto, Y., et al., 2010. PHITS - Particle and Heavy Ion Transport code System, Version 2.23. Japan Atomic Energy Agency, Tokai-mura, Japan.

NRA, 2012. ….

Nuclear Regulation Authority Japan website, 2013. Practical measures for evacuees to return their homes. https://www.nsr.go.jp/data/000067234.pdf.

O' Brien, K., Sanna, R., 1976. Absorbed gamma dose rate for immersion in a semi-infinite radioactive cloud. Health Phys. 30(1), 71-78.

Pafundi, D.H., 2009. Image-based skeletal tissue and electron dosimetry models for the ICRP reference pediatric age series.

Pelowitz, D.B.e., 2011. MCNPX User's Manual, Version 2.7.0. LA-UR-11-02295, Los Alamos National Laboratory, Los Alamos, NM.

Pelowitz, D.B.e., 2013a. Initial MCNP6 Release Overview - MCNP6 version 1.0. LA-UR-13-22934, Los Alamos National Laboratory, Los Alamos, NM.

Pelowitz, D.B.e., 2013b. MCNP6 User's Manual. Version 1.0. LA-CP-13-000634, Los Alamos National Laboratory, Los Alamos, NM.

Perkins, S.T., Cullen, D.E., Seltzer, S.M., 1991. Tables and graphs of electron-interaction cross sections from 10 eV to 100 GeV derived from the LLNL Evaluated Electron Data Library (EEDL), Z = 1 to 100.

Perkins, S.T., …, 1997. …

Petoussi-Henss, N., Saito, K., 2009. Applications to environmental exposures, in: Xu, X.G., Eckerman, K.F. (Eds.), Handbook of anatomical models for radiation dosimetry. Taylor & Francis, Boca Raton, London, New York, pp. 413-424.

Petoussi-Henss, N., Schlattl, H., Zankl, M., et al., 2012. Organ doses from environmental exposures calculated using voxel phantoms of adults and children. Phys. Med. Biol. 57, 5679-5713.

Petoussi, N., Zankl, M., Saito, K., et al., 1989. Organ doses to adults and children from environmental gamma rays. In: Feldt, W. (Ed.), XVth Regional Congress of IRPA, Visby, Gotland, Sweden, The Radioecology of Natural and Artificial Radionuclides pp. 372-377.

Petoussi, N., Jacob, P., Zankl, M., et al., 1991. Organ doses for foetuses, babies, children and adults from environmental gamma rays. Radiat. Prot. Dosim. 37, 31-41.

Poston, J.W., Snyder, W.S., 1974. Model for exposure to a semi-infinite cloud of a photon emitter. Health Phys. 26(4), 287-347.

Saito, K., Petoussi, N., Zankl, M., et al., 1990. The calculation of organ doses from environmental gamma rays using human phantoms and Monte Carlo methods, Part I: Monoenergetic sources and natural radionuclides in the ground. GSF-Report 2/90, GSF - National Research Center for Environment and Health, Neuherberg, Germany.

Saito, K., Petoussi, N., Zankl, M., et al., 1991. Organ doses as a function of body weight for environmental gamma rays. Journal of Nuclear Science and Technology 28(7), 627-641.

Saito, K., Jacob, P., 1995. Gamma-ray fields in the air due to sources in the ground. Radiat. Prot. Dosim. 58, 29-45.

Saito, K., Petoussi-Henss, N., Zankl, M., 1998. Calculation of the effective dose and its variation from environmental gamma ray sources. Health Phys. 74(6), 698-706.

Saito, K., Ishigure, N., Petoussi-Henss, N., et al., 2012. Effective dose equivalent conversion coefficients for radionuclides exponentially distributed in the ground. Radiation Environmental Biophysics 51(4), 411-423.

Saito, K., Petoussi-Henss, N., 2014. Ambient dose equivalent conversion coefficients for radionuclides exponentially distributed in the ground. Journal of Nuclear Science and Technology,

Saito, K., Tanihata, I., Fujiwara, M., et al., 2015. Detailed deposition density maps constructed by large-scale soil sampling for gamma-ray emitting radioactive nuclides from the Fukushima Dai-ichi Nuclear Power Plant accident. J. Environ. Radioact. 139(Supplement C), 308-319.

Sato, T., Niita, K., Matsuda, N., et al., 2013. Particle and Heavy Ion Transport code System, PHITS, version 2.52. Journal of Nuclear Science and Technology 50, 913-923.

Sato, T., 2016. Evaluation of World Population-Weighted Effective Dose due to Cosmic Ray Exposure. Scientific Reports 6, 33932.

Satoh, D., Kojima, K., Oizumi, A., et al., 2014. Development of a calculation system for the estimation of decontamination effects. Journal of Nuclear Science and Technology 51(5), 656-670.

Satoh, D., Furuta, T., Takahashia, F., et al., 2015. Age-dependent dose conversion coefficients for external exposure to radioactive cesium in soil. Journal of Nuclear Science and Technology 53(1), 69-81.

Satoh, D., Furuta, T., Takahashi, F., et al., 2017. Simulation study of personal dose equivalent for external exposure to radioactive cesium distributed in soil. Journal of Nuclear Science and Technology 54(9), 1018-1027.

Schlattl, H., Zankl, M., Becker, J., et al., 2012. Dose conversion coefficients for paediatric CT examinations with automatic tube current modulation. Phys. Med. Biol. 57(20), 6309-6326.

Schümann, J., Paganetti, H., Shin, J., et al., 2012. Efficient voxel navigation for proton therapy dose calculation in TOPAS and Geant4. Phys. Med. Biol. 57(11), 3281-3293.

Skrable, K., French, C., Chabot, G., et al., 1974. A general equation for the kinetics of linear first order phenomena and suggested applications. Health Phys. 27(1), 155-7.

Ulanovsky, A., Jacob, P., Fesenko, S., et al., 2011. ReSCA: decision support tool for remediation planning after the Chernobyl accident. Radiat. Environ. Biophys. 50(1), 67-83.

UNSCEAR, 2000. Sources and effects of ionizing radiation. United Nations Scientific Committee on the Effects of Atomic Radiation, New York.

UNSCEAR, 2008. Sources and effects of ionizing radiation. United Nations Scientific Committee on the Effects of Atomic Radiation, New York.

UNSCEAR, 2013. Sources and effects of ionizing radiation. with Annex A - Levels and effects of radiation exposure due to the nuclear accident after the 2011 great east-Japan earthquake and tsunami. United Nations Scientific Committee on the Effects of Atomic Radiation, New York.

UNSCEAR, 2016. Sources and effects of ionizing radiation. United Nations Scientific Committee on the Effects of Atomic Radiation, New York.

Veinot, K.G., Eckerman, K.F., Bellamy, M.B., et al., 2017. Effective dose rate coefficients for exposure to contaminated soil. Radiat. Environ. Biophys. 56(3), 255-267.

Wayson, M.B., 2012. Computational Internal Dosimetry Methods as Applied to the University of Florida Series of Hybrid Phantoms. Biomedical Engineering, Dissertation, University of Florida.

White, M., 2003. A New Photoatomic Library Based on Data from ENDF/B-VI Release 8. Report LA-UR-03-1019, Los Alamos National Laboratory, Los Alamos, NM.

Xu, X.G., Eckerman, K.F. (Eds.), 2010. Handbook of anatomical models for radiation dosimetry, Taylor & Francis, Boca Raton, London, New York.

Yoo, S.J., Lee, J.-K., Kim, E.-H., et al., 2013a. Groundshine dose–rate conversion factors of soil contaminated to different depths. Radiat. Prot. Dosim. 157(3), 407-429.

Yoo, S.J., Jang, H.K., Lee, J.K., et al., 2013b. External dose-rate conversion factors of radionuclides for air submersion, ground surface contamination and water immersion based on the new ICRP dosimetric setting. Radiat Prot Dosimetry 156(1), 7-24.

Zankl, M., Wittmann, A., 2001. The adult male voxel model "Golem" segmented from whole body CT patient data. Radiat. Environ. Biophys. 40, 153-162.

Zankl, M., Fill, U., Petoussi-Henss, N., et al., 2002. Organ dose conversion coefficients for external photon irradiation of male and female voxel models. Phys. Med. Biol. 47(14), 2367-2385.

Zankl, M., Becker, J., Fill, U., et al., 2005. GSF male and female adult voxel models representing ICRP Reference Man - the present status. In: The Monte Carlo Method: Versatility Unbounded in a Dynamic Computing World, Chattanooga, TN.

ANNEX A. SKELETAL DOSIMETRY

(A 1) In this report, the radiation absorbed dose to two different target tissues were assessed in the computation of the effective dose: the haematopoietically active bone marrow (AM), and the skeletal endosteum (TM_{50}). The former target region is taken as the non-adipose regions of the bone marrow cavities within both spongiosa and medullary marrow cavities of the phantom skeleton, while the latter target region is taken to be total marrow localised with 50 µm of the bone trabeculae surfaces and along the interior surfaces of the long bone medullary cavities. As described in *Publications 110* and *116* (ICRP, 2009, 2010), the bone trabeculae and marrow cavities are tissue structures on the order of tens to hundreds of micrometres in thickness and extent, and thus cannot be fully modelled with the voxel resolution of either the reference adult or paediatric phantoms. Consequently, radiation absorbed dose, thus equivalent dose, to these two target tissues were determined employing the concept of the fluence-to-dose response function for photons as described and presented in Annex D of *Publication 116* (ICRP, 2010).

(A 2) It should be noted that for this report, energy deposition to the skeletal target tissues is almost exclusively by photons, either directly emitted from the environmental radionuclide sources (air, water, or soil), or indirectly by bremsstrahlung x-ray production by environmentally emitted beta particles and conversion/Auger electrons. In the rare instance that electron collisional kinetic energy is deposited within the marrow cavities of the phantom skeleton, radiation dose to spongiosa (or medullary marrow) is taken as a surrogate of the absorbed dose to either AM or TM_{50}.

(A 3) The fluence-to-dose response function ($\mathcal{R}$) for assessment of the bone-specific absorbed dose to skeletal tissues delivered by photons of energy (E) in bone site (x) is given as follows:

$$\mathcal{R}(r_T \leftarrow r_S, x, E) = \frac{D(r_T, x)}{\Phi(E, r_S, x)} \tag{A.1}$$

$$= \sum_r \frac{m(r,x)}{m(r_T,x)} \sum_i \int_0^\infty \phi(r_T \leftarrow r, T_i, x)(\mu_i/\rho)_{r,E} T_i \, n_r(T_i, E)\, dT_i \tag{A.2}$$

where

x is the index for the various bone sites within the phantom (upper femora, cranium, etc.); for the long bones, regions of spongiosa and the medullary cavities are considered as different bones sites;

r_T is the index for the target tissue for dose assessment (active marrow or endosteum);

r_S is the index for the source tissue in bone site x in which the photon fluence is scored (spongiosa or medullary marrow);

r is the index for the constituent tissues of source tissue r_S. For r_S = spongiosa, r is trabecular bone, active marrow, or inactive marrow;

E is the energy of the photon passing through and potentially interacting within skeletal tissue r_S of bone site x;

$m(r,x)$ is the mass of the constituent tissue r in bone site x;

$m(r_T,x)$ is the mass of the target tissue r_T in bone site x;

i is the index for the photon interaction type considered: photoelectric, Compton, pair production, or triplet production;

T_i is the kinetic energy of the secondary electron liberated in constituent tissue *r* by interaction type *i*;

$\phi(r_T \longleftarrow r, T_i, x)$ is the fraction of secondary electron kinetic energy T_i liberated in constituent tissue *r* of bone site *x* that is imparted to target tissue r_T in bone site *x*;

$(\mu_i/\rho)_{r,E}$ is the mass attenuation coefficient for photon interaction type *i*, in constitute tissue *r* at photon energy *E*; and

$n_r(T_i, E)dT_i$ denotes the number of secondary electrons of energy between T_i and $T_i + dT_i$ liberated in constituent tissue *r* by photon of energy *E* in interaction type *i*.

(A 4) As noted in Annex D of *Publication 116*, Eq. D.2 was evaluated as described by Johnson et al. (Johnson et al., 2011). Electron absorbed fraction data were obtained through Paired-Image Radiation Transport (PIRT) calculations using microCT images of 32 bones sites extracted from the skeleton of a 40-year-old male cadaver (Hough et al., 2011). Values of electron absorbed fractions in the bones of the reference paediatric phantoms were taken from the University of Florida doctoral dissertations of Pafundi (Pafundi, 2009) and Wayson (Wayson, 2012), as summarised in Bolch et al. (in preparation). MicroCT images of cadaveric newborn bones were used for radiation transport in the bones of the reference newborn phantom (Pafundi et al., 2009; Pafundi et al., 2010). Similarly, microCT images of cadaveric 18-year-old male bones were used in the construction of skeletal absorbed fractions for electrons in the reference 15-year-old phantom (Pafundi, 2009). Cadaveric bone samples were not available for the interior ages of the ICRP reference phantom series. Consequently, the linear path length distributions from the University of Leeds 1.7-year-old and 9-year-old cadavers were used respectively to assess electron absorbed fractions in the bones of the reference 1-year-old and 10-year-old phantoms (Beddoe, 1976). Values of skeletal electron absorbed fractions were then assessed via interpolation of the Leeds data to report values for the reference 5-year-old phantom (Pafundi, 2009). Charged particle equilibrium is typically established across bone sites at photon energies exceeding 200 keV, and thus in this report, values of the dose response function above that energy are taken as their corresponding spongiosa kerma coefficients.

(A 5) In this report, the absorbed dose in tissue (r_T) in bone site (x), $D(r_T, x)$ is thus determined as the integral of the product of the bone-specific energy-dependent photon fluence ($\Phi(E, r_S, x)$) and the bone-specific energy-dependent dose-response function ($\mathcal{R}(r_T \longleftarrow r_S, x, E)$):

$$D(r_T, x) = \int_{\mathrm{E}} \Phi(E, r_S, x)\, \mathcal{R}(r_T \longleftarrow r_S, x, E) dE. \tag{A.3}$$

While bone-specific absorbed dose to the skeletal tissues was computed in this study, the computation of the effective dose requires the skeletal-averaged absorbed dose to active marrow and to endosteum for each of the reference adult and paediatric phantoms. Accordingly, skeletal averaged dose is given as a mass-weighted average of the bone-site specific absorbed dose:

$$D_{skel}(r_T) = \sum_x \frac{m(r_T, x)}{m(r_T)} D(r_T, x), \tag{A.4}$$

where $m(r_T, x)$ is the bone-specific mass of the target tissue (r_T) in bone site (x), $m(r_T)$ is the total mass of target tissue (r_T) across the entire skeleton, and $D(r_T, x)$ is the bone-specific absorbed dose given by Equation A.3. Masses for the skeletal tissues are reported in *Publication 133* (ICRP, 2016) for the male and female reference adult phantoms, and in *Publication* XXX (ICRP, in preparation) for the series of male and female pediatric phantoms.

A.1. References

Beddoe, A.H., 1976. The microstructure of mammalian bone in relation to the dosimetry of bone-seeking radionuclides. Department of Medical Physics, University of Leeds.

Bolch, …, in preparation.

Hough, M., Johnson, P., Rajon, D., Jokisch, D., Lee, C. and Bolch, W., 2011. An image-based skeletal dosimetry model for the ICRP reference adult male-internal electron sources. Phys. Med. Biol. 56, 2309-2346.

ICRP, 2009. Adult Reference Computational Phantoms. ICRP Publication 110, International Commission on Radiological Protection, Oxford, UK. Ann. ICRP 39 (2).

ICRP, 2010. Conversion Coefficients for Radiological Protection Quantities for External Radiation Exposures. ICRP Publication 116, International Commission on Radiological Protection, Oxford, UK. Ann. ICRP 40 (2-5).

ICRP, 2016. The ICRP Computational Framework for Internal Dose Assessment for Reference Adults: Specific Absorbed Fractions. ICRP Publication 133, International Commission on Radiological Protection, Oxford, UK. Ann. ICRP 45 (2).

ICRP, in preparation.

Johnson, P.B., Bahadori, A.A., Eckerman, K.F., et al., 2011. Response functions for computing absorbed dose to skeletal tissues from photon irradiation - an update. Phys. Med. Biol. 56, 2347-2365.

Pafundi, D., Lee, C., Watchman, C., Bourke, V., et al., 2009. An image-based skeletal tissue model for the ICRP reference newborn. Phys. Med. Biol. 54, 4497-4531.

Pafundi, D., Rajon, D., Jokisch, D., et al., 2010. An image-based skeletal dosimetry model for the ICRP reference newborn--internal electron sources. Phys. Med. Biol. 55, 1785-1814.

Pafundi, D.H., 2009. Image-based skeletal tissue and electron dosimetry models for the ICRP reference pediatric age series. Biomedical Engineering, University of Florida, PhD Dissertation.

Wayson, M.B., 2012. Computational internal dosimetry methods as applied to the University of Florida series of hybrid phantoms. Biomedical Engineering, University of Florida, Dissertation.

ANNEX B. SKIN DOSIMETRY

(B 1) For environmental external exposures and dose to the skin, stochastic effects are relevant. In radiation protection, the mean value of the absorbed dose averaged over the specified organ, tissue or cells at risk is correlated with the detriment due to stochastic effects. The skin cells at radiogenic risk have been identified and the absorbed dose to these cells have been assigned a tissue weighting factor w_T=0.01 (ICRP, 2007). The skin dose contributing to the effective dose is the equivalent dose to the skin cells at risk averaged over the body.

(B 2) The skin cells at the most radiogenic risk are the basal cells, which are located between the epidermis and dermis of the skin. ICRP refers to a range of epidermal thickness of 20 to 100 µm, including the majority of body sites, but uses the nominal average value of 70 µm for general radiological protection purposes (ICRU, 1997; ICRP, 2010). *Publication 89* (ICRP, 2002) provides the reference thicknesses of the epidermis for different ages: 45 µm (newborn and 1-year-old and 5-year-old children), 50 µm (10-year-old children), 60 µm (15-year-old children) and 70 µm (adults). A range of 50 to 100 µm below the skin surface is considered to be an appropriate depth for the basal cell layer at radiogenic risks of most parts of the skin (ICRP, 2010).

(B 3) The extent to which the mean value of the skin dose is representative of the absorbed dose to the critical region of the skin, located at 50 to 100 µm depth, depends, for external irradiation, on the homogeneity of the exposure and on the range of the incident radiation. For gammas of energies relevant for environmental radionuclides, the assumption of the mean organ dose being representative of the dose to the 70 µm can be considered valid due to their rather homogeneous dose distribution within the skin. For weakly penetrating radiations (e.g. electrons) which could exhibit a significant dose gradient within the skin, this approach could be invalid, underestimating or overestimating the doses to the basal cell layer at risk.

(B 4) The skin of the voxel–based ICRP reference phantoms is represented as one voxel layer. The voxel thicknesses in both the male and female adult phantoms (2.137 mm and 1.775 mm, respectively) (ICRP, 2009) are larger than the reference skin thicknesses of 1.6 mm and 1.3 mm for the reference male and female, respectively (ICRP, 2002). Reference values for skin thickness in children have not be defined by ICRP, but can be derived for the reference paediatric phantoms using *Publication 89* data on: (1) skin mass and (2) body surface area provided in *Publication 89* (ICRP, 2002), and (3) a reference skin density from ICRU *Report 46* (ICRU, 1992). These derived skin thicknesses are shown in Table B.1. Note that these have not directly been used for the skin dosimetry of this publication, as the skin dose was scored at the sensitive layer (see paragraph B7), but are referred here for the sake of completeness.

(B 5) For electron skin dosimetry of the adult phantoms, the voxel representation of 2.1 or 1.7 mm (for male and female phantoms, respectively) could underestimate or overestimate the doses, depending on the electron energy, as would be shown in section B.1.1. In order to overcome this limitation, polygon mesh (PM) models were used: for the adult male and female phantoms, the skin models of the mesh-type ICRP adult reference phantoms were employed for the calculations. These phantoms are the exact counterparts of the ICRP phantoms and have the advantage that they can model small tissues below the voxel phantom resolution. More information on these phantoms can be found at (Kim et al., 2011, 2016, 2017; Yeom et al., 2013, 2016a,b; Nguyen et al., 2015).

(B 6) The mesh-type skin models of the adult phantoms were constructed by directly converting the skin models of the voxel-type ICRP adult reference phantoms to high-quality polygon-mesh (PM) format. The PM skin models include a 50-µm -thick radiosensitive layer located at a depth from 50 to 100 μm below the skin surface. Fig. B.1 shows a 3D representation of the adult male and female PM skin model. The masses of the adult PM skin models are in accordance with the reference values (male: 3300 g and female: 2300 g) (ICRP, 2002). The average thicknesses of the skin models are 1.69 mm and 1.33 mm for the adult male and female, respectively, which are in good agreement with the reference values (male: 1.6 mm and female: 1.3 mm). The inner space of the skin PM models is filled with the average soft tissue for adults, as specified by ICRU (1992), but has slightly modified densities (male: 1.024 g cm^3 and female: 1.010 g cm^3) in order to maintain the reference body weights of 73 (male) and 60 kg (female).

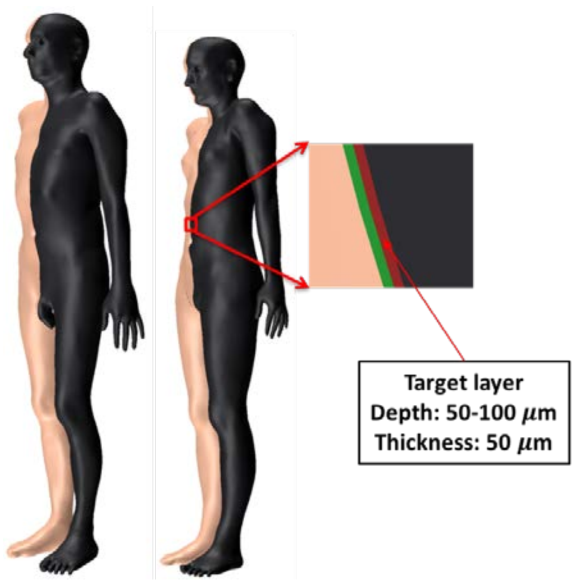

Fig. B.1. Representation of the adult male and female polygon mesh (PM) skin model. Red indicates the target sensitive layer of the skin; the beige colour indicates the exterior skin surface and the black colour represents the most inner skin surface. The dead skin layer between the exterior surface and the target layer is represented by the green colour, as viewed from the left side.

(B 7) For the paediatric phantoms, the mesh-type skin models were constructed from the outer surfaces of the NURBS-version of ICRP paediatric phantoms. (NURBS: Non-Uniform Rational B-Spline surfaces). These were the original phantoms from which the ICRP paediatric phantoms were derived (Lee et al., 2010). The NURBS-format outer surfaces were converted to the PM format via tessellation procedure (Piegl and Richard, 1995). The PM outer surfaces were then adjusted to match the total volumes of the ICRP paediatric phantoms. The outer surfaces were copied and their sizes were reduced to define the inner surface of the skin, matching the skin thicknesses to those (i.e. voxel sizes) of the ICRP paediatric phantoms. The inner space of the PM skin models was also filled with average soft tissue (ICRU, 1989) but with slightly modified densities to maintain the reference body weights. The outer surfaces were again copied to create two additional surfaces and reduce their sizes to define the target sensitive layer within the skin at depths of 50 μm and 100 μm. Table B.1 shows the average skin thickness, mass and density for the paediatric phantoms, as well as the of the sensitive layer of the skin.

Table B.1. Skin thickness, mass and density and mass of the sensitive layer of the skin of the pediatric phantoms.

Age and gender	Newborn Male/ Female	1 yr Male/ Female	5 yr Male/ Female	10 yr Male/ Female	15 yr Female	15 yr Male
Skin thickness (mm)	0.663	0.663	0.850	0.990	1.200	1.250
Skin mass (g)	139.9	291.5	665.5	1221.8	1978.7	2236.0
Mass of sensitive layer (g)	10.7	22.2	39.5	62.3	83.3	90.4
Skin density (g cm^{-3})	1.1	1.1	1.1	1.1	1.1	1.1

(B 8) The skin dose rate coefficients, shown in the electronic supplement of this report and used for the calculation of the effective dose rates, for both electron and photon beams and all geometries, were derived using the above PM phantom models and the Monte Carlo code GEANT4 (Agostinelli et al., 2003). For implementation, the skin phantoms in the PM format were converted to the tetrahedral-mesh (TM) format using the TetGen code (Si, 2006) and the converted TM phantoms were implemented in GEANT4 using the G4Tet class. Note that this tetrahedralization maintains the original shape of the PM phantoms but significantly improves computation speed (Yeom et al., 2014). The electromagnetic physics library of G4EmLivermorePhysics was used to transport photons and electrons (Wright, 2014). Considering the 50-µm-thick target layer, a secondary-range cut value of 1 µm was set for all particles.

(B 9) It should be noted that tissue reactions (sometimes referred to as deterministic effects) are correlated to the local skin dose i.e. dose averaged over 1 cm^2. The skin dose coefficients given in this report are not correlated with tissue reactions since they have been evaluated for the skin extended in the whole body.

B.1. Electron

(B 10) Fig. B.2 and B.3 show the skin dose rate coefficients for the adult female phantom and contamination at the surface of the soil and submersion to contaminated air, respectively, as a function of electron energy and as calculated using the original voxel phantom coupled to the PHITS transport code (Sato et al., 2013) and the polygon mesh phantom and the GEANT4 code (Agostinelli et al., 2003). As mentioned above, the resolution of the voxel phantom does not allow targeting the cells at risk (50 – 100 µm layer) but instead the dose is computed for the whole skin voxels. Using the mesh phantom, the estimation of the dose rate coefficients to the sensitive as well as to the entire skin is possible and these are shown in the Figures B.2 and B.3. It can be seen, that, the voxel approach overestimates the absorbed dose to the skin basal cell layer at photon energies below approximately 0.100 MeV and underestimates that same dose at energies between 0.100 and 1.5 MeV.

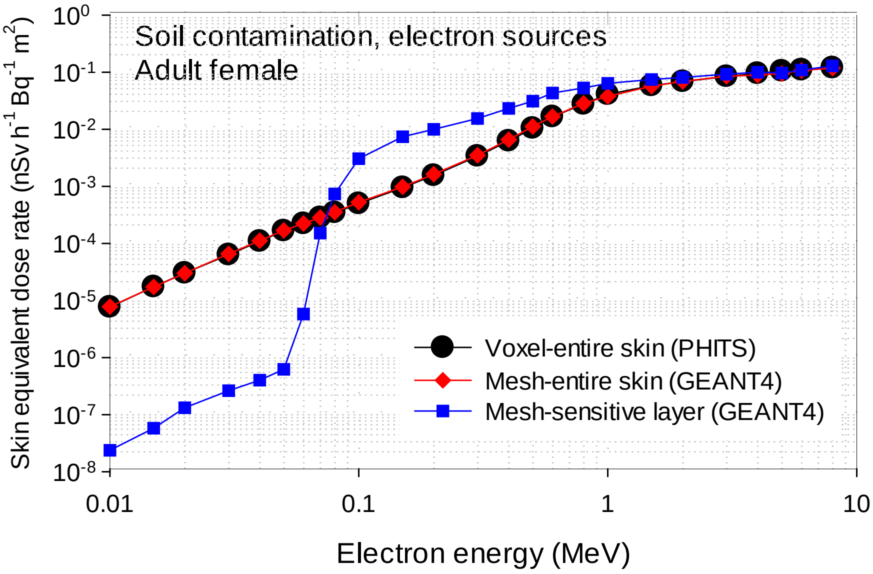

Fig. B.2. Skin dose coefficients for the adult female phantom and contamination at the surface of the soil, calculated using the original adult voxel phantom and the PHITS code, and the polygon adult mesh phantom and the GEANT4 code.

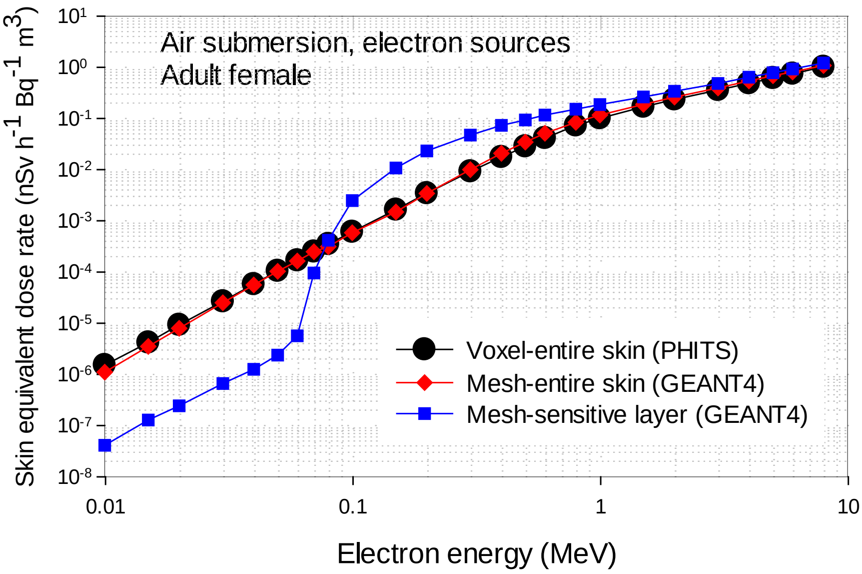

Fig. B.3. Skin dose coefficients for the adult female phantom and air submersion, calculated using the original adult voxel phantom and the PHITS code, and the polygon adult mesh phantom and the GEANT4 code.

(B 11) For electron simulations in the case of water immersion, excessive computation times are needed, because electrons emitted from the spherical water source of a diameter of 2 m hardly reach the phantom. To improve the efficiency of the calculation, a sampling source volume was limited from the skin surface to a certain distance in the water, depending on electron energies. For electrons with energies > 0.06 MeV, a distance, which is longer than the electron CSDA range in the water medium was used to limit the sampling source volume, because these primary electrons contribute to most of the energy deposited to the skin sensitive layer. On the other hand, for the lower energy electrons (≤ 0.06 MeV), a distance, which is longer than the mean free path of the photon at the initial electron energy, was considered because these electrons, having CSDA range less than 50 μm, cannot penetrate the 50-μm-thick dead layer to reach the skin sensitive layer and thus, only the secondary photons (e.g. bremsstrahlung photons) contribute to the dose.

(B 12) Figures B.4-B.6 show the skin dose rate coefficients evaluated for the sensitive layer of the skin using the mesh phantoms, for all ages and geometries considered. For the adult and 15-year-old phantoms, the male and female coefficients were averaged, whereas for the other paediatric ages a single skin model was used.

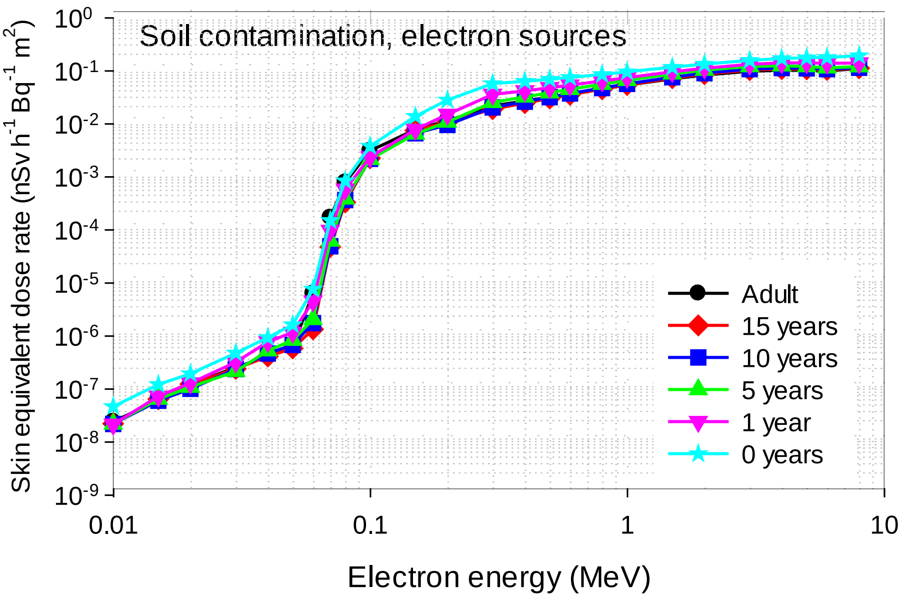

Fig. B.4. Skin dose rate coefficients for monoenergetic electron sources distributed at the surface as a ground plane source.

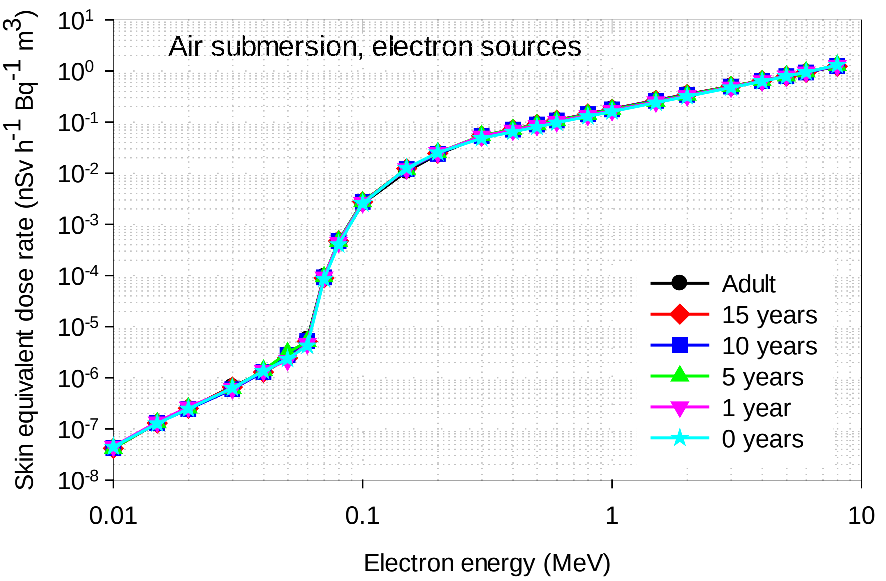

Fig. B.5. Skin dose rate coefficients for monoenergetic electron sources distributed uniformly in the atmosphere.

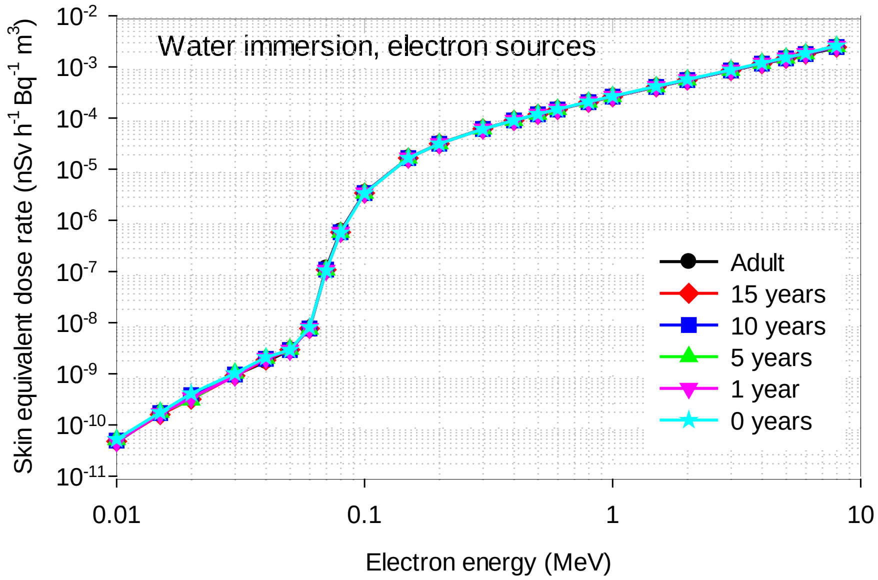

Fig. B.6. Skin dose rate coefficients for monoenergetic electron sources distributed uniformly in the water (i.e. water immersion).

B.2. Photons

(B 13) Figures B.7-B.9 show the skin dose rate coefficients for the adult male phantom, for monoenergetic photons and for the three environmental sources considered in this publication. For each plot, results are shown as calculated with the voxel-defined entire skin (i.e. averaged over all skin voxels), the entire skin as defined by the polygon meshes and the sensitive layer of the skin, also polygon-mesh defined and targeted between 50 and 100 µm below the skin surface. Similarly to the electron exposure simulations, the calculations for the voxel phantoms were performed with PHITS (Sato et al., 2013), whereas for the mesh phantoms GEANT4 was used (Agostinelli et al., 2003). It can be seen, that, although the differences of evaluated coefficients are not so pronounced as for electrons, the values of the coefficients for the sensitive layer are higher than those of the entire skin, at energies below approximately 0.1 MeV. This pattern is seen because low-energy photons tend to establish their maximum dose near the skin surface, as the dose rapidly decreases with depth by exponential attenuation. However, the values of the coefficients for the sensitive layer are lower for emitted energies above 0.2 to 0.6 MeV, (depending on the environmental source). Photons penetrate the sensitive layer skin region and deposit their energy partially, while they fully impart their energy to the voxel skin of the voxel phantoms, establishing the maximum dose at a depth deeper than what is seen within the sensitive layer.

(B 14) Moreover, it should be noted that, while the skin dose rate coefficients obtained with the adult voxel phantoms with PHITS and EGS4 agree well (see section 6.5), GEANT4 gives slightly larger values in the low energy region. This might result from the differences in the cut-off algorithm during particle transport within each code.

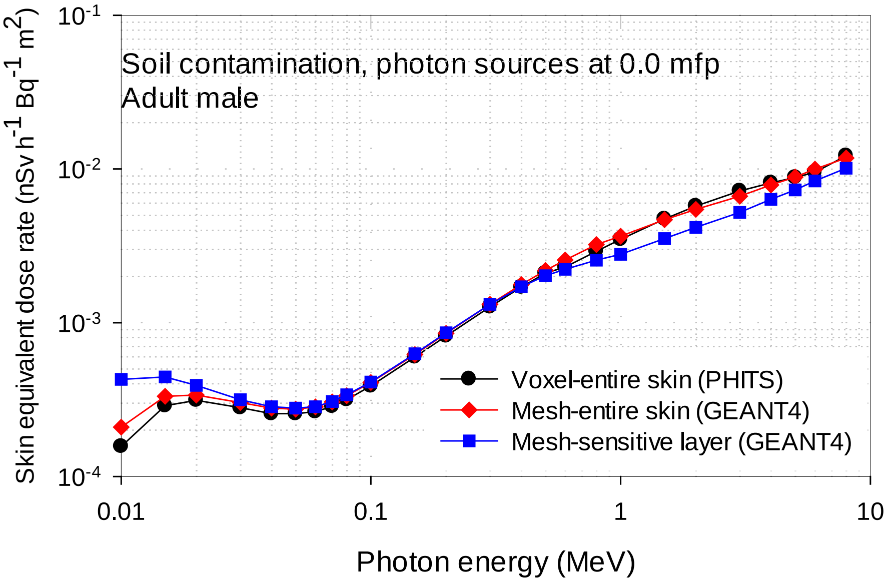

2795
2796
2797 Fig. B.7. Skin dose rate coefficients for monoenergetic photon sources distributed at the
2798 surface as a ground plane source.

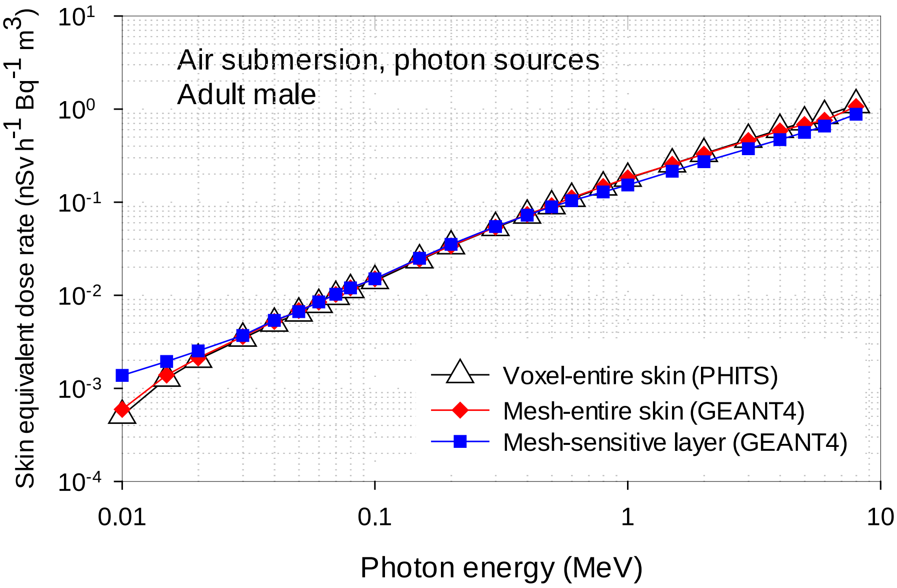

2799
2800 Fig. B.8. Skin dose rate coefficients for monoenergetic photon sources distributed uniformly
2801 in the atmosphere.
2802

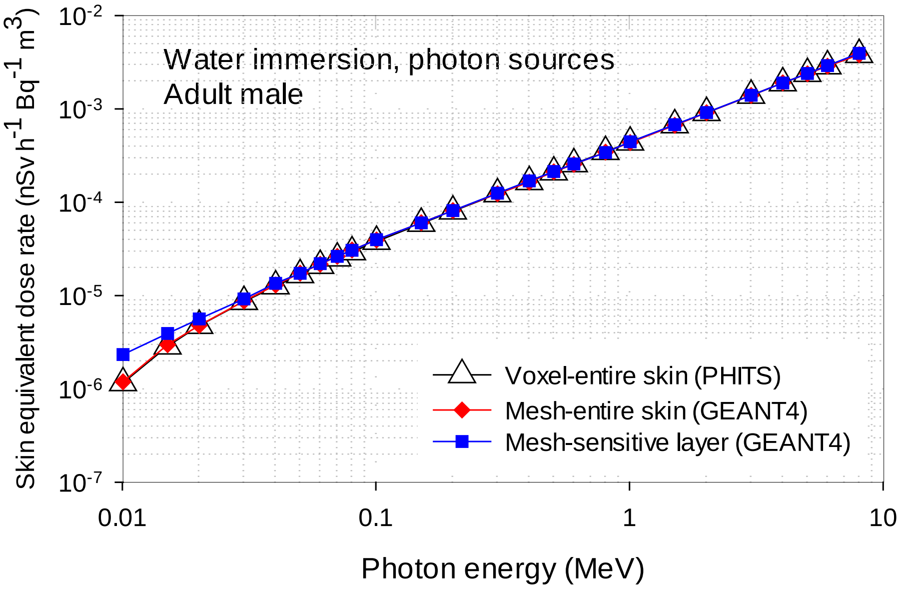

Fig. B.9. Skin dose rate coefficient for for monoenergetic photon sources and water immersion.

(B 15) Figures B.10-B.12 show the skin dose rate coefficients evaluated for the sensitive layer of the skin using the mesh phantoms, for all ages and environmental sources considered, for monoenergetic photons. As for the coefficients for electrons, for the adult and 15-year-old phantoms, the male and female coefficients were averaged, whereas for the other paediatric ages a single skin model was used. All skin dose rate coefficients, also for soil contamination at depths of 0.2-4 mfp in the soil, can be found in the electronic supplement.

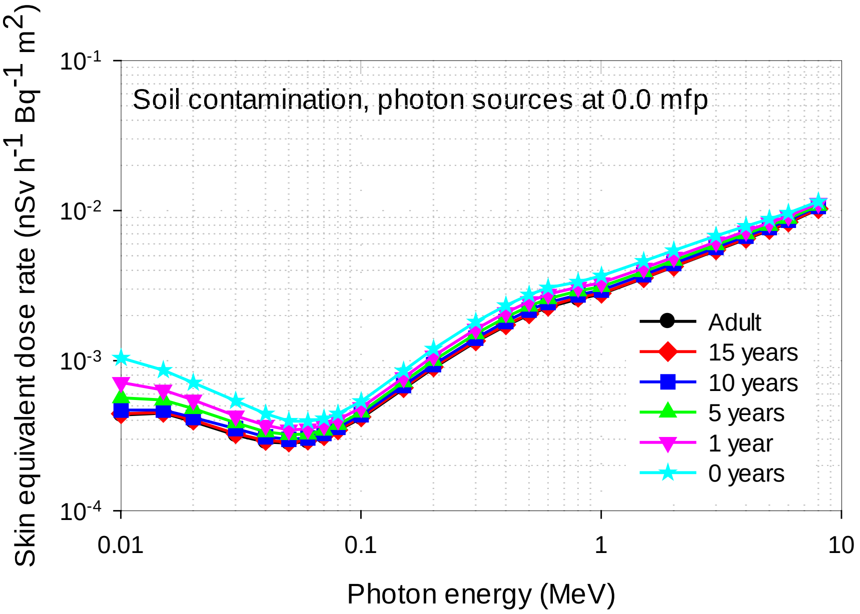

Fig. B.10. Skin dose rate coefficients for monoenergetic photon sources distributed at the surface as a ground plane source.

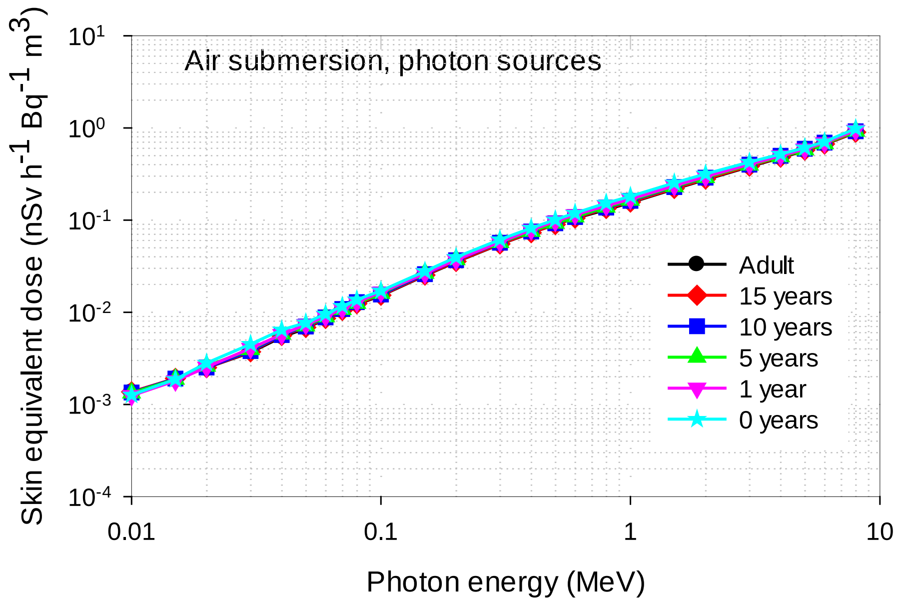

Fig. B.11. Skin dose rate coefficients for monoenergetic photon sources distributed uniformly in the atmosphere.

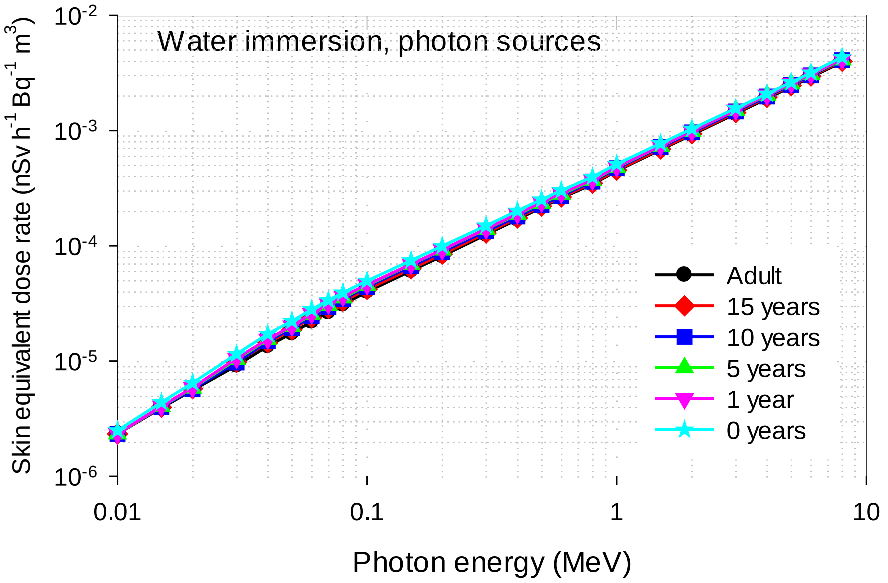

Fig. B.12. Skin dose rate coefficients for monoenergetic photon sources distributed uniformly in the water (i.e. water immersion).

B.3. References

Agostinelli, S., Allison, J., Amako, K., et al., 2003. Geant4—a simulation toolkit. Nuclear Instruments and Methods in Physics Research Section A: Accelerators, Spectrometers, Detectors and Associated Equipment 506(3), 250-303.

ICRP, 2002. Basic Anatomical and Physiological Data for Use in Radiological Protection: Reference Values. ICRP Publication 89, Pergamon Press, Oxford, UK. Ann. ICRP 32 (3-4).

ICRP, 2007. The 2007 Recommendations of the International Commission on Radiological Protection. ICRP Publication 103, Elsevier, Oxford, UK. Ann. ICRP 37 (2-4).

ICRP, 2009. Adult Reference Computational Phantoms. ICRP Publication 110, International Commission on Radiological Protection, Oxford, UK. Ann. ICRP 39 (2).

ICRP, 2010. Conversion Coefficients for Radiological Protection Quantities for External Radiation Exposures. ICRP Publication 116, International Commission of Radiological Protection, Oxford, UK. Ann. ICRP 40 (2-5).

ICRU, 1989. Tissue substitutes in radiation dosimetry and measurement. ICRU Report 44, International Commission on Radiation Units and Measurements, Bethesda, MD.

ICRU, 1992. Photon, electron, proton and neutron interaction data for body tissues. ICRU Report 46, International Commission on Radiation Units and Measurements, Bethesda, MD.

ICRU, 1997. Dosimetry of external beta-rays for radiation protection. ICRU Report 56, International Commission on Radiation Units and Measurements, Bethesda, MD.

Kim, C.H., Jeong, J.H., Bolch, W.E., et al., 2011. A polygon-surface reference Korean male phantom (PSRK-Man) and its direct implementation in Geant4 Monte Carlo simulation. Phys. Med. Biol. 56(10), 3137.

Kim, C.H., Yeom, Y.S., Nguyen, T.T., et al., 2016. The reference phantoms: Voxel vs polygon. Ann. ICRP 45, 188-201.

Lee, C., Lodwick, D., Hurtado, J., et al., 2010. The UF family of reference hybrid phantoms for computational radiation dosimetry. Phys. Med. Biol. 55(2), 339-363.

Nguyen, T.T., Yeom, Y.S., Kim, H.S., et al., 2015. Incorporation of detailed eye model into polygon-mesh versions of ICRP-110 reference phantoms. Phys. Med. Biol. 60(22), 8695-707.

Piegl, L.A., Richard, A.M., 1995. Tessellating trimmed NURBS surfaces. Computer-Aided Design 27(1), 16-26.

Sato, T., Niita, K., Matsuda, N., et al., 2013. Particle and Heavy Ion Transport code System, PHITS, version 2.52. Journal of Nuclear Science and Technology 50, 913-923.

Si, H., 2006. A Quality Tetrahedral Mesh Generator and Three-Dimensional Delaunay Triangulator.

Yeom, Y.S., Han, M.C., Kim, C.H., et al., 2013. Conversion of ICRP male reference phantom to polygon-surface phantom. Phys. Med. Biol. 58(19), 6985-7007.

Yeom, Y.S., Jeong, J.H., Han, M.C., et al., 2014. Tetrahedral-mesh-based computational human phantom for fast Monte Carlo dose calculations. Phys. Med. Biol. 59(12), 3173–3185.

Yeom, Y.S., Kim, H.S., Nguyen, T.T., et al., 2016a. New small-intestine modeling method for surface-based computational human phantoms. J. Radiol. Prot. 36(2), 230-45.

Yeom, Y.S., Wang, Z.J., Thang Tat, N., et al., 2016b. Development of skeletal system for mesh-type ICRP reference adult phantoms. Phys. Med. Biol. 61(19), 7054.

Wright, …, 2014. …

ANNEX C. CONTENT OF THE ELECTRONIC SUPPLEMENT

(C 1) The electronic supplement of this report presents age-dependent reference dose rate coefficients of effective dose and organ equivalent doses for the three environmental exposures simulated (1) soil contamination on the soil (0.0 mfp) and in the soil (planar sources at depths of 0.2, 1, 2.5 and 4 mean free paths of photon energy), (2) submersion to contaminated air and (3) immersion to contaminated water. The coefficients have been evaluated for the ICRP reference adult and paediatric phantoms using the methods described in sections 4-7.

(C 2) For soil contamination, additional data are given for the effective and organ equivalent dose rate coefficients for planar sources at specific depths of 0.5, 3.0, and 10.0 g cm^{-2} computed as described in section 8.1.

(C 3) Also given are the effective and organ equivalent dose rate coefficients for photon sources exponentially distributed with $\beta = 0.5$, 1.0, 2.5, and 5.0 g cm^{-2} as discussed in 8.1.

(C 4) Data are given for every age group and for the male and female phantoms separately. The effective and organ equivalent dose rate coefficients are normalized to environmental radioactivity concentration and are given in units of nSv h^{-1} Bq^{-1} m^{-2} (for soil contamination) or nSv h^{-1} Bq^{-1} m^{-3} (for submersion to contaminated air and water immersion).

(C 5) The supplement is organised in three main folders (one for each exposure geometry): 'Soil contamination', 'Air submersion' and 'Water immersion'. The folder 'Soil contamination' contains 7 subfolder: 5 for each mean free paths considered, and 2 for planar and exponential sources. The folders of the planar and exponential sources contain 3 subfolders for each specific depths at 0.5, 3.0, and 10.0 g cm^{-2}, and 4 subfolder for photon sources exponentially distributed with 4 different relaxation masses per unit area, $\beta = 0.5$, 1.0, 2.5, and 5.0 g cm^{-2}, respectively.

(C 6) All data are given in two different formats: ASCII format and Microsoft Excel Format.

(C 7) Reference values of the organ equivalent dose rate coefficients are given for the following organs: bone-marrow (red), colon, lung, stomach, breast, ovaries, testes, bladder, oesophagus, liver, thyroid, skeletal endosteum, brain, salivary glands, skin, remainder tissues, adrenals, extrathoracic (ET) region, gall bladder, heart, kidneys, lymphatic nodes, muscle, oral mucosa, pancreas, prostate, small intestine, spleen, thymus, and uterus/cervix.

(C 8) Moreover, a data viewer code is provided which allows comfortable viewing and downloading of the organ and effective dose rate coefficients.